UNIVERSITÀ
DI PARMA

DEPARTMENT OF CHEMISTRY, LIFE SCIENCES AND ENVIRONMENTAL SUSTAINABILITY

Doctoral Programme in Material Science and Technology
XXXIV Cycle

Thermally Activated Delayed Fluorescence: Excited State Engineering Towards Efficient Organic Light Emitting Diodes

Coordinator:
Prof. Enrico Dalcanale

Supervisor:
Prof. Anna Painelli
Prof. Francesca Terenziani

PhD student:
Rama Dhali

2019-2022

Contents

Introduction **5**

1 Environmental Effects on Excited States **13**
1.1 Introduction . . . 13
1.2 The Model and the Antiadiabatic Approximation . . . 16
1.3 Environmental Effects on Excitation Energy . . . 21
1.3.1 Computational Details . . . 21
1.3.1.1 Antiadiabatic and Exact Diagonalization . . . 24
1.3.1.2 Antiadiabatic vs Adiabatic methods . . . 26
1.3.1.3 Solvated Dyes: Comparison between Adiabatic FSM and TD-DFT Results . . . 29
1.3.2 Discussion . . . 32
1.4 Environmental Effects on Singlet-Triplet Energy Gaps . . . 34
1.4.1 Computational Details . . . 35
1.4.1.1 Choice of the Functional . . . 35
1.4.1.2 Excitation Energies in Natural solvent under PCM . . . 36
1.4.2 Computational Results . . . 38
1.4.3 Antiadiabatic Approach to Singlet-Triplet Energy Gap . . . 42
1.4.3.1 Few-State Model: LR, CLR and EI Approaches . . . 42
1.4.4 Discussion . . . 45
1.5 Conclusions . . . 46

Appendix A Long-Range ω-tuned Functional **50**

Appendix B Additional TD-DFT Results on TADF Dyes **54**

2 Understanding TADF of DMAC-TRZ **65**
2.1 Introduction . . . 65
2.2 Optical Spectroscopy . . . 66
2.3 Computational Analysis . . . 73

2.4 Understanding TADF: Conformational Disorder and Matrix Effects 76
2.4.1 Setting up the Model 76
2.4.1.1 θ Dependence of τ 77
2.4.1.2 Three-State vs Four-State Model for DMAC-TRZ 78
2.4.1.3 The Role of the Effective Local Triplet State 80
2.4.2 Validating the Model against Steady-State Spectra 81
2.4.2.1 Modelling the Solvent Response 82
2.4.3 Matrix Effect 86
2.5 Conclusions 91

3 Large Dihedral Angle Relaxation of DMAC-py-TRZ 94
3.1 Introduction 94
3.2 Computational Analysis 96
3.3 Experimental Details 102
3.3.1 Cyclic Voltammetry 102
3.3.2 Optical Spectra 103
3.3.2.1 Absorption Oscillator Strength 103
3.3.2.2 Effect of Solvent Polarity 104
3.3.3 DMAC-py-TRZ in Solid Matrixes 109
3.4 Conclusions 113

Conclusions and Perspectives 114

Bibliography 117

List of Publications 135

Acknowledgements 137

Introduction

Organic light emitting diodes (OLEDs) are now must-have displays due to several design advantages and they have better efficiency than usual liquid-crystal displays (LCDs).[1] OLEDs have the most successful application in the field of plastic optoelectronics due to their high brightness, higher contrast, lower power consumption and lightweight compared to traditional LCD displays.[1] OLED devices are composed of a thin layer of fluorescent organic material sandwiched between an anode and a cathode (see Figure 1, image courtesy: cynora).[2,3] When a sufficient voltage is applied across an organic semiconductor layer, electrons and holes are injected and they travel through the organic semiconductor. These electrons and holes then recombine in organic layers into electron-holes pair, also known as excitons.[4–6] The excitons may decay back to the ground state emitting a photon.

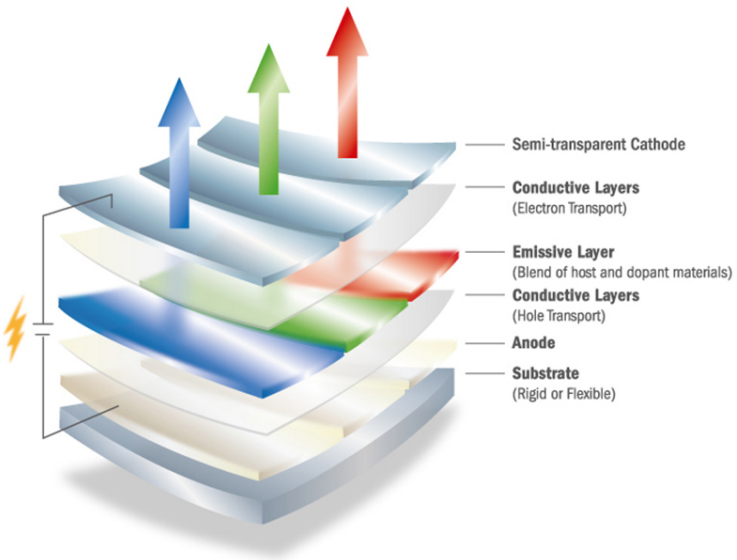

Figure 1: Design of a generic OLED device.

Since electrons and holes are fermions with half integer spin ($S = 1/2$), and depending on the relative orientations of the two spins, different spin states may be obtained for the excitons. If the exciton has a total spin of zero ($S = 0$), it is called a singlet exciton; if it

has a total spin of one ($S = 1$) it is a triplet exciton. As shown in Figure 2 (image courtesy: Edinburgh Instruments), three possible recombination of half integer spins can form $S = 1$ exciton (hence the name triplet) and but only one recombination can form an $S = 0$ spin (hence the name singlet). This means upon electron-hole recombination, 25% singlet excitons and 75% triplet will be formed.

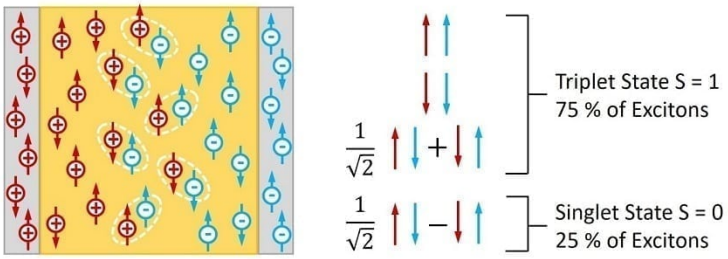

Figure 2: Formation of 25% of singlet and 75% of triplet excitons in OLEDs device.

The emission (radiative decay) from triplet state (T_1) to to ground state singlet (S_0) is a spin-forbidden process and and this creates a major issue in creation of an efficient OLED. 75% of total electrons and holes injected into device are therefore wasted and sets an maximum Internal Quantum Efficiency (IQE) of 25% because of the limit of the harvestiing fluorescent excitons only.[5,7,8] 1^{st} generation of OLED devices are based on this principle (Figure 3, 1^{st} Generation). The External Quantum Efficiency (EQE), namely the ratio of excitons to the incident photons, is determined by the IQE as well as an out-coupling term, typically capped at 20%, for a maximum EQE of 5% in fluorescent OLEDs. Improving IQE of OLED devices is the most pressing issue, involving a multidisciplinary effort of chemists, physicists and engineers. Harvesting triplet states into emissive species is the most attractive way to do so. Moving away from the pure organic materials to the use of heavy metals (Ir, Pt *etc.*) materials was the first solution to this problem. The use of heavy metals helps to increase spin-orbit coupling (SOC) between T_1 and S_0 states allowing emission from the triplet states. Use of heavy metals also increase SOC between S_1 and T_1 states and the population of S_1 state can trasferred to T_1 state via intersystem crossing (ISC). This leads to a maximum theoretical IQE of 100% for this phosphorecence based OLED device.[9,10] OLEDs based on this mechanism are there known as Phosphorescent Organic Light-Emitting Diodes (PHOLED) or 2^{nd} Generation of OLED (Figure 3, 2^{nd} Generation). However, this approach has several limits: first of all, heavy metals such as Ir and Pt are expensive. Since fluorescence and phosphorescence may coexist, color purity is degraded. Moreover, blue emission represents a problem since phophorecence is typically red-shifted with respect to fluorescence. Finally, long-lived triplet states in the device increase the risk of chemical degradation and free radical formation, while, at the same time, hinder the

applicability of PHOLEDs in systems where high frequency modulation of the emission is needed.[9,11–13]

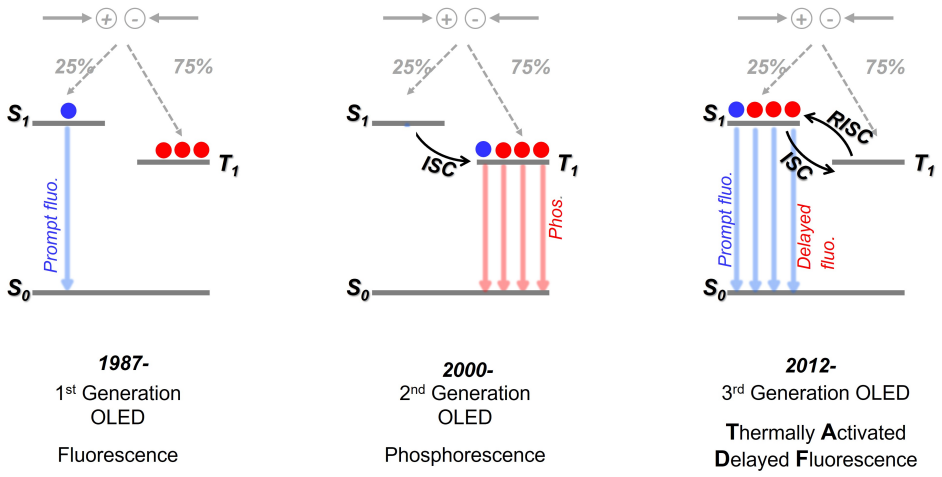

Figure 3: The principles of 1^{st}, 2^{nd} and 3^{rd} generations of OLEDs.

A promising way to move away from phosphorescent emitters towards fluorescent emitters is a phenomenon known as Thermally Activated Delayed Fluorescence (TADF). TADF is a rare phenomenon occurring in systems where a triplet state sits very close in energy to the lowest excited singlet. Once the triplet state is populated, either upon intersystem crossing (ISC) following photoexcitation or upon injection of charges in a device, it may transfer its population to the nearby singlet state via a reverse ISC (RISC). The process, made possible by the exchange of thermal energy, leads to the observation of a very long-lived (delayed) fluorescence with typical lifetimes in the microsecond regime (Figure 3, 3^{rd} Generation). TADF was discovered in 1961,[14] but remained a scientific curiosity up to 2011, when Adachi first suggested its exploitation to harvest triplets in OLEDs, rising their theoretical efficiency from 25 to 100%.[15,16] The TADF requirement of singlet and triplet states lying close in energy is easily met in dyes with low-energy charge transfer (CT) states, provided the conjugation between the electron-donor (D) and electron acceptor (A) is weak. Dyes with the D and A units arranged almost orthogonally were immediately recognized as target systems.[16–19]. However, strictly orthogonal (non-conjugated) systems also have vanishingly small spin-orbit coupling between relevant states,[20] hindering RISC. Moreover, they have a negligible transition dipole moments from the excited singlet to the ground state,[21] strongly suppressing emission intensity. An enormous effort towards the design of novel and more efficient TADF dyes includes multipolar dyes, where several D and or A groups are linked together in different geometries,[12] macromolecular and dendritic systems[22] also exploring the possibility of combining together different functionalities in the

same molecular system towards TADF-dyes that may actively respond to different stimuli, including mechanical stress and pressure.[13]. Mastering TADF then requires reliable models able to accurately account for the different interactions while maintaining the global picture in control.

Quantum chemical calculations can help the work of synthetic chemists and material scientists: the systematic in-silico study of a large amount of novel chemical structures can indeed reduce the expensive and time-consuming work in the experimental laboratory, allowing the experimentalists to focus on just the most promising structures. To this effect, cheap, fast and reliable computational approaches are needed. Time-dependent density functional theory (TD-DFT) arguably represents one of the most effective computational tools in this respect, thanks to the favorable trade-off between accuracy and computational cost. However, modeling CT transitions is non-trivial in TD-DFT, relevant results being strongly dependent on the adopted functional. Progress in this direction is offered by the development of tuned range-separated hybrid functionals, where the proper amount of exact exchange for each system is selected, without the need for a comparison with experimental data.[23–25]. Once the proper functional is selected, reliable TD-DFT results can be obtained for isolated (*gas phase*) dyes, but material scientists need to address the properties of the dyes in condensed phases (either in solution or in a matrix). The dielectric properties of local environment also largely affect the behaviour of TADF dyes. Typically used continuum models leads to wildly different results because of the adiabatic approximation used for solvent electronic degrees of freedom. This Chapter discusses the basic understanding of TADF process.

The dielectric properties of local environment largely affect the relative energies of CT and LE states and therefore alter the properties and behaviour of TADF dyes. Continuum solvation models are largely exploited to address the issue. However there are different implementations of continuum models leading to wildly different results. We traced the origin of this behavior to a fundamental problem of continuum model implementations in dealing with fast solvation, i.e. the solvation component associated with the electronic degrees of freedom of the solvent and usually described in continuum models in terms of the solvent refractive index. In **Chapter 1**, an antiadiabatic approach is proposed to model how the refractive index of the surrounding medium affects optical spectra of molecular systems in condensed phases. The approach solves some of the issues affecting current implementations of continuum solvation models and more generally of effective models where a classical description is adopted for the molecular environment. This chapter is divided in three sections. In Section 1.2, we discuss our antiadiabatic model, in Section 1.3 we discuss how refractive index of surrounding medium affects excitation energy of a few selected sye. We propose how antiadiabatic approach solves some of the issues affecting

current implementations of continuum solvation models and more generally of effective models where a classical description is adopted for the molecular environment. In Section 1.4, we mostly focus a few selected TADF dyes, we show how current implementations of continuum solvation models do not properly address environmental effects on the singlet-triplet gap, with results that wildly depend on the adopted approximation scheme and lead, in some cases, to an inversion of the order of the lowest singlet and triplet states.

In **Chapter 2**, **DMAC-TRZ** is presented as a representative dye with an extensive computational analysis along necessary experimental data from the host lab. The information obtained along the two paths were finally combined in a reliable complete model for the system. We build, parametrize against TD-DFT and validate against experiment a first complete model for a TADF dye, accounting for all relevant interactions.The model, accounting for charge transfer and local singlet and triplet states, spin-orbit coupling, conformational and vibrational degrees of freedom, sets the basis for a sound understanding of the photophysics of TADF dyes in different environments. The charge-transfer nature of the fluorescent state and of the almost degenerate phosphorescent state is unambigously demonstrated. The concurrent role played by conformational degrees of freedom and the matrix polarizability in governing TADF is addressed. The model, without adjustable parameters, satisfactorily reproduces the absorption and fluorescence spectra (in terms of band positions and bandshapes) and their evolution with the solvent polarity, as well as absorption, fluorescence and phosphorescence spectra in a solid matrix. To the best of our knowledge this is a brand new result: reproducing observed spectra is not possible for any model published so far for TADF dyes.

In **Chapter 3**, **DMAC-py-TRZ**, a new TADF dye is presented. The dye is obtained via a modest chemical modification of the parent **DMAC-TRZ** dye, substituting a CH unit in the triazine unit with an N atom. This marginal change has an enormous impact on the structure and hence on the photophysics of the dye as the release of the steric hindrance, that forces **DMAC-TRZ** in an orthogonal structure, allows in **DMAC-py-TRZ** for a planar and slightly bent structure in the ground state. The large conjugation in the bent **DMAC-py-TRZ** structure, demonstrated by the strong intensity of the lowest (CT) excitation, hinders TADF, due to the very large singlet-triplet gap. Quite interestingly, the computational analysis predicts that emission occurs from a relaxed orthogonal excited state geometry, as confirmed by the huge Stokes shift observed in non-polar solvents. In this relaxed geometry TADF is indeed observed. Emission from the unrelaxed state is recovered in glassy frozen solvents, as demonstrated by the large blue shift of the emission band if compared with liquid solvent and by the disappearance of the TADF response. In amorphous matrices, structural disorder leads to the coexistence of both structures, even if, depending on the dye concentration dual fluorescence may disappear as a result of a fast energy transfer from

the bent to the orthogonal structures. We maintain that this efficient energy transfer is responsible for the good efficiency of **DMAC-py-TRZ** devices, in spite of the presence in the matrix of a sizable portion of dyes in the bent structure, unfavorable to TADF. Part of this work is carried out with a close collaboration with Prof. Eli Zysman-Colman, University of St Andrews, Scotland.

Chapter 1

Environmental Effects on Excited States

1.1 Introduction

The definition of reliable and practical models to simulate how the local environment affects the spectra of molecular materials represents a theoretical and computational challenge with enormous practical implications: environmental effects can be detrimental to the performance of molecular materials for advanced applications, including OLED and solar cells, but, when properly understood, they can be exploited towards optimized materials in a smart-matrix approach.

If specific interactions can be neglected, electrostatic forces dominate the interplay between the solute (the molecule of interest) and the solvent (the local molecular environment, either a solvent, a solid matrix, a biological environment, etc), so that the solvent is described in terms of its dielectric properties.[26] A good solvent is transparent in the spectral window of interest (typically the visible and near-UV, $\sim$ 1-4 eV) and its electronic absorption bands are found deep in the UV region (>6 eV). Kramers-Krönig equations relate the real and imaginary parts of the dielectric response: since in the region of interest the solvent is transparent, in the same region the dielectric costant is real and almost frequency independent, its square root being usually referred to as the refractive index, $\varepsilon_{opt} = \eta^2$.[27] Vibrational transitions are weak and marginally contribute to the dielectric constant. Orientational motions are optically silent in non-polar solvents, whose dielectric constant therefore stays almost invariant down to its static value: $\varepsilon_{st} \sim \varepsilon_{opt}$. In polar solvents instead the orientational motion of solvent molecules gives a large contribution to the static dielectric constant and $\varepsilon_{st} > \varepsilon_{opt}$.

With respect to relevant solute degrees of freedom (visible and near UV), the electronic degrees of freedom of the solvent (with resonances deep in the UV) are much faster, while the orientational motion of polar solvent molecules (picosecond timescale in liquid solvents, longer in solid matrices) is much slower. In either case, the distinctly different timescales

for the solute and solvent dynamics allow for the separation of the two systems in effective solvation models. Two families of models have been developed in this context: in the QM-MM approch the solute is modeled by a quantum-mechanical (QM) Hamiltonian accounting for the electrostatic potential generated by the surrounding medium that is described in a classical Molecular Mechanics (MM) approach. In a simpler but powerful approach, the solvent is described as a continuum dielectric medium, as in the polarizable continumm model (PCM) or in the conductor-like screening model (COSMO).[28–34]

In the following, we adopt the generic term *solvent* to address either the liquid solvent surrounding the dye in solution, or the solid matrix surrounding the dye, as e.g. in a device. Models where both the dye and the surrounding solvent are treated quantum-mechanically are clearly impractical and approximation strategies must be devised to separate the solute and solvent problem. In this perspective, effective solvation models are introduced where a quantum mechanical Hamiltonian is defined for the solute, implicitly accounting for the effects of the surrounding medium. When constructing an effective solvation model, a hierarchy of approximations must be considered. The first step is the separation of the solute and solvent problems, relying on the different timescales of relevant degrees of freedom (DoF). Specifically, being interested to model the solute optical spectrum in the visible-near UV regions, we can safely assume that polar solvation, related to the orientational motions of polar solvent molecules around the solute, represents a slow motion and can be treated adiabatically. On the opposite, electronic solvation accounts for the rearrangement of the electronic clouds of solvent molecules in response to the charge distribution in the solute: the corresponding DoF have typical frequencies far in the ultraviolet, and are therefore much faster than the solute DoF. The adiabatic approximation must then be abandoned in favor of the antiadiabatic (AA) approximation.[35] Of course, cases may occur where the timescales of solute and solvent motions are comparable. In these special cases effective solvation models cannot be reliably defined.

Once the framework for the solute-solvent separation is set, models for the solute and solvent and for their interaction must be defined. As for the solute, a vast variety of quantum-mechanical models is possible, ranging from parametric models accounting for just few electronic degrees of freedom, semiempirical models, first-principle DFT and TD-DFT models, high-quality ab-initio etc. The choice of the model Hamiltonian and of the relevant basis of course heavily affects the quality of the results and their reliability. The solvent in turn can be described as a continuum dielectric medium, linearly responding to electrostatic perturbations (elastic medium).[26,36] Alternatively, one can rely on atomistic pictures for the solvent, in MM or MD approaches.[37–39] Quite interestingly, in these mixed approaches a number of solvent molecules can be included into the portion of system treated quantum-mechanically, and, when this number is large enough, the limit of a full quantum

mechanical treatment of the solute and solvent is reached.[40]

The solute-solvent interaction can be simplified to a dipolar interaction in an approach that can be extended to multipolar terms. In more refined approaches, the solute is contained in a cavity carved in the solvent, whose shape and dimensions are defined according to several approximation schemes with variable degrees of details. In continuum solvation models, the solute generates charges at the cavity surface, that in turn affect the potential felt by the solute. In atomistic models, the solute affects the orientation of surrounding molecules and (in polarizable models) also their charge distribution. In turn, the charges on the surrounding molecules affect the potential felt by the solute.

Fixing all the details in the approximation ladder leads to a proliferation of effective solvation models, that cannot be reviewed here. However the first approximation, related to the separation of solute and solvent degrees of freedom, leads to two qualitatively different approaches to effective solvation. In the adiabatic approximation the molecular Hamiltonian is diagonalized for a fixed value of the potential generated by the surrounding medium (that, depending on the model, means fixed charges on the surrounding molecules or on the surface cavity, or a fixed reaction field, etc). The calculation can be repeated for different values of the potential, typically fixing it at the equilibrium value relevant for each state (hence leading to state-specific approaches). In any case, in the adiabatic approximation, each Hamiltonian is defined and diagonazed for a fixed potential. The adiabatic approach to solvation closely resembles the adiabatic approach adopted to separate electronic and vibrational DoF in molecular systems (most often in the so-called Born-Oppenheimer scheme).[41] It is well known that the adiabatic approximation can be reliably applied to separate electronic and vibrational DoF when the nuclear dynamics is much slower than the electronic dynamics. Analogously, the adiabatic approximation applied to separate solvation degrees of freedom works well when solvation charges (and the resulting potential) move slowly with respect to the solute DoF of interest. However, when dealing with electronic solvation we are considering fast DoF: the adiabatic approximation must be abandoned since it relies on a molecular Hamiltonian where the charges in the surrounding solvent are considered frozen, while they actually move faster than the solute DoF. Rather an AA approximation can be invoked, assuming an instantaneous rearrangement of the solvent charges and of the resulting potentials to the charge fluctuations in the solute. A single AA Hamiltonian is thus obtained, whose diagonalization leads in a single shot to all molecular eigenstates.

This chapter is divided in three section. In Section 1.2, we discuss our antiadiabatic model, in Section 1.3 we discuss how refractive index of surrounding medium affects excitation energy of a few selected dye. We propose how antiadiabatic approach solves some of the issues affecting current implementations of continuum solvation models and more generally of effective models where a classical description is adopted for the molecular

environment. In Section 1.4, we mostly focus a few selected TADF dyes, and show how current implementations of continuum solvation models do not properly address environmental effects on the singlet-triplet gap, with results that wildly depend on the adopted approximation scheme and lead, in some cases, to an inversion of the order of the lowest singlet and triplet states.

1.2 The Model and the Antiadiabatic Approximation

In the absence of the solute the solvent is isotropic. The solute perturbs the solvent that responds generating the *reaction* fields, F_{el} and F_{or} (we only consider the main component of the fields as relevant for quasi-linear molecules, the derivation can be easily extended to the general case). At the equilibrium, both the fast and slow components of the reaction field are proportional to the expectation value of the solute dipole moment in the state of interest, $(\vec{F}_{el/or})_{eq} = r_{el/or}\langle\hat{\vec{\mu}}\rangle$, with the proportionality constant determined by the medium dielectric properties:[42,43]

$$\begin{aligned} r_{el} &= \frac{2}{4\pi\varepsilon_0 a^3} f(\varepsilon_{opt}) \\ r_{or} &= \frac{2}{4\pi\varepsilon_0 a^3} \left[f(\varepsilon_{st}) - f(\varepsilon_{opt})\right] \end{aligned} \tag{1.1}$$

where a is the radius of the (spherical) cavity occupied by the solute, ε_0 is the vacuum permittivity and $f(\varepsilon) = (\varepsilon - 1)/(2\varepsilon + 1)$. So the two terms in the parenthesis of Equation 1.1 will read as:

$$\begin{aligned} f(\varepsilon_{opt}) &= \frac{\varepsilon_{opt} - 1}{2\varepsilon_{opt} + 1} \\ f(\varepsilon_{st}) &= \frac{\varepsilon_{st} - 1}{2\varepsilon_{st} + 1} \end{aligned} \tag{1.2}$$

Since, we are interested for transparent solvent, in the same region the dielectric constant is real and almost frequency independent, its square root being usually referred to as the refractive index, $\varepsilon_{opt} = \eta^2$.[27] Orientational motions are optically silent in non-polar solvents, whose dielectric constant therefore stays almost invariant down to its static value: $\varepsilon_{st} \sim \varepsilon_{opt}$. In polar solvents instead the orientational motion of solvent molecules gives a large contribution to the static dielectric constant and $\varepsilon_{st} > \varepsilon_{opt}$.

In the hypothesis that the solvent behaves as an elastic medium, we introduce a quadratic potential term, so that the solute-solvent Hamiltonian reads:

$$H = H_{gas} + \left[\frac{1}{2}K_{el}F_{el}^2 + T_{el} - \hat{\vec{\mu}} \cdot \vec{F}_{el}\right] + \left[\frac{1}{2}K_{or}F_{or}^2 - \hat{\vec{\mu}} \cdot \vec{F}_{or}\right] \tag{1.3}$$

where $K_{el/or}$ are the force constants associated with the electronic and orientational solvent degrees of freedom and all other terms are defined in the before. H_{gas} is the gas phase molecular Hamiltonian and the two parentheses group terms relevant to the electronic and orientational solvation. T_{el} is the kinetic energy associated with the electronic reaction field. The corresponding term in the second parenthesis is missing since the adiabatic approximation works well for the orientational field.

At the equilibrium the energy is at a minimum for both F_{el} and F_{or}, and, exploiting the Hellman-Feynman theorem, we get:

$$\begin{aligned} 0 &= \frac{\partial \langle H \rangle}{\partial F_{or}} = K_{or} F_{or} - \langle \hat{\mu} \rangle \\ 0 &= \frac{\partial \langle H \rangle}{\partial F_{el}} = K_{el} F_{el} - \langle \hat{\mu} \rangle \end{aligned} \tag{1.4}$$

Comparing these equations with the equations that impose the proportionality between the fields and the dipole moments $(F_{el/or})_{eq} = r_{el/or} \langle \hat{\mu} \rangle$ and we obtain:

$$\begin{aligned} K_{or} &= \frac{1}{r_{or}} \\ K_{el} &= \frac{1}{r_{el}} \end{aligned} \tag{1.5}$$

We finally obtain the Hamiltonian of the solvated molecule which reads:[44,45]

$$H = H_{gas} + \left[\frac{\vec{F}_{el}^2}{2 r_{el}} + T_{el} - \hat{\vec{\mu}} \cdot \vec{F}_{el} \right] + \left[\frac{\vec{F}_{or}^2}{2 r_{or}} - \hat{\vec{\mu}} \cdot \vec{F}_{or} \right] \tag{1.6}$$

In the following we only address electronic solvation, shortly discussing polar solvation in the discussion section. Moreover, we consider quasi-linear molecules, whose dipole moment has sizable matrix elements only along a special molecular axis (Figure 1.2), at least for the states of interest. F_{el} and $\hat{\mu}$ denote the main components of the reaction field and of the dipole moment operator, respectively.

In second-quantization, we set $F_{el} = g(\hat{b}^\dagger + \hat{b})$, where $\hat{b}$ ($\hat{b}^\dagger$) is the boson annihilation (creation) operator, $g = \sqrt{\hbar \omega_{el} r_{el}/2}$ and ω_{el} is the frequency associated with the solvent electronic polarization (typically in the ultraviolet). With these definitions, the Hamiltonian of a molecule only coupled to F_{el} (the first two terms in the Hamiltonian in Equation 1.6) reads:

$$H_0 = H_{gas} - g\hat{\mu}(\hat{b}^\dagger + \hat{b}) + \hbar \omega_{el} \left(\hat{b}^\dagger \hat{b} + \frac{1}{2} \right) \tag{1.7}$$

If H_{gas} is defined on a finite basis set $(|f_1\rangle, |f_2\rangle, ..., |f_N\rangle)$, a numerically exact non-adiabatic solution of the Hamiltonian in Equation 1.7 is obtained diagonalizing the Hamiltonian matrix written on the direct product basis: $(|f_1\rangle, |f_2\rangle, ..., |f_N\rangle) \times (|0\rangle, |1\rangle, |2\rangle, ...)$, where $|n\rangle$ are the eigenstates of the harmonic oscillator in the last term of Equation 1.7.[45] Of course,

the infinite oscillator basis is truncated to large enough n as not to affect the properties of interest.

In the proposed model, a single effective oscillator with frequency ω_{el} describes the electronic spectrum of the solvent.[45] This oversimplified view only applies if the solvent absorption bands occur at much higher energy than the solute absorption bands, so that the details of the solvent spectrum become irrelevant. This is not a specific limitation of our model, but it is an intrinsic limitation of any effective solvation model. Indeed, if the details of the electronic excitation spectrum of the solvent are important, then a complete QM description of the solute and the surrounding medium is unavoidable.

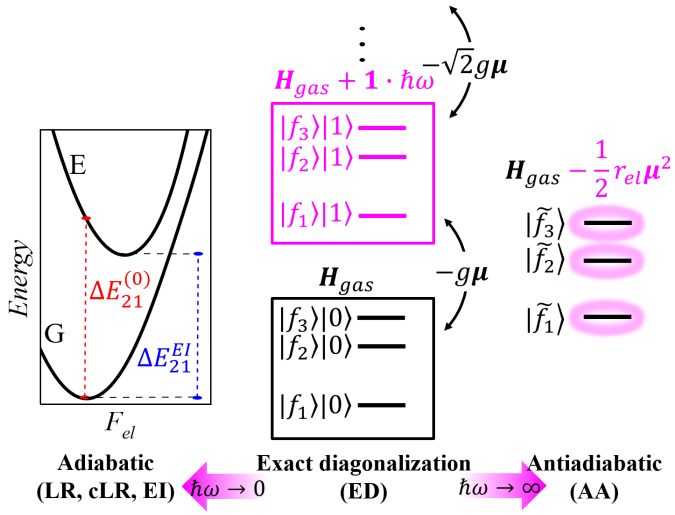

Figure 1.1: Central panel: a sketch of the non-adiabatic Hamiltonian. Left panel: in the adiabatic approximation we show the ground and excited state potential energy curves and the definition of the vertical and EI transition energies. Right panel: a sketch of the AA renormalized molecular states and Hamiltonian.

For the sake of clarity, we consider a molecular system described in terms of 3 electronic states (f_1, f_2, f_3), even if the derivation applies to any number of states. The Hamiltonian for the isolated (gas-phase) molecule reads:

$$H_{gas} = \begin{pmatrix} h_{11} & h_{12} & h_{13} \\ h_{21} & h_{22} & h_{23} \\ h_{31} & h_{32} & h_{33} \end{pmatrix} \tag{1.8}$$

On the same basis, the matrix elements of the dipole moment operator are:

$$\mu_{ij} = \langle f_i | \hat{\mu} | f_j \rangle \tag{1.9}$$

The non-adiabatic basis is the direct product of the electronic basis (f_1, f_2, f_3) times the first three eigenstates of the harmonic oscillator describing fast solvation $(|0\rangle, |1\rangle, |2\rangle,$

the calculation can be easily generalized to an arbitrary number of states). The nine basis functions are:

$$|f_1\rangle|0\rangle, |f_2\rangle|0\rangle, |f_3\rangle|0\rangle, |f_1\rangle|1\rangle, |f_2\rangle|1\rangle, |f_3\rangle|1\rangle, |f_1\rangle|2\rangle, |f_2\rangle|2\rangle, |f_3\rangle|2\rangle \tag{1.10}$$

On this basis the Hamiltonian describing the solute interacting with the fast solvation field (Equation 1.7) reads:

$$H_0 = \begin{pmatrix} h_{11} & h_{12} & h_{13} & -g\mu_{11} & -g\mu_{12} & -g\mu_{13} & 0 & 0 & 0 \\ . & h_{22} & h_{23} & -g\mu_{21} & -g\mu_{22} & -g\mu_{23} & 0 & 0 & 0 \\ . & . & h_{33} & -g\mu_{31} & -g\mu_{32} & -g\mu_{33} & 0 & 0 & 0 \\ . & . & . & h_{11}+\hbar\omega_{el} & h_{12} & h_{13} & -\sqrt{2}g\mu_{11} & -\sqrt{2}g\mu_{12} & -\sqrt{2}g\mu_{13} \\ . & . & . & . & h_{22}+\hbar\omega_{el} & h_{23} & -\sqrt{2}g\mu_{21} & -\sqrt{2}g\mu_{22} & -\sqrt{2}g\mu_{23} \\ . & . & . & . & . & h_{33}+\hbar\omega_{el} & -\sqrt{2}g\mu_{31} & -\sqrt{2}g\mu_{32} & -\sqrt{2}g\mu_{33} \\ . & . & . & . & . & . & h_{11}+2\hbar\omega_{el} & h_{12} & h_{13} \\ . & . & . & . & . & . & . & h_{22}+2\hbar\omega_{el} & h_{23} \\ . & . & . & . & . & . & . & . & h_{33}+2\hbar\omega_{el} \end{pmatrix} \tag{1.11}$$

where we took advantage of the Hermiticity of the Hamiltonian matrix to only write its upper triangle. This Hamiltonian can be diagonalized numerically to get the exact non-adiabatic eigenstates.

To proceed towards the antiadiabatic (AA) Hamiltonian we use first order perturbation theory to write the effective electronic states as:

$$|\tilde{f}_i\rangle = |f_i\rangle|0\rangle + \frac{g}{\hbar\omega_{el}} \sum_{k=1}^{3} \mu_{ik}|f_k\rangle|1\rangle \tag{1.12}$$

where, in line with the AA approximation, we neglect the coupling to states with more than a single oscillator quantum and disregard molecular energies vs $\hbar\omega_{el}$. We can now calculate the matrix elements of the AA Hamiltonian as the matrix elements of the non-adiabatic Hamiltonian on the effective AA states:

$$\langle\tilde{f}_i|H_0|\tilde{f}_j\rangle = h_{ij} - 2\frac{g^2}{\hbar\omega_{el}} \sum_k \mu_{ik}\mu_{kj} + \frac{g^2}{(\hbar\omega_{el})^2} \sum_{km} \mu_{ik}\mu_{jm}\langle 1|\langle f_m|H_0|f_k\rangle|1\rangle \tag{1.13}$$

In the $\langle 1|\langle f_m|H_0|f_k\rangle|1\rangle$ term the contribution from the interaction part in the Hamiltonian, $-g\hat{\mu}(\hat{b}^\dagger + b)$, goes high order and is neglected. The only relevant contribution is $\langle 1|\langle f_m|H_{gas}|f_k\rangle|1\rangle$. Off-diagonal elements are $\langle 1|\langle f_m|H_{gas}|f_k\rangle|1\rangle = h_{mk}$ so that resulting corrections to the renormalized Hamiltonian are proportional to $\frac{g^2}{(\hbar\omega_{el})^2}$ and are therefore negligible in the $\omega_{el} \to \infty$. Diagonal elements instead are $\langle 1|\langle f_m|H_{gas}|f_m\rangle|1\rangle = h_{mm} + \hbar\omega_{el} \sim \hbar\omega_{el}$. Corresponding terms turn out $\propto \frac{g^2}{\hbar\omega_{el}}$ and must be retained, leading to

$$\langle\tilde{f}_i|H|\tilde{f}_j\rangle = h_{ij} - \frac{g^2}{\hbar\omega_{el}} \sum_k \mu_{ik}\mu_{kj} \tag{1.14}$$

Having defined $g = \sqrt{\hbar\omega_{el} r_{el}/2}$, the above equation reduces to Equation 1.15.

$$H_{AA} = H_{gas} - \frac{r_{el}}{2}\hat{\mu}^2 \tag{1.15}$$

We underline that the AA Hamiltonian is obtained via a perturbative expansion on $1/\omega_{el}$ and therefore is the exact AA Hamiltonian relevant to the $\omega_{el} \to \infty$ limit, irrespective of the strength of the solute-solvent interaction. Consistently with the separation of the solute-solvent dynamics, we then adopt an AA approach (Figure 1.1),[44,46,47] setting $\omega_{el} \to \infty$ to obtain the above Hamiltonian in Equation 1.15.

This equation applies to quasi-linear molecules, its analogous for 3D structures has $\hat{\mu}^2$ substituted by $\hat{\vec{\mu}}^2$.

1.3 Environmental Effects on Excitation Energy

An antiadiabatic approach is proposed to model how the refractive index of the surrounding medium affects optical spectra of molecular systems in condensed phases. We describe the solute-solvent interaction in the dipolar approximation: the solvent generates at the solute location an electric field (the *reaction field*) which, in turn, is proportional to the solute dipole moment. This self-consistent model set the basis to understand solvatochromism,[43,48] was adopted in parametric models,[44,49–51] and was used to discuss PCM implementations.[28,29]. To validate our view on antiadiabatic approach, following a similar strategy as in ref. 52, a few state model (FSM) is defined for the four molecules in Figure 1.2. **DANS** and **RD** are polar (electron-donor-acceptor, DA) dyes showing positive and negative solvatochromism, respectively.[53,54] **Q1** and **Q2** are quadrupolar (DAD) dyes: both have negligible polarity but **Q1**, of interest for non-linear optics,[51] has a sizable transition dipole moment to the first excited state, while **Q2**, of interest for thermally activated delayed fluorescence,[55] has a negligible transition dipole moment.

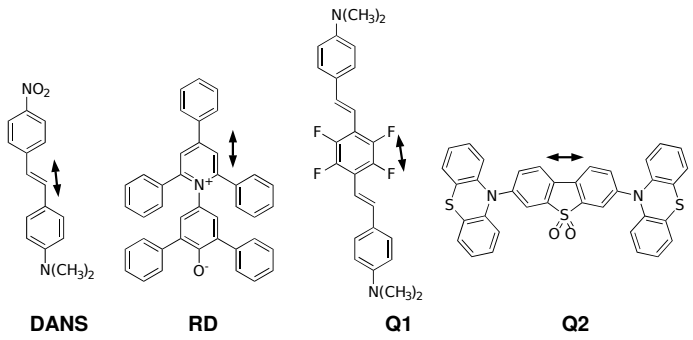

Figure 1.2: The molecules considered in this chapter. The arrows mark the direction of the main component of the dipole moment operator.[45] **DANS** (dimethylamino-nitrostylbene) and **RD** (the Reichardt dye) are polar dyes; **Q1** (a fluorinated bis-alkylaminostyryl derivative) and **Q2** (3,7-bis(10H-phenothiazin-10-yl)dibenzo[b,d]thiophene-S,S-dioxide) are representative quadrupolar dyes.

1.3.1 Computational Details

Quantum chemical calculations have been perfomed for the four molecules in Figure 1.3 (see also Figure 1.2) in gas phase using the Gaussian16 program suite.[56] Specifically we have performed TD-DFT calculation using the CAM-B3LYP functional and the 6-31G(d) basis set. Vertical energies and eigenstates are calculated at the equilibrium geometry es-

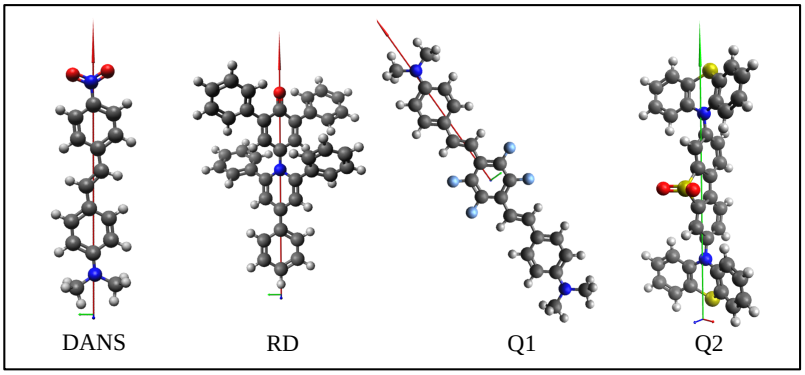

Figure 1.3: The ground state geometry (gas phase) of the four molecules considered in this work. The long arrow marks the direction of the main component of the dipole moment operator.

timated for the ground state (same functional and basis set). The first 3 eigenstates (the ground state and the lowest two singlet excited states) are typically used to construct the few-state model. On this basis the gas-phase Hamiltonian is clearly diagonal. The matrix elements of the main component of the dipole moment operator are calculated on the same basis using the program Multiwfn (http://sobereva.com/multiwfn/), feeded with the Gaussian outputs. For the non-adiabatic calculation we account for three boson states, having checked that the inclusion of additional states does not affect the results.

Table 1.1 shows all molecular parameters entering the FSM for the four considered molecules. Only the main component of the dipole moment operator is considered. The largest values of the matrix elements of $\hat{\mu}$ directed along orthogonal directions and hence neglected in the calculation are: **DANS** μ_{22}=0.57 D, **RD** μ_{23}=2.59 D; **Q1** μ_{12}=0.25 D, **Q2** μ_{22}=1.80 D. In the worst case (**RD**), the largest neglected matrix element of the dipole moment operator is less than 1/5 of the leading term.

Figure 1.4 shows the energies calculated for the four molecules either in the NA or AA approaches selecting a smaller (2) or a larger (4) basis of electronic states. Indeed for the quadrupolar dye, three states are the minimum needed to obtain sensible results and in this specific case only results obtained for 3 and 4 states are compared.

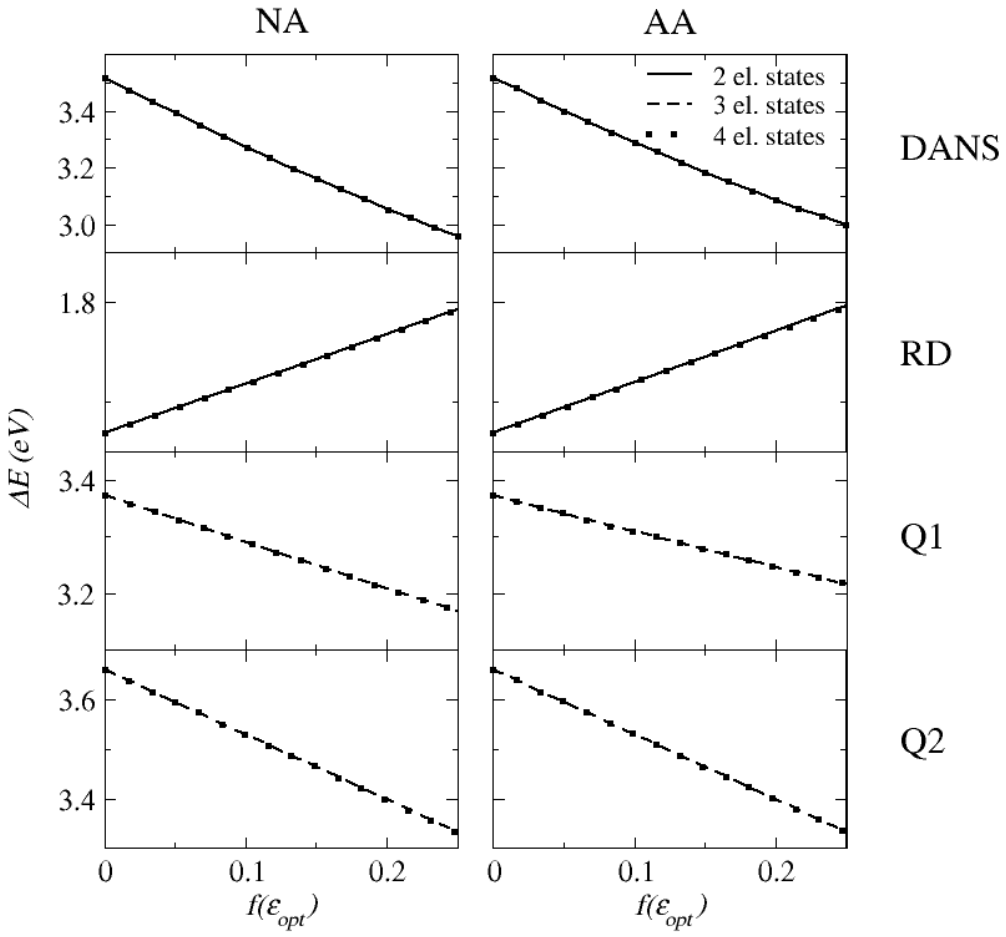

Figure 1.4: Comparing NA (left panels) and AA (right panels) transition energies calculated in the few-state model accounting for 2, 3 and 4 states. The 2-state results are not reported for **Q1** and **Q2**, since at least three states are needed to capture the physics of quadrupolar dyes.

	DANS	**RD**	**Q1**	**Q2**
E_1(eV)	0.00	0.00	0.00	0.00
E_2(eV)	3.52	1.67	3.37	3.66
E_3(eV)	4.00	2.51	4.15	3.68
μ_{11}(D)	9.38	14.82	0.00	0.00
μ_{22}(D)	25.95	−3.75	0.00	0.00
μ_{33}(D)	5.75	3.45	0.00	0.00
μ_{12}(D)	9.64	6.55	14.08	0.00
μ_{13}(D)	−0.03	0.00	0.00	0.00
μ_{23}(D)	0.04	0.38	14.44	21.97
a_0 (Å)	5.33	6.33	5.85	6.12

Table 1.1: Molecular parameters entering the FSM. Dipole moment matrix elements and transition energies are obtained from gas phase calculations

1.3.1.1 Antiadiabatic and Exact Diagonalization

The matrix elements of the dipole moment operator are calculated by Multiwfn software.[57] Figure 1.5 compares the molecular properties calculated in the AA approximation and upon exact diagonalization, ED, of H_0 (Equation 1.7) setting $\hbar\omega_{el} = 6$ or 20 eV. Results are plotted against $f(\varepsilon_{opt})$, estimated for each molcules setting a to the relevant Onsager radius.[45,56]

Results in Figure 1.5 confirm that the AA Hamiltonian in Equation 1.15 represents the $\omega_{el} \to \infty$ limit of the non-adiabatic Hamiltonian in Equation 1.7. Moreover, with the notable exception of **Q1**, results are marginally affected by the specific ω_{el} value, suggesting that effective solvation models are reliable even for solvents with comparatively low-energy excitations (for most organic media 6 eV represents the absorption cut-off, but the absorption maxima are located at much higher energies[45]). For **Q1**, a highly polarizable dye, the solute/solvent separation is more delicate and should be considered with care in largely polarizable environments.

The ground state dipole moment of the two polar dyes, **DANS** and **RD**, smoothly increases with $f(\varepsilon_{opt})$, due to the stabilization of polar states in condensed media. For **DANS**, a polar dye with a neutral ground state, this implies an increase of the transition dipole moment and a decrease of the transition frequency[49,53], while the opposite occurs for **RD**, a dye with a zwitterionic ground state.[49] Quadrupolar dyes, **Q1** and **Q2**, have vanishing permanent dipole moment, but the solvent polarizability is responsible for a sizable decrease of the transition frequency.

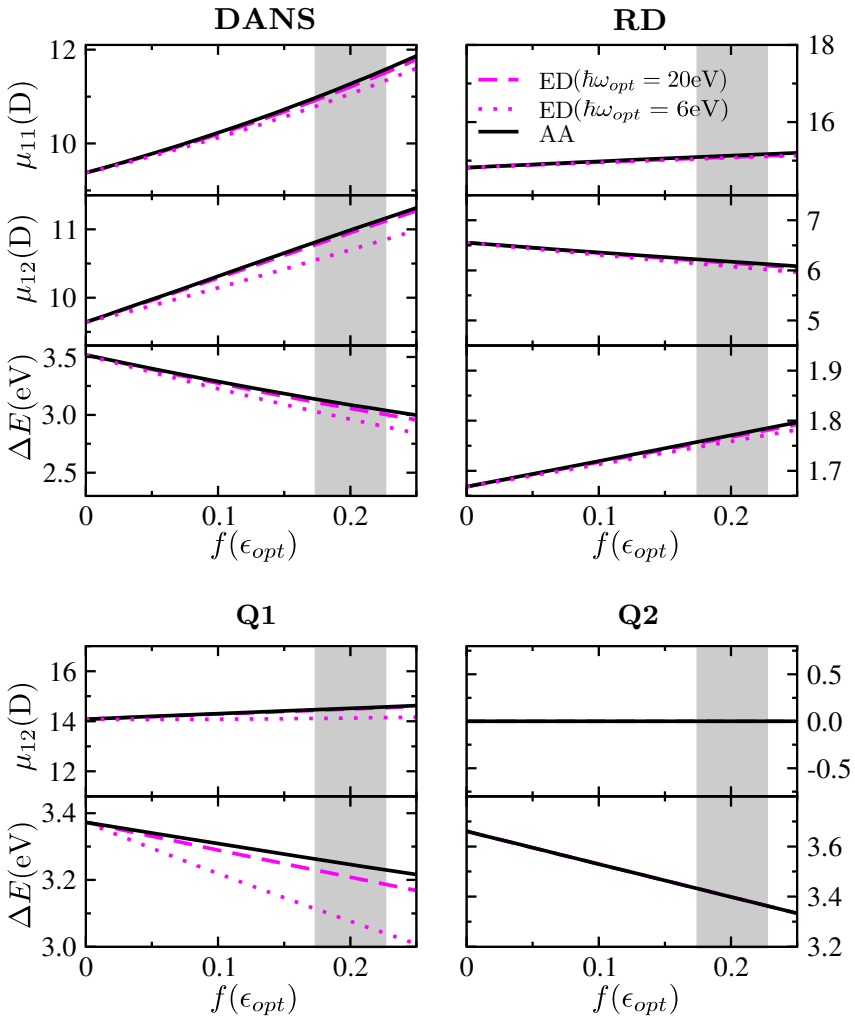

Figure 1.5: Top panels: for the two polar dyes the ground state dipole moment μ_{11}, the transition dipole moment μ_{12} and the transition energy ΔE are reported vs $f(\varepsilon_{opt})$. Bottom panels: for quadrupolar dyes the transition dipole moment μ_{12} and the transition energy ΔE are reported vs $f(\varepsilon_{opt})$. Black lines refer to AA results, magenta lines show ED results, obtained for ω_{el} =6 and 20 eV (dotted and dashed lines, respectively). For **Q2** all lines are superimposed. The shaded area marks the region where most organic solvents are located.

1.3.1.2 Antiadiabatic vs Adiabatic methods

Current implementations of effective solvation models adopt the adiabatic approximation to deal with fast solvation. Three different implementations of PCM are currently available in the Gaussian package,[56] named linear response (LR), corrected linear response (CLR) and external iteration (EI). In all cases, the calculation starts with a reference (initial) state with equilibrated fast and slow solvent DoF, and a final state, defined in different ways in the three approaches.[32,58]

LR represents the default approach in TD-HF and TD-DFT calculations. In LR,[59] excitation energies are determined directly as singularities of the frequency-dependent linear-response functions of the solvated molecule in the ground state, avoiding explicit calculations of the excited state wavefunctions, leading to a fast and computationally convenient approach. Specifically, defining the frozen-solvent transition energy as the transition energy calculated maintaining the fast and slow solvent DoF equilibrated to the reference state (the ground state for absorption, the excited state for emission), LR corrections are applied that only depend on the transition dipole moment between the reference and the final state. While computationally convenient, LR does not account for the variation of the charge distribution in the solute upon excitation, and therefore its use for CT transitions is not recommended.[59]

State-specific approaches were then proposed, accounting for the variation of the solute charge distribution upon excitation. Specifically, in EI, the fast DoF of the solvent are equilibrated to the excited state charge density, in a self-consistent procedure.[30,60] The non-equilibrium transition energy is then computed as the difference between the energy of the final state and of the initial state, both states being obtained with the fast solvent DoF equilibrated for the relevant state (for polar solvents slow solvent DoF are maintained fixed to the equilibrium value for the ground state, when referring to absorption processes, and to the excited state when referring to emission). It is important to underline that in EI two different potentials for the ground and the excited states are considered in an effort to account for the fast relaxation of the solvent DoF. However the approach is still strictly adiabatic, as each Hamiltonian is defined and diagonalized for a specific constant potential. Moreover, since transitions are computed between eigenstates obtained from the diagonalization of different Hamiltonians, the calculation of fundamental spectroscopic properties such as the transition dipole moments is precluded.[30,60]

CLR bridges the gap between LR and EI and represents a perturbative approximation to EI.[31,58] As in LR, the zero-order transition energy is calculated as the frozen-solvent transition energy. Corrections are then applied that depend on the variation of the charge distribution upon excitation. According to Ref. 61 the correction is computed by considering the orbital response to the excitation of interest, in turn obtained as the solution of the

Kohn–Sham Z-vector equations (relaxed density). CLR relies on a first order perturbative approach, so that corrections only apply to the energies, while wavefunctions are not affected. Transition dipole moments are therefore accessible and indeed coincide with those obtained in LR. However, CLR represents just a linear perturbative approximation to the complete EI calculation, and, apart from computational convenience, it is unclear why a linear perturbative treatment should be used rather than a nominally exact calculation.

For comparison purposes, we solve the Hamiltonian in Equation 1.7 in the adiabatic approximation, adopting the same strategies as implemented in Gaussian16.[56] The first step is the calculation of the ground state obtained upon diagonalization of the adiabatic Hamiltonian with F_{el} fixed at the ground state equilibrium. Top panels of Figure 1.6 compare the adiabatic and AA estimates of **DANS** and **RD** permanent dipole moments (**Q1** and **Q2** have vanishing dipole moment). The adiabatic approximation fails already in the calculation of the ground state. In particular, the adiabatic approximation underestimates the increase of the ground state dipole moment of **DANS** in condensed media. Indeed, the ground state dipole moment of **DANS** is smaller than its excited state dipole moment.[53] The reaction field equilibrated at the ground state is therefore small and more polar states than the ground state are less stabilized in the adiabatic approximation than in the AA approach where each state is stabilized by the interaction with its own reaction field. The opposite occurs for **RD**, whose dipole moment is larger in the ground than in the excited state.[54]

Turning attention to spectral properties, in the LR approach the transition energy is calculated from the vertical transition energy, $\Delta E_{21}^{(0)}$ (see Figure 1.1) as follows:[28,29]

$$\Delta E_{21}^{LR} = \Delta E_{21}^{(0)} - r_{el}|\mu_{21}|^2 \tag{1.16}$$

The LR transition energy in Figure 1.6 compares well with the AA result only for **DANS**. In general the LR energies are not accurate since they do not account for the variation of the solute polarity upon excitation.[28–30]

To improve on LR, state specific approaches were introduced.[30,31,34] Among them, the EI approach equilibrates the fast solvation field around the excited state and calculates the transition energy as the energy difference between the equilibrated excited and ground states (Figure 1.1).[30] Calculated EI energies always deviate considerably from AA results. More fundamentally, EI suffers from a basic flaw when applied to fast solvation, since the optimized ground and excited states are eigenstates of two different adiabatic Hamiltonians, thus precluding the calculation of transition dipole moments. The CLR approach circumvents this problem only accounting for perturbative corrections to transition energies, while maintaining the wavefuntions unperturbed. In CLR the correction to the transition energy is proportional to the square of the variation of the dipole moment upon excitation:[31,34,45]

$$\Delta E_{21}^{CLR} = \Delta E_{21}^{(0)} - \frac{r_{el}}{2}(\mu_{22} - \mu_{11})^2 \tag{1.17}$$

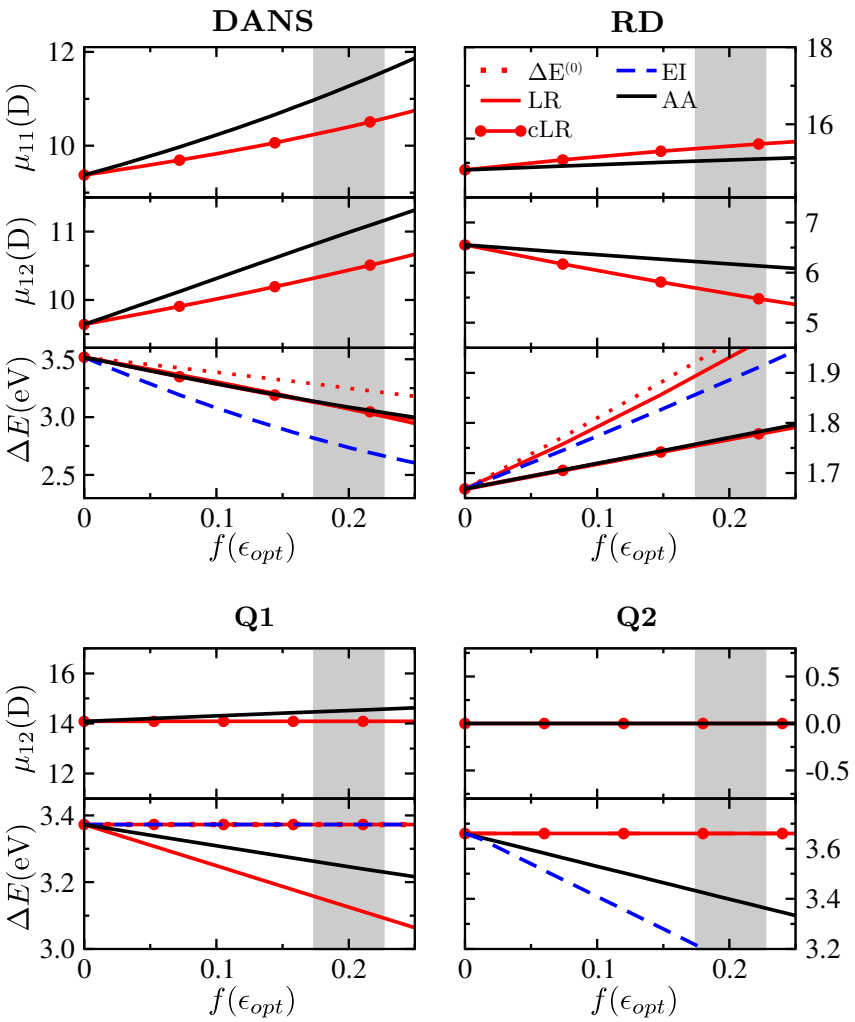

Figure 1.6: The same as in Figure 1.5 but comparing AA results (black line) with adiabatic results (colored lines). The ground state dipole moment μ_{11} (red line with dots) is the same in all adiabatic implementations. The transition dipole moment μ_{12} is undefined in EI, and is the same for LR and CLR approaches. For transition energies, the dotted red lines show the vertical excitation energy, the continuous red lines show LR results, the continuous red lines with dots show CLR results, the blue line show the EI results. For **DANS** LR and CLR energies are almost superimposed. For **Q1** the vertical excitation energy, CLR and EI energies are coincident. For **Q2** all adiabatic energies but EI are superimposed. The shaded area marks the region relevant for organic solvent and matrices.

The CLR estimate of the transition energies is good for the two polar dyes, whose solvatochromic shifts are governed by the variation of the molecular dipole moment upon excitation.[48] Some error cancellation on the two dipole moments cleary enters into play here, since, as disussed above, the adiabatic estimate of the ground state dipole moment is poor.

Adiabatic approaches fail in the most striking way for the quadrupolar dyes, **Q1** and **Q2**. These dyes have a negligible polarity and therefore have vanishing CLR corrections. The sizable transition dipole moment of **Q1** leads to a sizable LR correction, indeed largely deviating from AA results. **Q2** instead has a negligible transition dipole moment, then for this dye both LR and CLR corrections vanish. Neither LR nor CLR reproduce the excited state stabilization of **Q2** due to the medium refractive index. The solvent polarizability indeed stabilizes instantaneous charge fluctuations in the solute, an effect that cannot be appreciated in any adiabatic approach to fast solvation.

To validate the proposed FSM adiabatic results in Figure 1.6 are compared with analogous results from TD-DFT calculations for solvated dyes adopting the adiabatic implementations of PCM in Gaussian16.[56] We discuss this in next Section.

1.3.1.3 Solvated Dyes: Comparison between Adiabatic FSM and TD-DFT Results

In order to compare adiabatic results obtained adopting the FSM with TD-DFT results we have performed a series of TD-DFT (PCM model for solvation) calculations on the four solvated molecules. Calculations were run for different ε_{opt}, setting $\varepsilon_{or} = \varepsilon_{opt}$ to suppress polar solvation contributions, using the same functional and basis set as for the definition of FSM model. The LR transition energies and dipole moments are obtained as default output in TD-DFT calculation for solvated dyes (PCM). The CLR transition energies were obtained following the approach proposed by C. Guido and S. Caprasecca (details are provided in ref. 62). The vertical transition energy in the adiabatic calculation, $\Delta E_{21}^{(0)}$, is obtained by running a CLR calculation asking for extra information in the log file. The EI transition energies are obtained following the procedure suggested in J.B. Foresman and AE Frisch in ref. 63.

Figure 1.7, 1.8, 1.9 and 1.10 compare adiabatic results obtained for the four molecules in FSM and TD-DFT. A precise correspondence of FSM and TD-DFT results is not expected since FSM offers a simplified description of the electronic molecular structure and of the solute-solvent interaction. Specifically, apart from limiting attention to just few electronic states, the solute-solvent interaction is described in the dipolar approximation. In PCM instead a more detailed and realistic electrostatic potential is considered to describe the effect of the solvent on the solute. Therefore, the FSM values of $f(\varepsilon_{opt})$ do not compare directly with PCM TD-DFT values. With these caveats in mind, results shown in Figure 1.7, 1.8, 1.9 and 1.10 confirm that FSM captures the main physics of these systems. Specifically, for all dyes a reasonably good agreement is found between adiabatic FSM and TD-DFT. Some

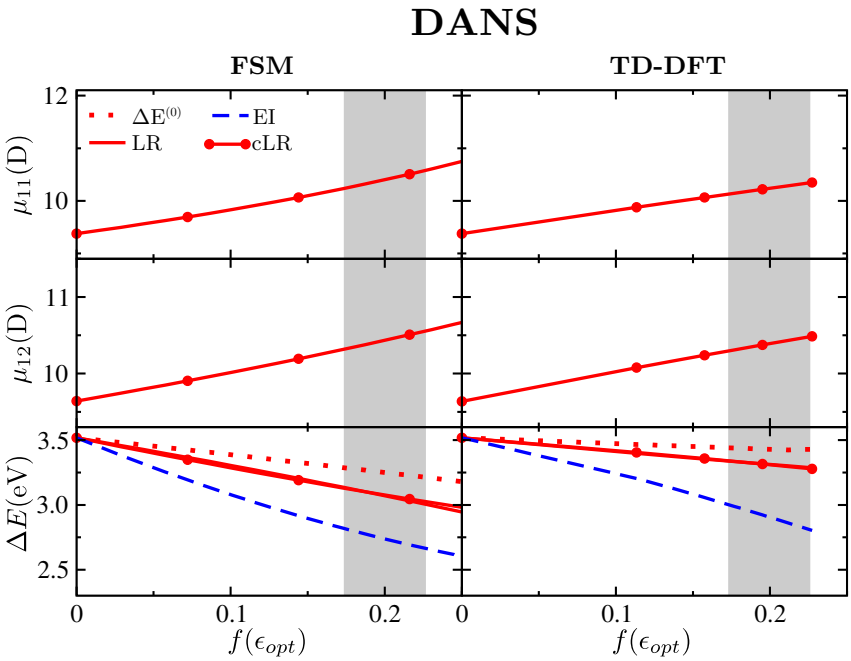

Figure 1.7: Adiabatic results for DANS. Left panels: FSM results (the same as in Figure 1.6). Right panel: TD-DFT results.

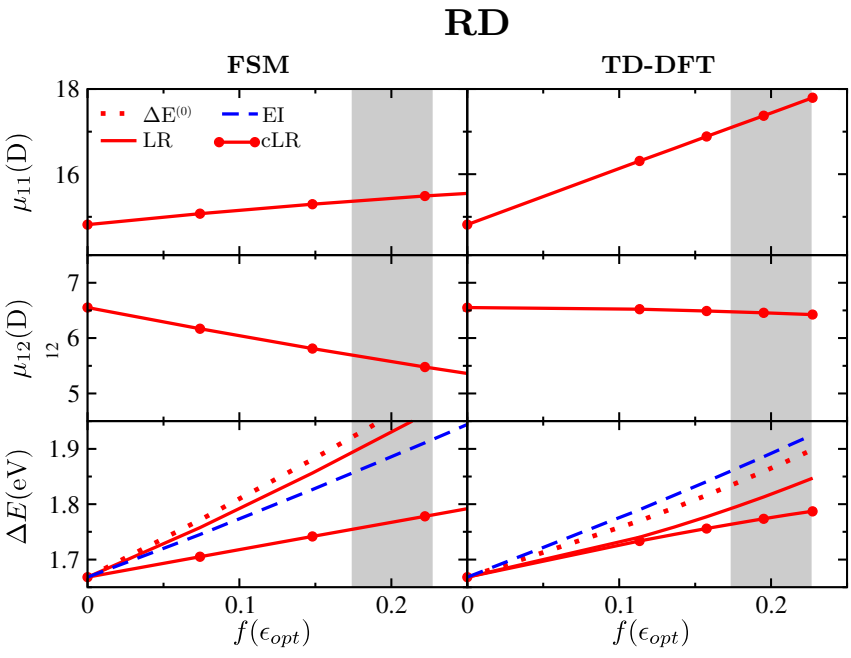

Figure 1.8: Adiabatic results for RD. Left panels: FSM results (the same as in Figure 1.6). Right panel: TD-DFT results.

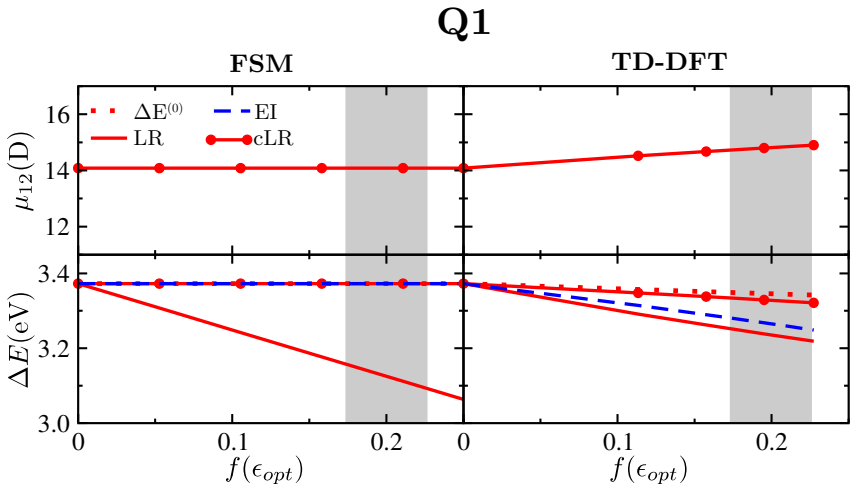

Figure 1.9: Adiabatic results for Q1. Left panels: FSM results (the same as in Figure 1.6). Right panel: TD-DFT results.

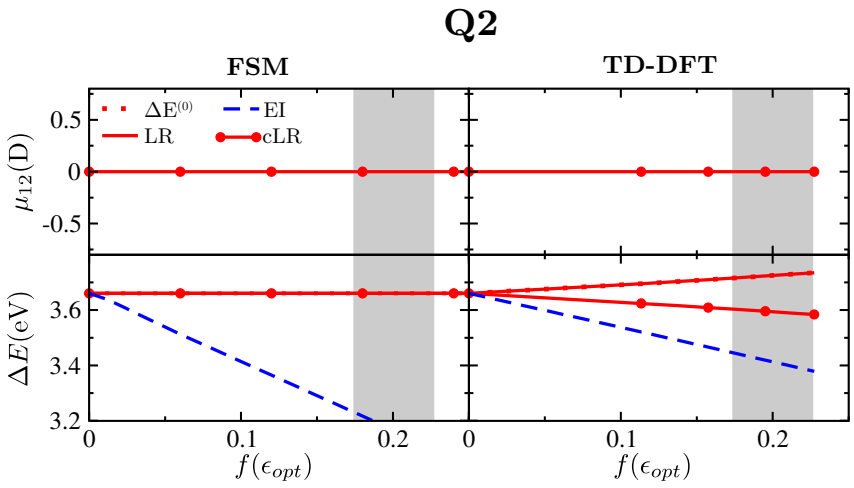

Figure 1.10: Adiabatic results for Q2. Left panels: FSM results (the same as in Figure 1.6). Right panel: TD-DFT results.

discrepancy is observed for **RD**, a zwitterionic dye with a large ground state dipole moment. This results in large solvation potentials whose FSM description in terms of a reaction field may lead to a FSM adiabatic ground state very different from the corresponding TD-DFT state, with effects that propagate in all adiabatic results.

More interestingly, TD-DFT calculates sizable small but finite CLR corrections for **Q1** and **Q2**. Since these molecules have vanishing polarity both in the ground and excited states, these corrections must be ascribed to quadrupolar and higher order terms in the solute-solvent interactions. Quadrupolar and higher-order interactions are disregarded in the proposed FSM implementation where the solute-solvent interaction is described in the dipolar approximation. While it is certainly possible extend FSM to multipolar terms, our results demonstrate that current implementations of continuum solvation models do not capture the effect of the leading (dipolar) interaction term on the transition energies of non-polar dyes.

The comparison confirms that the adopted FSM captures the basic physics of our systems. The only interesting observation is that sizable CLR corrections to the transition energies of the two quadrupolar dyes are calculated in TD-DFT. Since **Q1** and **Q2** are non-polar, these corrections are due to quadrupolar and higher order terms in the solute-solvent interactions, that are fully disregarded in our model. However, the important point here is not the quality of the dipolar approximation. Indeed our results demonstrate that the adiabatic approximation fails in the most dramatic way to describe fast solvation since it cannot account for the first order (dipolar) corrections to the transition energy of non-polar dyes.

1.3.2 Discussion

The limits of current implementations of continuum solvation models are known,[29,31,34] here we demonstrate that they are rooted in the adiabatic treatment of fast solvation. Adopting different approximation schemes (LR, CLR, EI, etc) for the calculation of transition energies cannot cure the basic problem: the adiabatic approximation does not account for the fast fluctuations of the solvent electronic clouds in response to the charge fluctuations in the solute and therefore cannot provide a reliable description of the effects of the medium refractive index on molecular properties and spectra. This problem, addressed here with specific reference to continuum solvation models, affects more generally all effective solvation models where the solvent is described classically, including the QM-MM approach. In QM-MM, even when accounting for the polarizability of the medium, a state-specific adiabatic Hamiltonian is defined for the solute and is diagonalized in the presence of a frozen potential due to the surrounding medium.

Effective solvation models must rely on an AA description of environmental electronic degrees of freedom, leading to a renormalized AA molecular Hamiltonian that accounts for

the instantaneous response of the solvent electronic clouds to charge fluctuations in the solute. The eigenstates of the AA Hamiltonian directly enter the calculation of optical spectra, without the need to invoke state-specific Hamiltonians, quite naturally solving the conundrum of calculating transitions between states obtained upon diagonalization of different Hamiltonians.

Once fast solvation is accounted for in the AA Hamiltonian, polar solvation can be dealt with in the adiabatic approximation. For this application EI,[30] leading to formally exact results, is more accurate than either LR or CLR approaches, based on perturbative expansions.[31,34] Optical transitions occur vertically with respect to slow degrees of freedom.[64] Accordingly, the eigenstates involved in the absorption process are obtained diagonalizing the adiabatic Hamiltonian with the potential due to slow solvation fixed to the ground state equilibrium value. Similarly, the states involved in fluorescence are obtained diagonalizing the adiabatic Hamiltonian with the slow-solvation potential equilibrated to the lowest excited singlet. In either case, transitions are calculated between states that are obtained from the diagonalization of the same EI Hamiltonian. The issue of incongruent eigenstates, affecting EI when applied to fast solvation, does not show up in dealing with polar solvation, for which the adiabatic approximation works well.

Extending the model to multipolar terms in the solute-solvent interaction is certainly feasible, but we believe that, having properly framed the problem of fast solvation, reliable AA effective Hamiltonians will be developed towards realistic and detailed descriptions of the molecular systems. The *GW*-Bethe-Salpeter Equation formalism coupled to continuum solvation models[39,65,66] is promising in this respect, but the development of reliable approaches to fast solvation to be implemented into popular TD-DFT computational codes is highly desirable.

In next Section 1.4 we discuss the failure of currently implemented continuum models focusing on TADF dyes. Several approximation schemes were proposed to mitigate the issue, but we underline that the adiabatic approximation to fast solvation is inadequate and cannot be improved, rather it must be abandoned in favour of an antiadiabatic approach.

1.4 Environmental Effects on Singlet-Triplet Energy Gaps

In this section we focus on effects of enviroments for TADF dyes. As discussed before, the effective design of dyes optimized for thermally activated delayed fluorescence (TADF) requires the precise control of two tiny energies: the singlet-triplet gap, that has to be maintained within thermal energy, and the strength of spin-orbit coupling. A subtle interplay among low-energy excited states having dominant charge-transfer and local character then governs TADF efficiency, making models for environmental effects both crucial and challenging.

With reference to TADF dyes, we show how current implementations of continuum solvation models do not properly address environmental effects on the singlet-triplet gap, with results that wildly depend on the adopted approximation scheme and lead, in some cases, to an inversion of the order of the lowest singlet and triplet states. In Section 1.4.2 we briefly introduce the three available implementations of continuum solvation model (PCM) in Gaussian package. In Section 1.4.2 we report results obtained with the three approaches on 6 different TADF dyes. In section 1.4.3 we demonstrate that the observed inversion of the singlet and triplet states is indeed a spurious result obtained imposing the adiabatic approximation to fast solvation. Finally, the last Section puts main results in perspective.

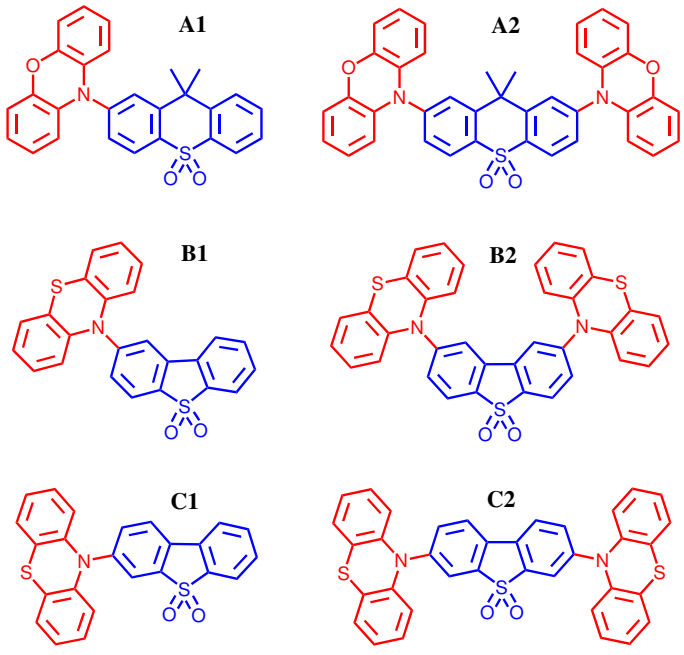

Figure 1.11: Molecules considered in this work. **A1**: PO-TXO2. **A2**: DPO-TXO2. **B1**: 2-PTZ-DBTO2. **B2**: DPTZ-DBTO2. **C1**: PTZ-DBTO2. **C2**: 3,7-DPTZ-DBTO2. In all molecules red and blue color refer to the donor and acceptor groups, respectively.

1.4.1 Computational Details

In this chapter, we consider three dipolar TADF emitters (**A1**, **B1** and **C1**) and their quadrupolar counterparts (**A2**, **B2** and **C2** respectively), as shown in Figure 1.11. For each emitter, single point TD-DFT calculations on the optimized ground state geometry are performed to obtain excitation energies (in the Tamm-Dancoff approximation),[67] both in gas phase and accounting for non-equilibrium solvation in PCM. All DFT and TD-DFT calculations are performed using Gaussian 16 B.01.[56] The optimized ground state structures of **A2**, **B2** and **C2** are obtained at the B3LYP/6-31G(d) level. Ground state geometries for **A1**, **B1** and **C1** are obtained substituting one of the donor units with an hydrogen atom. TD-DFT calculations are performed at the M06-2X/6-31G(d) level imposing the Tamm-Dancoff approximation.

1.4.1.1 Choice of the Functional

The choice of functional is a delicate issue for TADF molecules. Singlet-triplet (ΔE_{ST}) energy gaps as well as relative position of localised (LE) and charge transfer (CT) states largely depends on the chosen functional. Range-separated functionals were recently proposed to solve this issue.[68,69] We selected LC-ωPBE functional and found optimal ω (ω^*) for all dyes (listed in Table 1.2). Technical details about optimal ω computing could be found in Appendix A.[70]

	$\omega^*(\text{Bohr}^{-1})$
A1	0.1960
A2	0.1838
B1	0.1977
B2	0.1816
C1	0.1969
C2	0.1825

Table 1.2: Optimal ω values for dyes obtained using LC-ωPBE functional.

We have obtained excitation energy using LC-ωPBE and compared values with B3LYP,[71] M06-2X[72] and CAM-B3LYP's[73] output. Tamm-Dancoff approximation was used always for all excited state calculation.[74] Figure 1.12 shows excitation values with different functionals for all six dyes. For all molecules, B3LYP largely underestimates the energies of CT states and CAM-B3LYP overestimates them. In case of M06-2X, excitation energies are slightly overestimated compared to LC-ωPBE's values. Moreover, M06-2X gives similar trend of state energies (relative positition of LE/CT) compared to LC-ωPBE. Therefore we selected M06-2X functional for our studies. We underline that M06-2X was also reported

previously as a good functional for TADF molecules.[70]

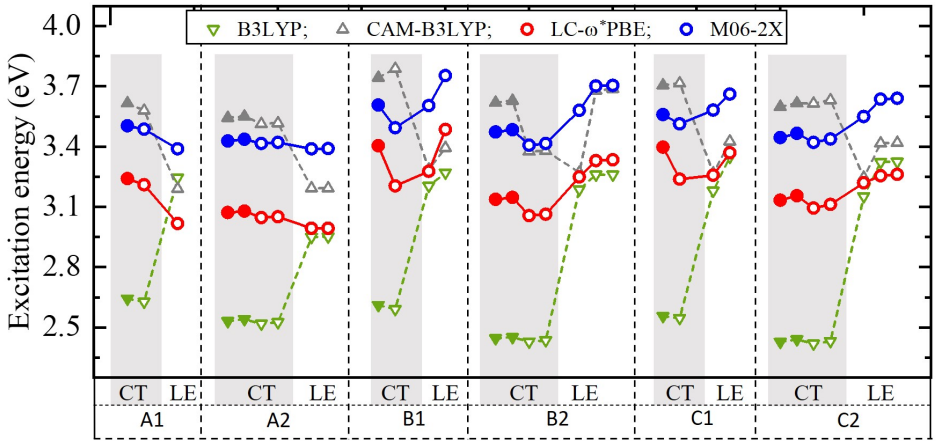

Figure 1.12: Excitation energies for dyes using different functionals - B3LYP (green), CAM-B3LYP (grey), LC-ω^*PBE (red), M06-2X (blue). Shaded area contains charge-transfer (CT) states and non-shaded area contains localized states (LE) with singlets (filled) and triplets (open), respectively.

1.4.1.2 Excitation Energies in Natural solvent under PCM

As discussed in Section 1.3, the ground state properties of the solute are not properly addressed when the adiabatic approximation is adopted to fast solvation. Three different implementations of PCM are currently available in the Gaussian package,[56] named LR, CLR and EI.[32,58] Since in current PCM implementations the ground state geometry is optimized in this approximation, leading to unreliable results, all data below are obtained for the optimized geometry in gas phase (see Figure 1.13). We have calculated excited states in natural solvent. Inconsistency and inversion of excited states are encountered under different solvation approaches.

Moreover, in order to exclude any contribution from polar solvation, we consider custom non-polar solvents, setting the static dielectric constant equal to the squared refractive index. Calculations are repeated for different values of the refractive index, η. Results are displayed as a function of $f(\eta^2) = (\eta^2 - 1)/(2\eta^2 + 1)$, the region corresponding to most organic solvents and polymeric hosts covering the $0.175 < f\left(\eta^2\right) < 0.225$ interval. We discussed this in next section.

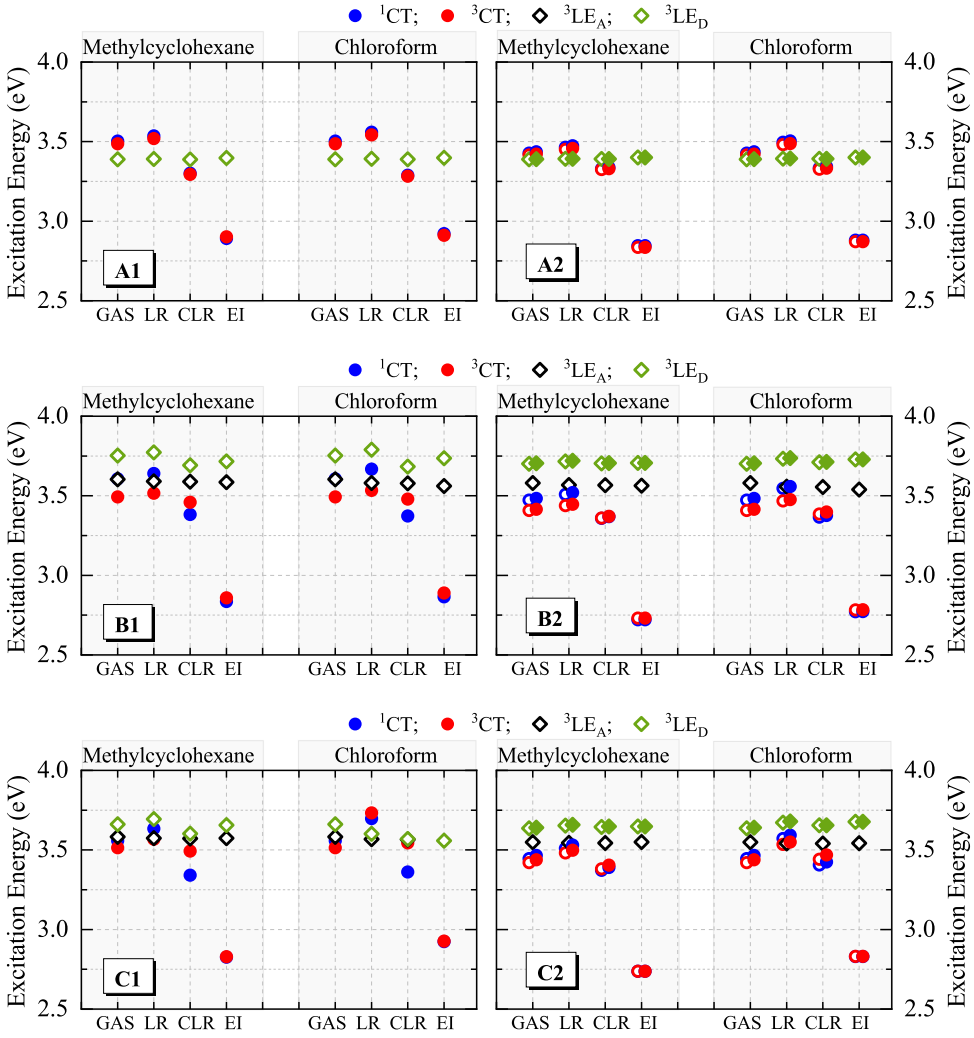

Figure 1.13: Excitation energy using different solvation formalism of dyes under PCM (Solvent: methylcyclohexane, chloroform)

1.4.2 Computational Results

1.4.2.1 PO-TXO2 (A1) and DPO-TXO2 (A2)

A1 and **A2** are TADF emitters with dipolar (D-A) and quadrupolar (D-A-D) structure, respectively, where A is 9,9-dimethylthioxanthene-S,S-dioxide (TXO2) and D is the phenoxazine (PO) group. The optimized ground state structure has the D and A moieties almost orthogonal. Both **A1** and **A2** have a negligible permanent dipole moment. Figure 1.14 shows the $f(\eta^2)$-dependence of the transition energies for the first few excitations of both molecules, calculated in the different implementations of PCM, discussed above. The nature of each state is defined with reference to the natural transition orbital (NTO), displayed in Figure B.1 and B.3 (Appendix B).

In gas phase, the lowest triplet excitation of **A1** at 3.389 eV is fully localized on the donor and has a negligible dipole moment; we call it ^{3}LE$_\mathrm{D}$. The second triplet at 3.487 eV and the lowest singlet at 3.504 eV are instead almost pure CT states, labeled ^{3}CT and ^{1}CT, respectively, and have a large permanent dipole moment oriented along the CT axis (see Table B.1 in Appendix B). Increasing $f(\eta^2)$, LR excitation energies marginally increase due to the solvent stabilization of the ground state, without any significant effect on the energies of the excited states. CLR and EI give qualitatively different results from LR: indeed already in non-polar solvents both approaches point to a different nature of the lowest excited triplet that becomes a CT state rather than an LE state. This has enormous spectroscopic consequences,[75–77] and it is important to realize that LR, the default approach to solvation, gives the wrong order of excited states for TADF dyes. In fact, not accounting for the large charge reorganization upon CT excitation, LR does not capture the large stabilization of CT states when going from gas-phase to condensed phases, leading to unreliable results already in non-polar media. On the other hand, CLR and EI lead to wildly different results, with energy differences ≈ 0.5 eV for typical $f\left(\eta^2\right)$ values for organic media. CLR and EI results for the energy gap between the lowest singlet and triplet states, ΔE_{ST}, are similar, even if largely different from the LR result.

In **A2**, the number of relevant excited states doubles with respect to **A1**, as symmetric and antisymmetric CT and LE$_\mathrm{D}$ states enter into play. In gas phase, the lowest triplets (≈ 3.39 eV) are two degenerate states localized on the donors, ^{3}LE$_\mathrm{D}$, while CT states are at higher energies: a pair of almost degenerate triplets, ^{3}CT, at ≈ 3.42 eV and a pair of singlets, ^{1}CT, at 3.428 eV and 3.436 eV. Despite the different structure and higher number of excited states, the dependence of LR, CLR and EI transition energies on $f(\eta^2)$ (Figure 1.14, right panel) can be explained in a similar way as for **A1**, with the caveat that EI and CLR corrections are due to the variation of the molecular quadrupolar moment of **A2** upon excitation. Once again, ΔE_{ST} results from CLR and EI calculations are similar but largely

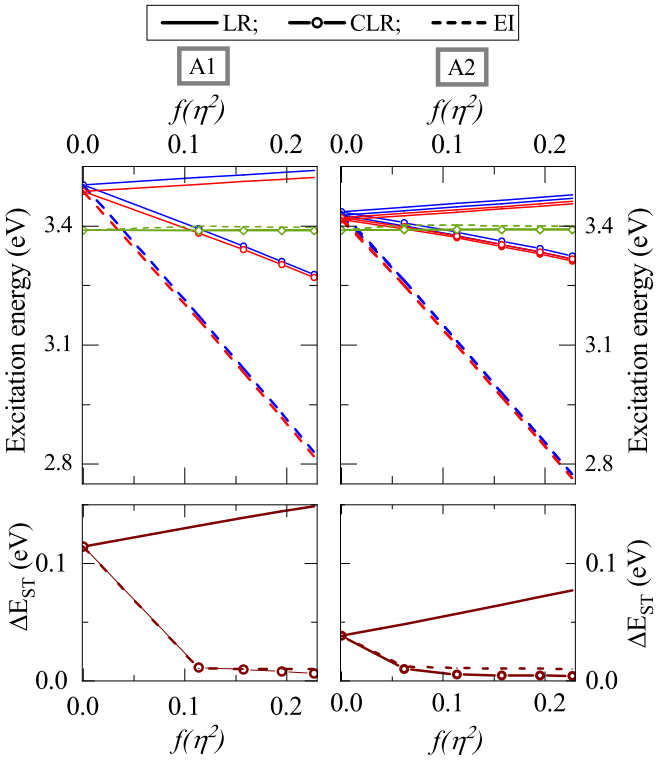

Figure 1.14: Results for **A1** (left) and **A2** (right) molecules. Top panels: excitation energies vs $f(\eta^2)$ for states ^{1}CT (blue), ^{3}CT (red), ^{3}LE$_D$ (green). Bottom panels: the calculated energy gap between the lowest singlet and triplet states. In all panels solid lines refer to LR, symbols refer to CLR, dashed lines refer to EI.

different from LR results.

1.4.2.2 2-PTZ-DBTO2, 2,8-DPTZ-DBTO2 (B1 and B2) and 3-PTZ-DBTO2, 3,7-DPTZ-DBTO2 (C1 and C2)

B1 and **B2** have been extensively studied both from a theoretical and experimental perspective.[75,76] The D and A units (phenothiazine, PTZ, and dibenzo[b,d]thiophene 5,5-dioxide, DBTO, respectively) are connected as shown in Figure 1.11. In the optimized ground state, D and A moieties lie on nearly orthogonal planes. Results for **B1** and **B2** are displayed in Figure 1.15. Several states must be considered for these systems. In fact the gas phase NTO and MO analysis (Figure B.4 and B.5) reveals that **B1** lowest triplet (3.493 eV) has a predominant CT character, so that we dub it as ^{3}CT, but with a non-negligible contribution from a local state. The next triplet, ^{3}LE$_A$, at 3.604 eV, is almost entirely localized on the A unit. The lowest singlet state at 3.607 eV, ^{1}CT, is a pure CT state, with a large

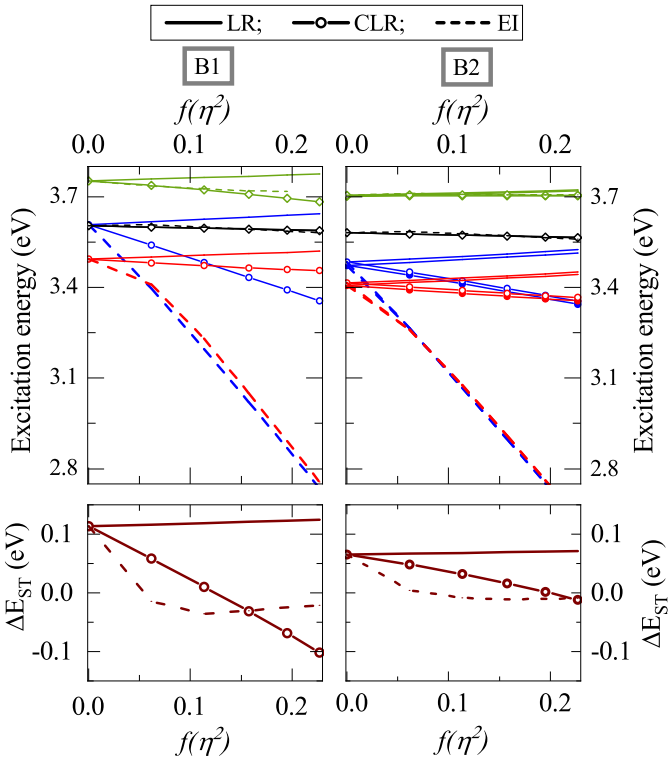

Figure 1.15: Results for **B1** (left) and **B2** (right) molecules. Top panels: Calculated excitation energies vs $f(\eta^2)$ for states ^{1}CT (blue), ^{3}CT (red), ^{3}LE$_A$ (black),^{3}LE$_D$ (green). Bottom panels: the calculated energy gap between the lowest singlet and triplet states. In all panels solid lines refer to LR, symbols refer to CLR, dashed lines refer to EI.

permanent dipole moment aligned approximately along the DA axis. The third triplet at 3.753 eV is a localized excited state on the D unit, ^{3}LE$_D$ state, with a non-negligible CT character. As before, the LR corrections to the excitation energies are minor for all states, in view of the very small transition dipole moments of relevant excitations. On the opposite, CT states are largely stabilized in CLR and EI but, as before, the two approaches yield very different results.

B2 is the quadrupolar counterpart of **B1** and more states enter into play. However, the nature and relative energies of the states in gas phase is similar in **B1** and **B2**. The lowest triplets ($\approx$ 3.41 eV) are mostly ^{3}CT, but have a non-negligible LE component, as shown from the NTO analysis (Figure B.6 in Appendix B). Interestingly, the low energy triplet in **B2** has a larger CT character than in **B1**. The next triplet at 3.580 eV is localized on A. The pair of degenerate ^{3}LE$_D$ states at $\approx$ 3.70 eV has a non-negligible CT component. The lowest singlets, ^{1}CT, at 3.473 eV and 3.484 eV are essentially pure CT states.

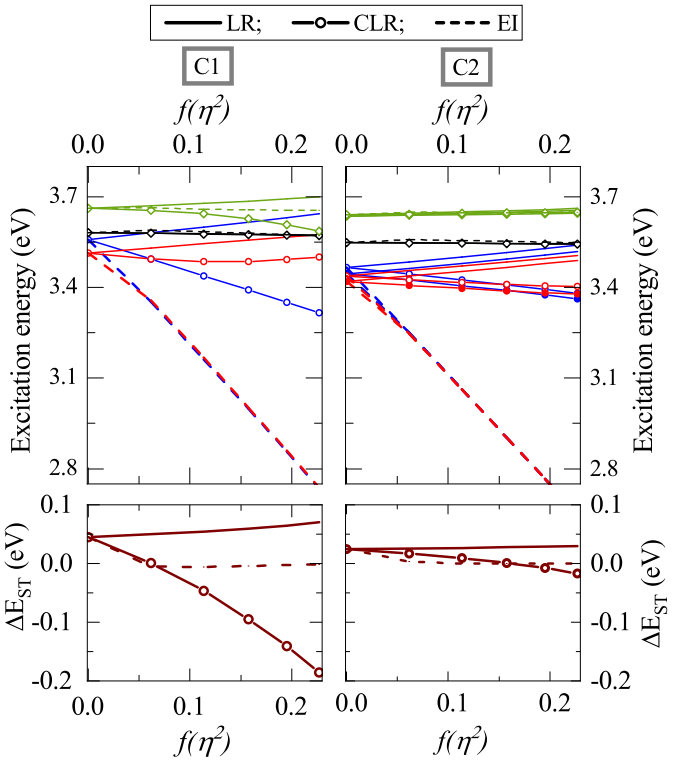

Figure 1.16: Results for **C1** (left) and **C2** (right) molecules. Top panels: Calculated excitation energies vs $f(\eta^2)$ for states ^{1}CT (blue), ^{3}CT (red), ^{3}LE$_A$ (black), ^{3}LE$_D$ (green). Bottom panels: the calculated energy gap between the lowest singlet and triplet states. In all panels solid lines refer to LR, symbols refer to CLR, dashed lines refer to EI.

As already discussed, LR corrections are negligible due to the very small transition dipole moments in TADF dyes. In CLR, corrections to the ^{3}LE$_A$ and ^{3}LE$_D$ states are also negligible. On the other hand, ^{3}CT and ^{1}CT states are stabilized as the transitions occur with a significant change in the charge distribution. However another serious problem emerges: both CLR and EI show an inversion in the order of the lowest singlet and triplet states. In other terms, according to these calculations, the lowest excited state of both **B1** and **B2** dissolved in an organic non-polar medium would correspond to a singlet and not to a triplet state. As discussed below, this result originates again from the mishandling of fast solvation. In **B1**, the lowest triplet has dominant CT character but with a sizable contribution from the triplet excitation localized on A, while the lowest singlet state is an almost pure CT state. The variation of the charge distribution upon excitation is therefore larger for the lowest singlet than for the lowest triplet excitation, leading to a larger stabilization of the singlet state with respect to the triplet state, with an effect that is most apparent in CLR. Indeed

in CLR the nature of the states is frozen, while in EI the nature of the states changes in the iterative process. Specifically, in our case, during the EI iterations the weight of the LE component in the lowest triplet state decreases, reducing ΔE_{ST}, that stays small but negative. In any case, the three implementations of the solvation model lead to very different values for ΔE_{ST}. Due to the larger CT component in ^{3}CT states in **B2** with respect to the same state in **B1**, the singlet-triplet inversion occurs at larger $f\left(\eta^2\right)$ values.

C1 and **C2** are very similar to **B1** and **B2**, respectively, as they share the same D and A units, even if connected in a different way. Result in Figure 1.16 are self explanatory now. NTOs (see Figure B.7 and B.9 in Appendix B) show a smaller mixing of local and CT triplet states than observed in **B1/B2**. Accordingly, for both **C1** and **C2**, ^{3}CT states have a larger weight of CT character than for **B1** and **B2**, resulting in larger charge separation. However, negative ΔE_{ST} are observed again with most prominent effects in CLR.

1.4.3 Antiadiabatic Approach to Singlet-Triplet Energy Gap

The scattering of the results obtained in the three current PCM implementations available in Gaussian package, the impossibility to calculate the transition dipole moment in the formally exact EI approach, addressed by limiting the analysis to first order perturbation theory in CLR, clearly point to some fundamental problem in solvation models, that can be traced back to the adiabatic approximation, as discussed in Section 1.3. To demonstrate that also the singlet-triplet inversion calculated in CLR and EI for some dyes in non-polar solvents is a spurious effect resulting from the adiabatic approximation to fast solvation, we focus on **B1** dye and compare adiabatic and AA results.

At present, AA implementations of PCM are not available, therefore, following the previous approach, we adopt a simplified model for the solvated molecule that relies on the dipolar approximation to describe the solute-solvent interaction and on the choice of a small electronic basis. With these approximations, we build a model that can be solved both in the adiabatic and in the AA approximation to fast solvation, allowing for a stringent comparison of the two approaches.

1.4.3.1 Few-State Model: LR, CLR and EI Approaches

To address the AA problem, we define a few state molecular model, writing the Hamiltonian in Equation 1.15 on the basis of the eigenstates of the gas-phase Hamiltonian. Specifically, we neglect spin-orbit coupling and consider two independent subspaces formed by the first n singlets and the first m triplets, as obtained from the TD-DFT calculation for the gas-phase molecule. On this basis H_{gas} is clearly diagonal. The dipole moment matrices were obtained using the MULTIWFN software.[78] Results of course depend on the number of states included in the basis sets and, since the diagonalization is performed independently in the

singlet and triplet subspaces, it is important to consistently choose the number of states in the two subspaces. Setting the same small number of states in both subspaces (Figure 1.17) indeed gives rise to the crossing of singlet and triplet states. The reason for this result is easily recognized in a basis that spans a much wider energy interval for the singlet vs the triplet subspace. Increasing the number of triplet states, so that the same energy window is roughly spanned in both subspaces, leads to more reliable results. Data in Figure 1.17 show that spanning a range of ~ 6 eV with 17 singlets and 26 triplets leads towards convergence.

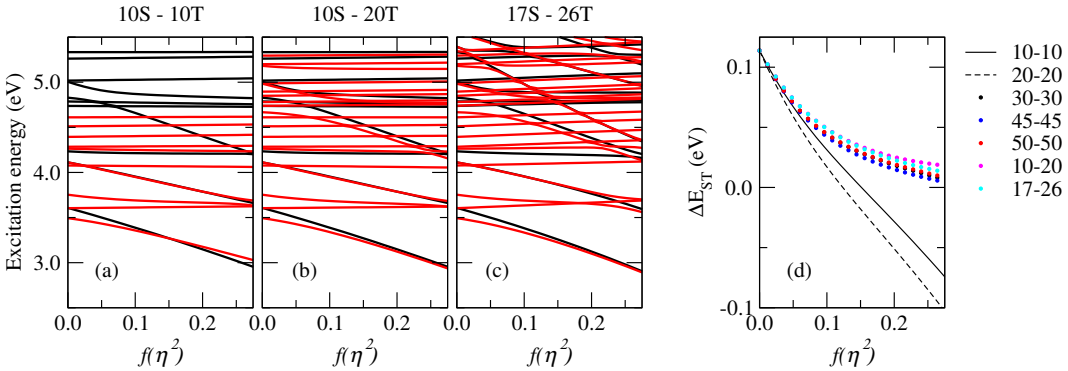

Figure 1.17: Antiadiabatic approach to fast solvation. Panels a, b and c: Transition energies of excited singlet (black) and triplet (red) states of **B1** as a function of $f\left(\eta^2\right)$. The three panels refer to results obtained truncating the electronic basis to the first (a) 10 singlet and 10 triplet states; (b) 10 singlets and 20 triplets; (c) 17 singlet and 26 triplets. Panel d: ΔE_{ST} as a function of $f\left(\eta^2\right)$ computed in the antiadiabatic approach for different number of excited singlet and triplet states as denoted in the legend.

In the LR approach the transition energy from the ground state, 1 to the j-th state is calculated from the frozen solvent transition energy, $\Delta E_{j1}^{(0)}$ as follows:

$$\Delta E_{j1}^{LR} = \Delta E_{j1}^{(0)} - r|\mu_{j1}|^2 \tag{1.18}$$

In CLR the correction to the transition energy is proportional to the square of the variation of the dipole moment upon excitation:

$$\Delta E_{j1}^{CLR} = \Delta E_{j1}^{(0)} - \frac{r}{2}(\mu_{jj} - \mu_{11})^2 \tag{1.19}$$

The EI approach equilibrates the fast solvation field around the excited state and calculates the transition energy as the energy difference between the equilibrated excited and ground states.

Right panels of Figure 1.18 collect AA results for **B1**, obtained setting the cavity radius to the Onsager's radius, $a = 5.44$ Å. These results clearly point to an excitation spectrum where the transition energies for the state with CT character (either singlet or triplet) are

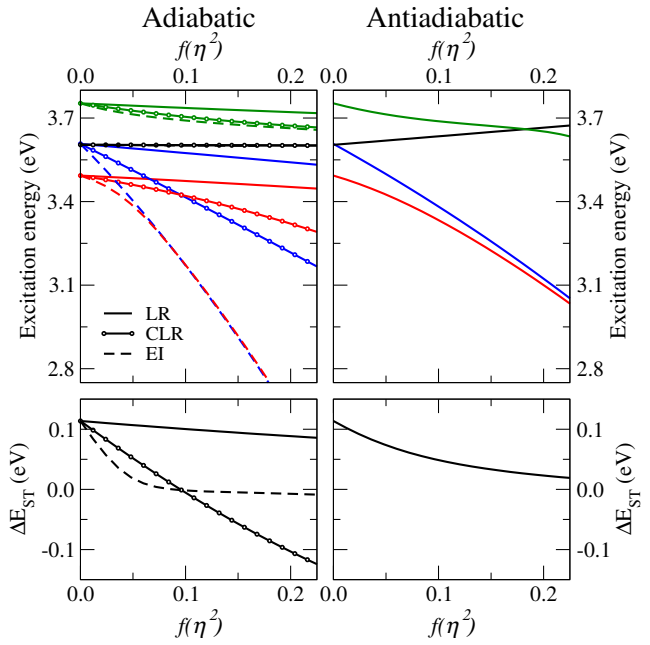

Figure 1.18: Comparison between adiabatic and AA results (left and right panels, respectively) for **B1** in the few state model accounting for 17 singlet and 26 triplet states. Top panels: Calculated excitation energies vs $f(\eta^2)$ for states ^{1}CT (blue), ^{3}CT (red), ^{3}LE$_A$ (black), ^{3}LE$_D$ (green). Bottom panels: the calculated energy gap between the lowest singlet and triplet states. In left panels (adiabatic results) solid lines refer to LR, symbols refer to CLR, dashed lines refer to EI.

lowered due to the medium polarizability while LE states are less affected. As expected, LR results are completely off for CT states. On the other hand, EI largely overestimates the stabilization of CT states and CLR underestimates it (see Figure 1.15). At variance with EI and CLR, AA results point to a normal order of excited states, with the lowest excited state having a triplet nature.

Comparing AA results in the right panels of Figure 1.18 with PCM results in Figure 1.15 may however be misleading due to the approximations introduced to build the few-state model adopted to run AA calculations. For a stringent comparison of AA and adiabatic approximations, left panels of Figure 1.18 show results obtained in the adiabatic approximation (and specifically in its LR, CLR and EI variants) for precisely the same model adopted for the AA approach (same basis set and dipole moment matrices).

The first observation is that adiabatic results in Figure 1.18 compare favourably with PCM results in Figure 1.15, suggesting that the adopted approximations capture most of the relevant physics. More important is however the comparison between adiabatic and AA results in Figure 1.18, relevant to the same model. Solvation effects on LE states are marginal,

but, as for CT states, neither EI nor CLR properly capture the stabilization of either the singlet or triplet states with differences in the estimated transition energies of several tenths of eV at $f(\eta^2) \sim 2$, as relevant to common organic media. Moreover, the singlet-triplet gap decreases considerably as a result of the medium polarizability, but at variance with CLR and EI results, it stays positive. Quite irrespective of the quality of the proposed molecular model, results in Figure 1.18 unambiguously demonstrate that the adiabatic approach, when applied to describe the spectroscopic effect of the medium polarizability, leads to unreliable results.

1.4.4 Discussion

TADF dyes are particularly delicate to model since the subtle interplay between localized and CT states makes environmental or matrix effects crucial in the definition of the tiny energies, the singlet-triplet gap and the spin-orbit coupling, that define the system performance.[38,70,75–77,79–82] Explicit-solvent quantum-classical approaches[38,39,83–90] are applied in several papers to investigate matrix effects in TADF-dyes. Even more popular are continuum solvation models, with LR,[80–82,91–99] CLR[100] and EI implementations.[16,83,84,99,101–103] As extensively discussed here, none of these approaches properly accounts for the electronic polarizability of the medium, leading to results that need a careful consideration.

Two main approaches are possible to separate the relevant DoF of the solute from the solvent DoF: an adiabatic and an antiadiabatic approach. Both approaches rely on the distinctively different dynamics of solute and solvent DoF. In the adiabatic approximation, one separates the relevant system (in our case the low-lying electronic excitations of the solute, typically in the visible and near-UV spectral region) from slow solvent DoF, so that the relevant Hamiltonian may be defined while maintaining the slow environmental DoF fixed. Accordingly, one diagonalizes several Hamiltonians as relevant to the different configurations of the slow DoF. This is indeed what is done in EI, where different molecular Hamiltonians are defined with the solvent DoF specifically equilibrated to each state, in an approach that is perfectly adequate to deal with polar solvation. As the name suggests, the antiadiabatic approximation applies to the opposite case, i.e. when the DoF to be renormalized away are much faster than the relevant ones. In this approximation one assumes that the solvent DoF readjust instantaneously to the motion of the relevant DoF. Therefore, a single Hamiltonian is defined for the relevant system in the antiadiabatic approximation.[35] This is very well apparent if one works with a basis of diabatic states, as in ref. 104: the antiadiabatic Hamiltonian describes a system where the fast DoF of the solvent are equilibrated to each diabatic basis state.

Here a fairly simple implementation of the AA approximation is introduced to demonstrate that the anomalous results obtained when the adiabatic approximation is applied to

fast DoF are quite naturally solved when the proper approximation scheme is adopted. To implement an AA calculation, a model is introduced, relying on a limited electronic basis and describing the solute-solvent interaction in the dipolar approximation. Moreover, the molecular geometry is always maintained fixed at the gas-phase equilibrium. Therefore, AA results in the left panel of Figure 1.18 must be taken with care and we do not pretend that they offer an accurate description of the system. Yet, the comparison with adiabatic results obtained for precisely the same model is solid and unambiguously demonstrates that the adiabatic approximation, implicitly adopted in all effective solvation models, leads to unreliable results.

Of special concern here is the inversion of the lowest singlet and triplet states calculated in the adiabatic CLR and EI implementations of PCM for some TADF-dyes. Indeed the breaking of the Hund rule was reported in some very special molecular systems, typically with highly symmetric structures and a very characteristic spatial separation of HOMO and LUMO orbitals that are delocalized on the whole molecular structure.[105–109] The molecules discussed here do not show these characteristics. Moreover, the singlet triplet inversion in these very special structures was only observed in high quality ab initio calculation, involving at least double excitations.[105,106] Quite interestingly, the inclusion of a standard TADF dye in a polarizable environment was also suggested as a possible origin for singlet-triplet inversion.[38,105] However these results were obtained and discussed treating the medium polarizability in the adiabatic approximation and deserve a careful reconsideration, either adopting the more adequate AA approximation or possibly addressing both the solute and its surrounding medium in a fully quantum mechanical approach.

1.5 Conclusions

Several variants of continuum solvation models are discussed in the literature,[26,30,32,36,58–60] that face the problem of fast solvation from slightly different perspectives, however, with the notable exception of early attempts,[46,47] all approaches rely on the diagonalization of molecular Hamiltonian obtained for a fixed potential from environmental charges. Whatever choice is made for the definition of the excited states of interest for absorption and emission processes, these methods are bound to fail, since the actual molecular states for a molecule in a polarizable environment should all be obtained diagonalizing a single Hamiltonian where the environmental polarizability affects in different ways the energy of the states of the systems and their coupling. Indeed, the adiabatic approximation leads to an incorrect description of the molecular ground state itself.[35] Just as an example, in polar dyes with a largely neutral ground state, the adiabatic approximation underestimates the increase of the ground state dipole moment as due to the polarizability of the environment,

simply because the equilibrium reaction field for a largely neutral ground state is small and cannot account for the large stabilization of polar charge fluctuations.[35] Similarly quantum-classical approaches with explicit solvent models do not properly account for the solvent polarizability, even when a *polarizable environment* is considered. In fact in polarizable models, one allows the charges on the solvent molecules to reorganize in response to the solute perturbation, but the molecular Hamiltonian is always defined accounting for a frozen potential generated by the surrounding charges.

While the adiabatic approximation can never be applied to electronic solvation, whose dynamics is faster than the relevant solute DoF, the AA approximation works well when the solvent degrees of freedom are much faster than the solute ones. The AA approximation therefore should be considered with care when the solvent excitation spectrum comes very close in energy to the solute spectrum, as it is the case for some matrices used in TADF applications. For common solvents and polymeric matrices used in spectroscopy, the UV-cutoff is typically larger (and often much larger) than 4 eV. Moreover, it must be recognized that the UV cutoff signals the frequency where the solvent absorption starts, the relevant absorption bands being located at much larger energy (just as an example, the water cutoff is at 6.5 eV, but the absorption spectrum peaks at $\sim$ 15 eV[110], with a large UV tail that moves the central frequency to $\sim$ 24 eV[35]). In systems where the AA approximation to fast solvation breaks down, due to similar timescales of the solute and solvent motions, the adiabatic approximation does not represents a viable alternative. Rather, solute and solvent degrees of freedom cannot be disentangled and one must resort to a full quantum mechanical approach to the solute and the solvent. Along these lines, the beautiful work reported in ref.[40] for water solvated dyes, offers another independent demonstration of the failure of the adiabatic approximation to fast solvation. In that work, a QM-MM approach is adopted, where the potential generated in the QM region by the charges on water molecules in the MM region is described (as usual) in the adiabatic approximation. In order to get reliable results, the solvation sphere described by QM must include a large number of water molecules (of the order of at least 200, depending on the solute and on the state of interest).

In the early 90's antiadiabatic approaches were proposed for fast solvation, but never gained traction.[46,47] Most probably, this is related to the choice of a wrong name for the approximation that was called Born-Oppenheimer rather than antiadiabatic. Indeed the Born-Oppenheimer approximation is a specific flavor of the most general adiabatic approximation that allows to separate slow DoF from relevant electronic DoF, through the definition of an electronic Hamiltonian that parametrically depends on slow coordinates.[41] It is true that also slow DoF are finally treated in the adiabatic approximation, but this is only possible after the adiabatic electronic Hamiltonian (defined for frozen slow coordinates) is diagonalized. Using the name Born-Oppenheimer to address an antiadiabatic approximation, where

instead a single electronic Hamiltonian is defined, was therefore unfortunate and may be the reason why the strategy was not recognized until very recently as the only viable approach to renormalize out the problem of the DoF related to fast solvation.

The term antiadiabatic, borrowed from the physics community working on polarons and superconductivity,[111] was used in the context of fast in 1999,[44] with reference to semiempirical model Hamiltonians, and was proposed again in the context of quantum chemical approaches.[35] Other authors have also recently recognized the value of the antiadiabatic approach to treat fast solvation.[112] Unfortunately, they stick on the Born-Oppenheimer notation, that obscures the qualitatively different nature of the antiadiabatic approach with respect to the adiabatic approximation. As extensively discussed in Ref. 35 the antiadiabatic approximation can be applied to solute DoF slower than the electronic DoF of the solvent, typically located deep in the UV (energies much larger than 6 eV): applying it to all electronic excitations in the solute is bound to fail, as also demonstrated in Ref. 112. However, a clever choice of the basis states can be made as to renormalize only relevant DoF, and, as the results in Figure 1.17 show for a specific example, converged antiadiabatic results can be obtained working in an energy window well within the critical threshold for common solvents.

Effective solvation models are of paramount importance in material science, since molecular properties are largely affected by the local molecular environment. Treating the active molecule and its environment on the same foot is a formidable task. Quantum-classical and continuum solvation models are therefore widely adopted in the community of computational chemists, physicists and material scientists. The main message of this work is a warning to these communities: the adiabatic approximation implicitly assumed in all these approaches to deal with fast solvation, i.e. to account for the medium polarizability, yields uncontrolled results, exemplified here by the prediction of a singlet excited state lying at lower energy than the lowest triplet state. The adiabatic approximation of course works very well to deal with slow solvation DoF, including e.g. polar solvation. However it cannot be applied to fast solvation: there is no way to improve on it. A different scheme, based on the antiadiabatic approximation, must rather be adopted.

Appendix A

Long-Range ω-tuned Functional

TD-DFT calculations based on different functionals lead to wildly different results for the excitation spectrum of TADF dyes, particularly with reference to the ΔE_{ST} value and, more generally, in terms of relative order of CT and local excited (LE) states.[113] Range-separated exchange functionals were suggested to solve the issue. In this approch, the range-separated parameter (ω) is optimally tuned to to get the exact exchange (eX) according to the inter-electron distance, r_{12}:[113]

$$\frac{1}{r_{12}} = \frac{1-[\alpha+\beta\,\mathrm{erf}(\omega\cdot r_{12})]}{r_{12}} + \frac{\alpha+\beta\,\mathrm{erf}(\omega\cdot r_{12})}{r_{12}} = SR + LR \tag{A.1}$$

where $erf(x) = \frac{2}{\sqrt{x}}\int_0^x exp(-t^2)dt$ and ω is range-tuning parameter.

The first term is the short-range (SR) component which is evaluated by DFT derived from local-density or generalized-gradient approximations. The second term is the long-range (LR) component which is evaluated by Hatree-Fock (HF). The α parameter quantifies the amount of eX in the SR limit, and $\alpha+\beta$ quantifies the amount of eX in the LR limit. The range-separation parameter ω defines the inverse distance at which exchange terms switch from DFT to HF. For any functional, $0 \leq \alpha \leq 1$, $0 \leq \beta \leq 1$ and $0 \leq \alpha+\beta \leq 1$. We use CAM-B3LYP ($\alpha = 0.19, \alpha+\beta = 0.65$), M06-2X (56% eX), B3LYP (20% eX) and LC-ωPBE ($\alpha = 0, \alpha+\beta = 1$) for comparison.[113,114] By deafult LC-ωPBE has a ω value of 0.4 $Bohr^{-1}$.[115,116] Now we tune this parameter to get the optimal ω (ω^*) using LC-ωPBE functional.

Baer *et al.* proposed a nonempirical method to get optimal ω by enforcing Koopmans' theorem,[117] stating that the negative HOMO energy, $-\varepsilon_H(N)$, of the N-electron system should be equal to the molecular vertical ionization potential, $IP(N)$ (see Figure A.1).

$$-\varepsilon_H^{\omega}(N) = IP^{\omega}(N) \tag{A.2}$$

Since, TADF molecules are donor-acceptor systems, it is useful to focus on ionization potential (related to donor component) as well as on electron affinity (related to acceptor

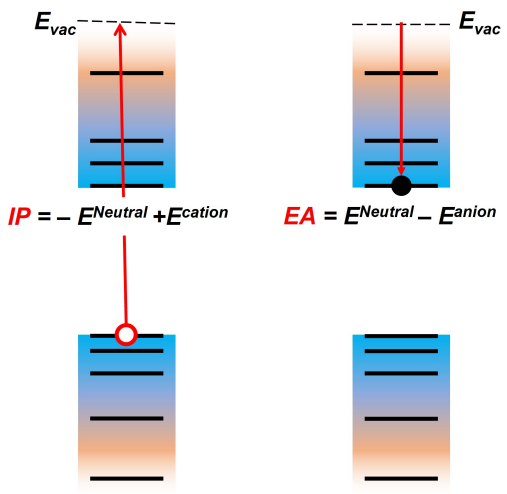

Figure A.1: Energies of molecular orbitals and its relation with ionization potential and electron affinity.

component). The vertical electron affinity of N-electron system, $EA(N)$ should be equal to the negative energy of HOMO energy of anion system, $-\varepsilon_H(N+1)$ (see Figure A.1).

$$-\varepsilon_H^{\omega}(N+1) = EA^{\omega}(N) \tag{A.3}$$

In optimal range-separated method, the goal is to minimize $J(\omega)$ defined as:

$$J^2(\omega) = |\varepsilon_H^{\omega}(N) + IP^{\omega}(N)|^2 + |\varepsilon_H^{\omega}(N+1) + EA^{\omega}(N)|^2 \tag{A.4}$$

We have performed our study using LC-ωPBE Figure A.2 shows ω vs. J^2 curve to get optimal ω ($\omega*$) for a few representative dyes considered in different chapters in this thesis. A detailed discussion on **DMAC-TRZ** is provided in Chapter 2, other dyes are discussed in Chapter 1 (Section 1.4). Optimal ω ($\omega*$) depends also geometry dependent. A more detailed discussion is presented in Section 2.3 for DMAC-TRZ molecule.

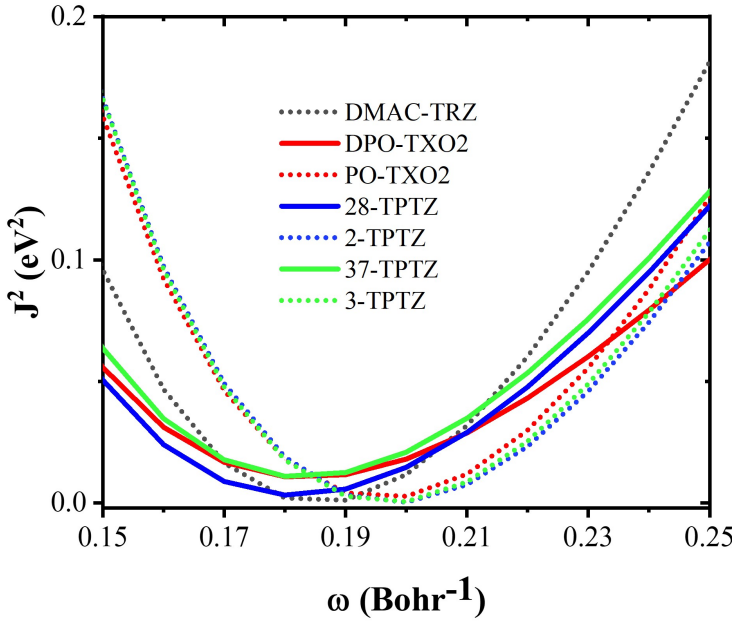

Figure A.2: ω vs. J^2 curve to get optimal ω ($\omega*$) for a few representative dyes considered in different chapters in this thesis. A detailed discussion on **DMAC-TRZ** is provided in Chapter 2, other dyes are discussed in Chapter 1 (Section 1.4)

Appendix B

Additional TD-DFT Results on TADF Dyes

B.1 Molecular Orbitals Analysis

B.1.1 Molecule: A1

State	HONTO		LUNTO	HONTO-1	LUNTO+1
^3LE_D 3.389 eV	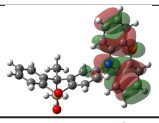	0.931 →	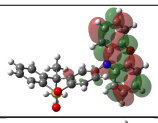		
^3CT 3.487 eV	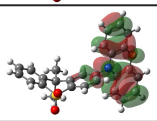	0.996 →	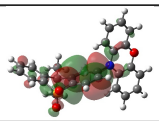		
^1CT 3.504 eV	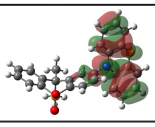	0.998 →	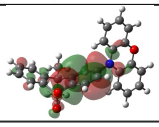		

Figure B.1: NTOs of **A1** molecule.

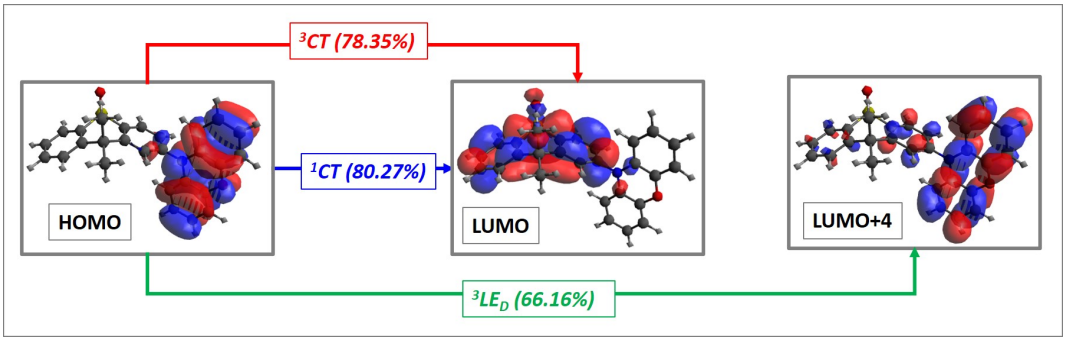

Figure B.2: Molecular Orbitals of **A1**

B.1.2 Molecule: A2

State	HONTO		LUNTO	HONTO-1		LUNTO+1
^3LE_D 3.389 eV	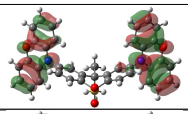	0.506	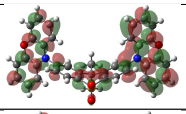	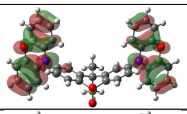	0.428	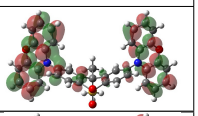
^3LE_D 3.390 eV	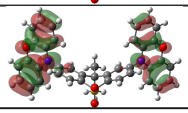	0.494	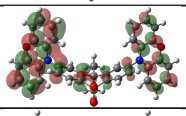	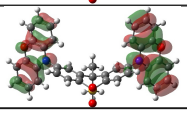	0.439	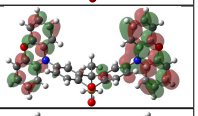
^3CT 3.416 eV	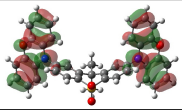	0.702	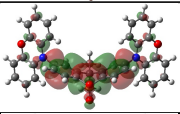	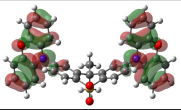	0.281	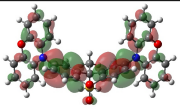
^3CT 3.421 eV	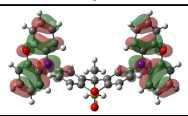	0.707	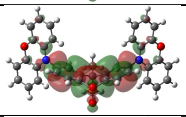	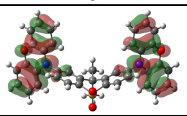	0.280	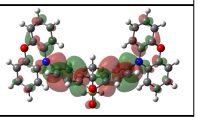
^1CT 3.428 eV	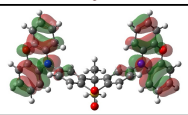	0.745	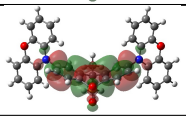	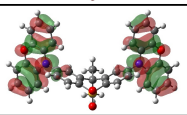	0.253	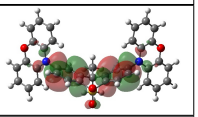
^1CT 3.436 eV	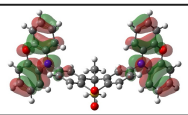	0.738	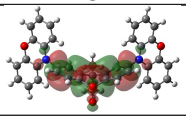	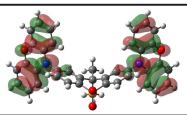	0.261	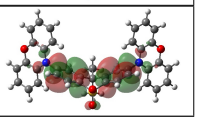

Figure B.3: NTOs of **A2** molecule (DPO-TXO2).

B.1.3 Molecule: B1

State	HONTO		LUNTO	HONTO-1	LUNTO+1
^{3}CT 3.493 eV	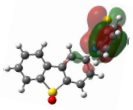	0.942 →	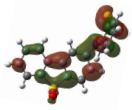		
^{3}LE$_A$ 3.604 eV	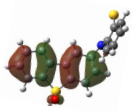	0.911 →	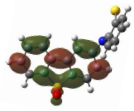		
^{1}CT 3.607 eV	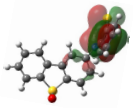	0.994 →	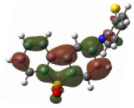		
^{3}LE$_D$ 3.753 eV	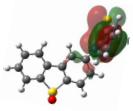	0.913 →	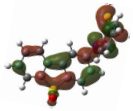		

Figure B.4: NTOs of **B1** molecule.

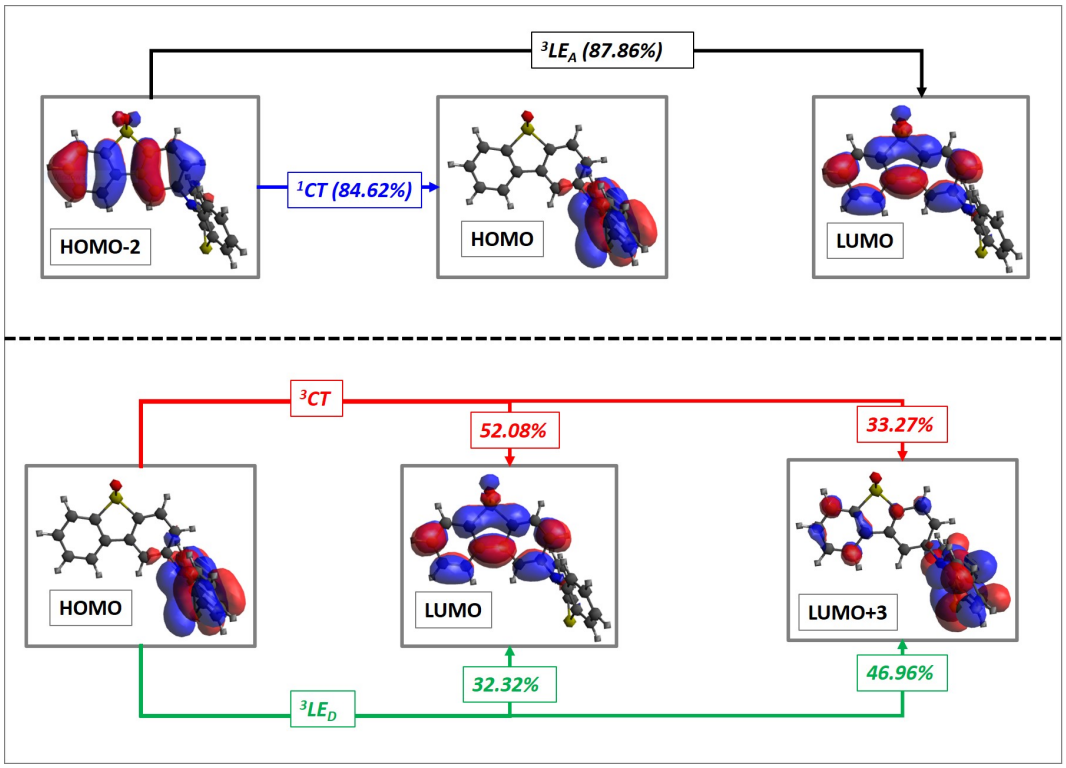

Figure B.5: Molecular Orbitals of **B1**

B.1.4 Molecule: B2

State	HONTO		LUNTO	HONTO-1		LUNTO+1
^{3}CT 3.407 eV	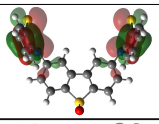	0.810 →	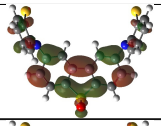	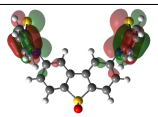	0.157 →	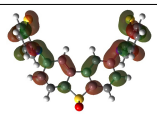
^{3}CT 3.415 eV	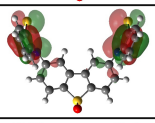	0.802 →	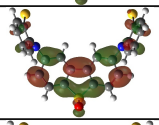	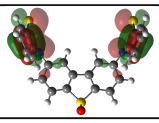	0.165 →	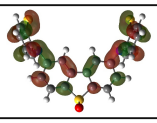
^{1}CT 3.473 eV	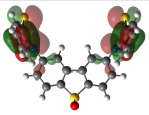	0.913 →	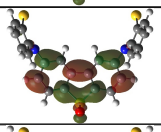			
^{1}CT 3.484 eV	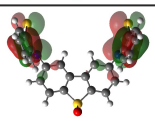	0.910 →	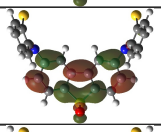			
^{3}LE$_A$ 3.580 eV	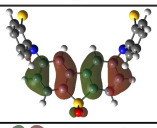	0.909 →	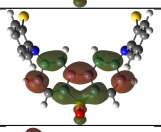			
^{3}LE$_D$ 3.702 eV	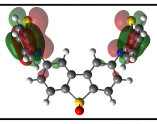	0.554 →	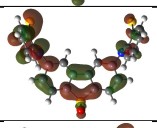	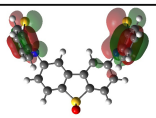	0.345 →	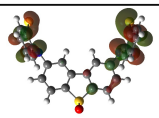
^{3}LE$_D$ 3.705 eV	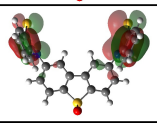	0.559 →	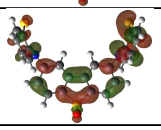	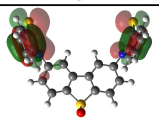	0.342 →	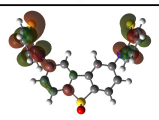

Figure B.6: NTOs of **B2** molecule.

B.1.5 Molecule: C1

State	HONTO		LUNTO	HONTO-1	LUNTO+1
^{3}CT 3.514 eV	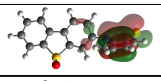	0.961	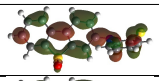		
^{1}CT 3.559 eV	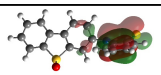	0.996	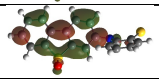		
^{3}LE$_A$ 3.582 eV	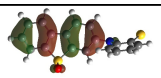	0.914	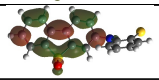		
^{3}LE$_D$ 3.662 eV	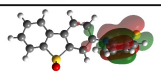	0.913	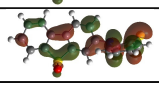		

Figure B.7: NTOs of **C1** molecule.

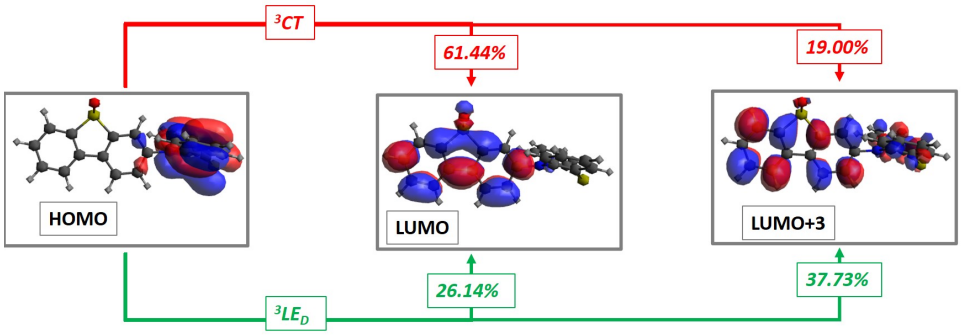

Figure B.8: Molecular Orbitals of **C1**

B.1.6 Molecule: C2

State	HONTO		LUNTO	HONTO-1		LUNTO+1
^{3}CT 3.420 eV	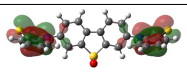	0.888 →	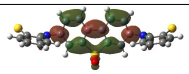			
^{3}CT 3.438 eV	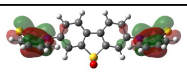	0.877 →	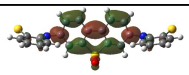			
^{1}CT 3.445 eV	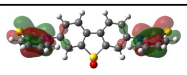	0.934 →	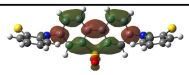			
^{1}CT 3.465 eV	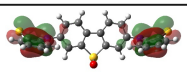	0.932 →	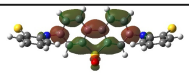			
^{3}LE$_A$ 3.549 eV	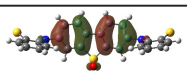	0.914 →	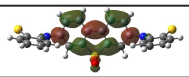			
^{3}LE$_D$ 3.636 eV	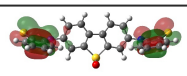	0.535 →	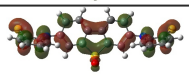	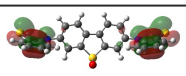	0.374 →	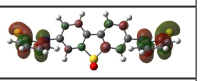
^{3}LE$_D$ 3.640 eV	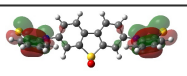	0.538 →	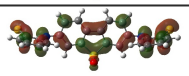	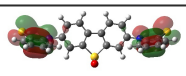	0.372 →	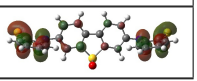

Figure B.9: NTOs of **C2** molecule.

B.2 Additional TD-DFT results

Selected TD-DFT results for the considered dyes (gas-phase result, M06-2X/6-31G(d)). TD-DFT analysis are obtained using Gaussian 16 B.01.[56] Transition dipole moment (TDM) and permanent dipole moments (PDM) of excited states are obtained using MULTIWFN software.[78]

B.2.1 A1 and A2

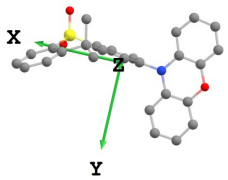

A1	Excitation energy (eV)	Permanent dipole moment (Debye) (x, y, z)	Transition dipole moment (Debye) (x, y, z)
S_0	–	(0.037, 2.413, 4.056)	–
^1CT	3.389	(-17.686, 4.430, 7.033)	(-0.559, 0.041, 0.069)
^3CT	3.487	(-17.214, 4.325, 6.945)	
^3LE_D	3.389	(0.147, 2.402, 4.080)	

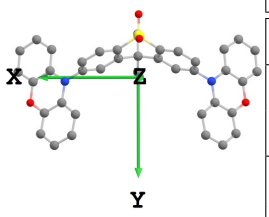

A2	Excitation energy (eV)	Permanent dipole moment (Debye) (x, y, z)	Transition dipole moment (Debye) (x, y, z)
S_0	–	(0.000, 2.179, -2.226)	–
^1CT	3.428 3.436	(0.085, 10.628, -8.565) (-0.085, 10.638, -8.555)	(-0.731, 0.000, 0.001) (0.003, -0.313, 0.250)
^3CT	3.416 3.421	(0.038, 9.261, -7.625) (-0.022, 9.612, -7.862)	
^3LE_D	3.389 3.390	(0.039, 3.319, -3.061) (-0.054, 2.961, -2.801)	

Table B.1: TD-DFT outputs for **A1** and **A2**. Molecules are shown with axis alongside (hydrogens are hided for simplicity).

B.2.2 B1 and B2

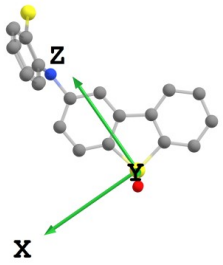

B1	Excitation energy (eV)	Permanent dipole moment (Debye) (x, y, z)	Transition dipole moment (Debye) (x, y, z)
S_0	–	(-2.501, 0.000, 2.647)	
^1CT	3.607	(1.570, 0.000, 22.306)	(0.000, -0.048, 0.000)
^3CT	3.493	(-1.028, 0.000, 12.950)	
^3LE_A	3.604	(-3.039, 0.000, 2.615)	
^3LE_D	3.753	(-0.734, 0.000, 12.745)	

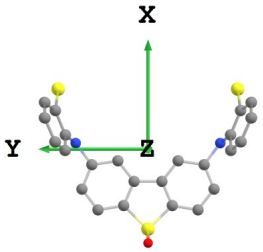

B2	Excitation energy (eV)	Permanent dipole moment (Debye) (x, y, z)	Transition dipole moment (Debye) (x, y, z)
S_0	–	(1.673, 0.029, 0.000)	–
^1CT	3.473	(16.503, 1.970, 0.000)	(0.000, 0.000, 0.065)
	3.484	(16.570, -1.980, 0.000)	(0.000, 0.000, 0.001)
^3CT	3.407	(13.131, 1.465, 0.000)	
	3.415	(12.978, -1.420, 0.000)	
^3LE_A	3.580	(1.921, 0.013, 0.000)	
^3LE_D	3.702	(6.017, 0.433, 0.000)	
	3.705	(6.250, -0.433, 0.000)	

Table B.2: TD-DFT outputs for **B1** and **B2**. Molecules are shown with axis alongside (hydrogens are hided for simplicity).

B.2.3 C1 and C2

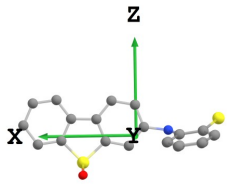

C1	Excitation energy (eV)	Permanent dipole moment (Debye) (x, y, z)	Transition dipole moment (Debye) (x, y, z)
S_0	–	(2.157, -0.002, 4.834)	
^1CT	3.559	(-20.043, -0.001, 2.547)	(-0.002, -0.106, 0.000)
^3CT	3.514	(-13.705, -0.002, 3.461)	
^3LE_A	3.582	(2.283, -0.001, 4.985)	
^3LE_D	3.662	(-6.139, -0.002, 4.937)	

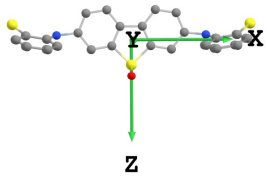

C2	Excitation energy (eV)	Permanent dipole moment (Debye) (x, y, z)	Transition dipole moment (Debye) (x, y, z)
S_0	–	(0.000, -0.001, -3.832)	–
^1CT	3.445	(-0.134, -0.001, -2.144)	(0.003, 0.000, 0.000)
	3.465	(0.134, -0.001, -2.192)	(0.000, 0.146, -0.001)
^3CT	3.420	(-0.140, -0.002, -2.373)	
	3.438	(0.141, -0.001, -2.468)	
^3LE_A	3.549	(0.001, 0.000, -3.883)	
^3LE_D	3.636	(-0.163, -0.002, -4.659)	
	3.640	(0.162, -0.002, -4.623)	

Table B.3: TD-DFT outputs for **C1** and **C2**. Molecules are shown with axis alongside (hydrogens are hided for simplicity).

Chapter 2

Understanding TADF of DMAC-TRZ

2.1 Introduction

TADF requires a delicate balance of several and sometimes competing interactions, as to ensure a tiny energy gap between the lowest excited singlet and triplet states, a large spin-orbit coupling between the same states, with the singlet showing reasonable emissive properties. The requirement of singlet and triplet states lying close in energy is easily met in dyes with low-energy charge transfer (CT) states, provided the conjugation between the electron-donor (D) and electron acceptor (A) is weak. Dyes with the D and A units arranged almost orthogonally were immediately recognized as target systems.[16–19] However, strictly orthogonal (non-conjugated) systems also have vanishingly small spin-orbit coupling between relevant states,[20] hindering RISC, as well as negligible transition dipole moments from the excited singlet to the ground state,[21] strongly suppressing emission intensity. An enormous effort towards the design of novel and more efficient TADF dyes includes multipolar dyes, where several D andor A groups are linked together in different geometries,[12] macromolecular and dendritic systems[22] also exploring the possibility of combining together different functionalities in the same molecular system towards TADF-dyes that may actively respond to diffent stimuli, including mechanical stress and pressure.[13]

Conformational flexibility, modulating the D-A conjugation, and hence affecting both the singlet-triplet energy gap and spin-orbit coupling is crucial to efficient TADF,[76,77,118] but, as first recognized by Monkman,[76,119] also local excited (LE) triplet states enter into the picture, mixing up with CT triplets to release the El-Sayed constraint of vanishing spin-orbit coupling between pure CT singlet and triplets.[77,81,120] LE states, at variance with CT state, are characterized by an excitation localized on either the D or A fragment. The presence of several states with different nature lying close in energy calls for a non-adiabatic approach to electron-vibration coupling, whose effects in speeding up RISC have been discussed recently.[75,121–124] To make the picture even more intricate, the matrix properties,

including dielectric properties, mobility, viscosity etc, may affect in different ways states with different nature, with dramatic effects on the relative energies of excited states, their mutual mixing etc.[38,98,125–130]. The concerted optimization of the active dye and its matrix requires a detailed understanding of several interconnected features and concurrent forces towards the precise control of the tiny energy gaps, and of the tiny interactions that govern TADF efficiency. This challenging endeavor must rely on a careful and critical exploitation of several tools available to the theoretician, validating against a large body of experimental data the adopted approaches and relevant results.

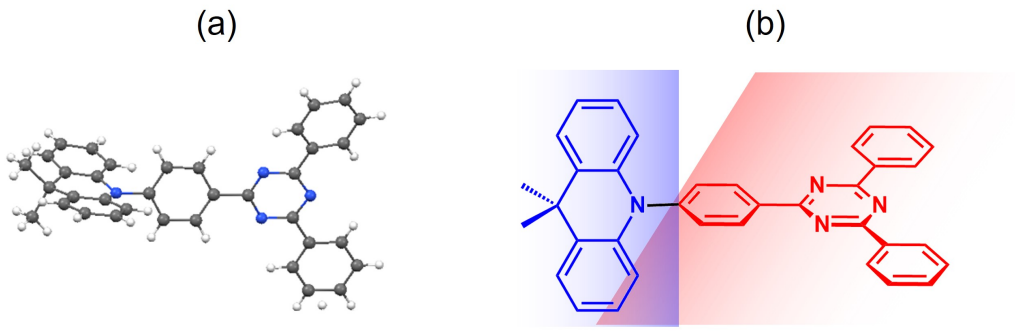

Figure 2.1: (a) Crystal structure and (b) molecular structures of 10-(4-(4,6-Diphenyl-1,3,5-triazin-2-yl)phenyl)-9,9-dimethyl-9,10-dihydroacridine (**DMAC-TRZ**).

This chapter presents a first step in this direction for a representative TADF dye,[11,131] **DMAC-TRZ** in Figure 2.1. Here I present a detailed computational analysis of the dye supported by experimental data are collected by experimentalists in host lab. The information obtained along the two paths were finally combined in a reliable complete model for the system. Our developed model for **DMAC-TRZ**, accounts for low-lying electronic excited states, a conformational degree of freedom, a coupled molecular vibration while addressing environmental effects. This model is developed for a prototypical D-A dye, but sets a sound basis for modeling multipolar dyes. In these systems, the synthetic flexibility due to the presence of multiple D and A moieties in the same molecule in a variety of different geometries has an enormous potential towards the optimal design of TADF dyes,[12] but can only be fully exploited if reliable structure-properties relations emerge from a deep understanding of the physics of the dye, including its interaction with the surrounding medium.

2.2 Optical Spectroscopy

DMAC, **TRZ** and **DMAC-TRZ** were acquired from Merck, and used without further purification. Spectroscopic data were collected in solution using HPLC-grade solvents from

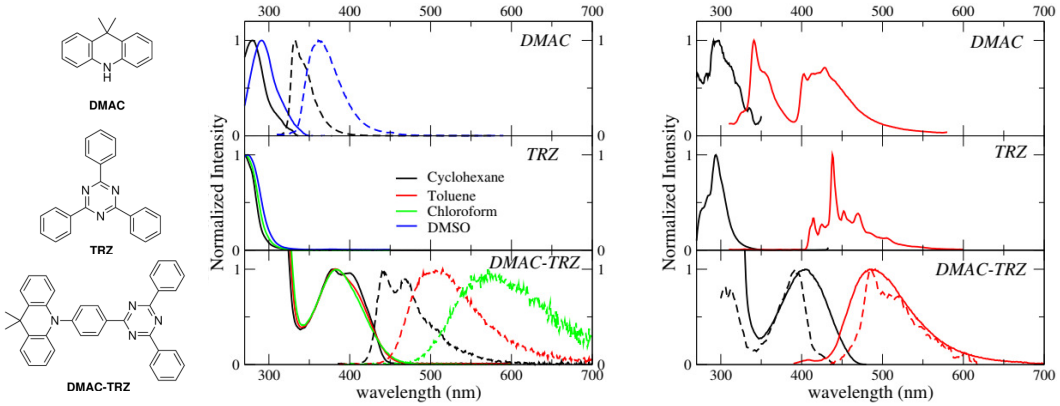

Figure 2.2: Left: molecular structures of 9,9-dimethyl-9,10-dihydroacridine (**DMAC**), 2,4,6-triphenyl-1,3,5-triazine (**TRZ**) and **DMAC-TRZ**. Central panels: absorption (continuous lines) and emission spectra (dashed lines) of **DMAC**, **TRZ** and **DMAC-TRZ** in solvents of different polarity. Toluene, with a cut-off wavelength of 285 nm, is not suitable for **DMAC** and **TRZ**. Moreover, **DMAC** is not stable in chloroform, while the emission of **DMAC-TRZ** in DMSO is very weak. Right panels: excitation (black) and emission (red) spectra of **DMAC-TRZ** in 2MeTHF at 77 K. Dashed lines in the bottom panel report gated measurements, collected with a gate delay of 1 s and a gate width of 7 s.

Merck. Absorption spectra were recordered with a Perkin Elmer Lambda 650 spectrophotometer. Steady-state and time-resolved luminescence spectra (including anisotropy) were recordered on dilute solutions (absorbance lower than 0.1) with a FLS1000 Edinburgh Fluorometer equipped with a gated PMT detector. Low-temperature measurements were collected on glassy matrices of 2MeTHF at 77K (the solvent was stored over molecular sieves for one night, and filtered before use), that were fastly cooled using an Oxford Instrument OptistatDN cryostat.

Room temperature absorption and fluorescence spectra of **DMAC-TRZ**, and of the two subunits, **DMAC** and **TRZ** (Figure 2.2), dissolved in solvents of different polarity (cyclohexane, toluene, chloroform and DMSO) are shown in the central panels of Figure 2.2 and relevant data are summarized in Table 2.2. **TRZ** is not emissive at room temperature. Both **DMAC** and **TRZ** are transparent at $\lambda > 350$ nm, so that the weak **DMAC-TRZ** absorption band (molar extinction coefficient ~ 2000 L mol^{-1}cm^{-1}, Table 2.2) observed at 380 nm is safely assigned to a CT band. Its marginal solvatochromism points to a very small permanent dipole moment for **DMAC-TRZ**,[132] in line with a largely neutral ground state (i. e. a ground state where the contribution from the charge-separated zwitterionic **DMAC**$^{+}$**-TRZ**$^{-}$ structure is negligible). On the opposite, **DMAC-TRZ** emission shows a large red-shift upon increasing the solvent polarity: the emission is therefore ascribed to a CT state, a state

Compound	Solvent	λ_{abs} [nm][a]	λ_{em} [nm][b]	Quantum Yield	Lifetime [ns]	Molar Extinction Coefficient [L mol^{-1}cm^{-1}]
DMAC	Cyclohexane	280	332	-	2.1 (10.1%) 3.9 (89.9%)	-
	DMSO	291	361	-	3.6 (4.6%) 7.8 (95.4%)	-
TRZ	Cyclohexane	269	-	-	-	-
	Chloroform	271	-	-	-	-
	DMSO	274	-	-	-	-
DMAC-TRZ	Cyclohexane	380	442	0.22	9.8 (99.6%) 84.5 (0.4%)	-
	Toluene	382	510	0.18	12.7 (97.5%) 62.1 (2.5%)	1990
	Chloroform	382	571	0.23	14.4 (75%) 120.1 (25%)	2180
	DMSO	385	-	-	-	2250

Table 2.1: Spectroscopic data for **DMAC**, **TRZ** and **DMAC-TRZ**. [a] maximum absorption wavelength, [b] maximum emission wavelength.

with a largely zwitterionic character and hence a large permanent dipole moment. The emission is safely ascribed to fluorescence, in view of its lifetime $\sim$ 10 ns (Table 2.2 and upper panel of Figure 2.3). Indeed an emission component with longer lifetime is observed, with a sizable weight in chloroform, suggesting a possible delayed fluorescence contribution, as also supported by time resolved emission spectra (lower panel of Figure 2.3) whose shape and position are time-independent.

The different emission bandshapes observed in polar and non-polar solvents are sometimes ascribed to an emissive state whose nature changes from LE to CT. This is easily ruled out by fluorescence excitation spectra (Figure 2.4): it is clear that, in all solvents, emission comes from the same CT state responsible for absorption. Indeed, the broadening of the emission band with increasing solvent polarity is due to the inhomogeneous broadening related to polar solvation.[133–135]

To address long-lived emission, including delayed fluorescence and phosphorescence, spectra were collected in a glassy 2MeTHF matrix at 77 K, as shown in Figure 2.2 (right panels). **DMAC** shows two separate emission bands: the short wavelength band (lifetime: 5.2 ns (38%) and 15.4 ns (62%) is due to fluorescence, while the long-wavelength band (lifetime 4 s) is ascribed to phosphorescence. A single long-lived emission (lifetime 1 s) is observed for TRZ, in the blue-green spectral region, again ascribed to phosphorescence. The

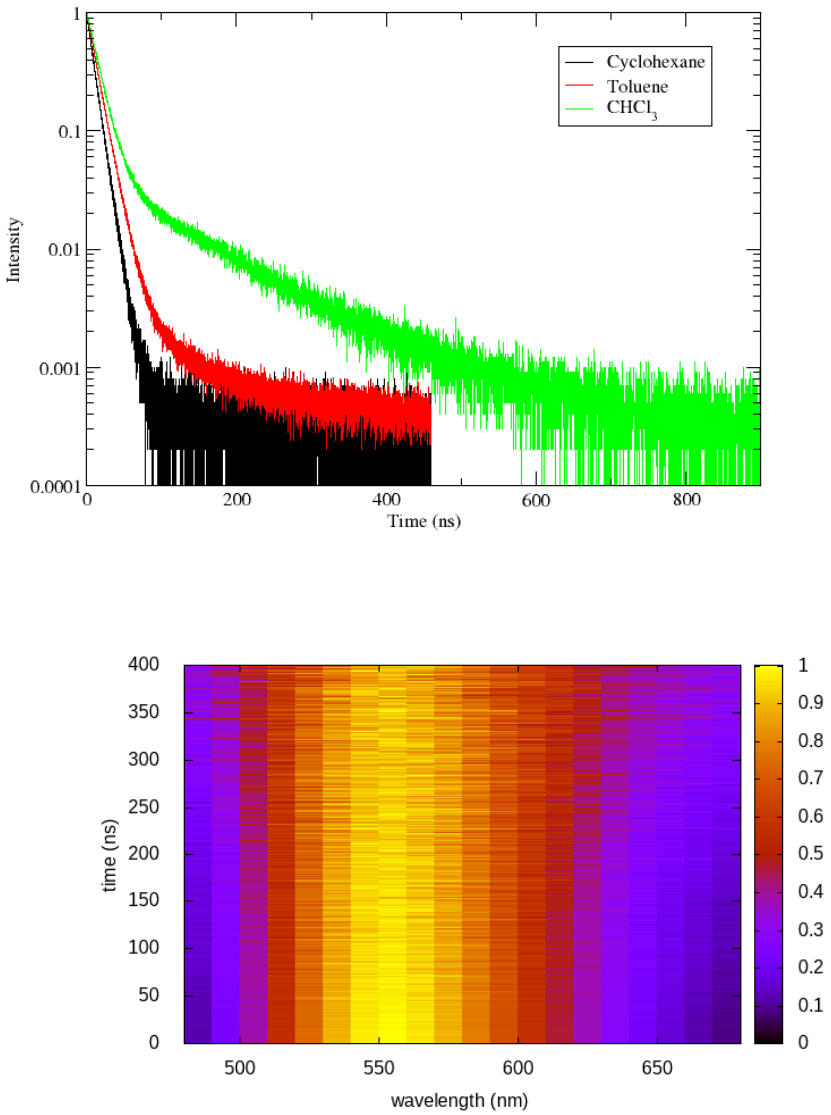

Figure 2.3: Fluorescence intensity (excitation 375 nm, detection at the maximum of emission for each solvent) vs time for **DMAC-TRZ** in different solvents. Lower: Time resolved emission spectra of **DMAC-TRZ** in chloroform.

emission observed for **DMAC-TRZ** at 485 nm, in a spectral region where neither **DMAC** nor **TRZ** emit, is clearly CT in nature. The emission decay (Figure 2.6) shows a short (of the order of ns) and a long (of the order of s) lifetime component in the same spectral region. Time resolved emission spectra are reported in Figure 2.7. After a marginal red shift in the first few tenths of ns, the emission profile is constant in time over several order of

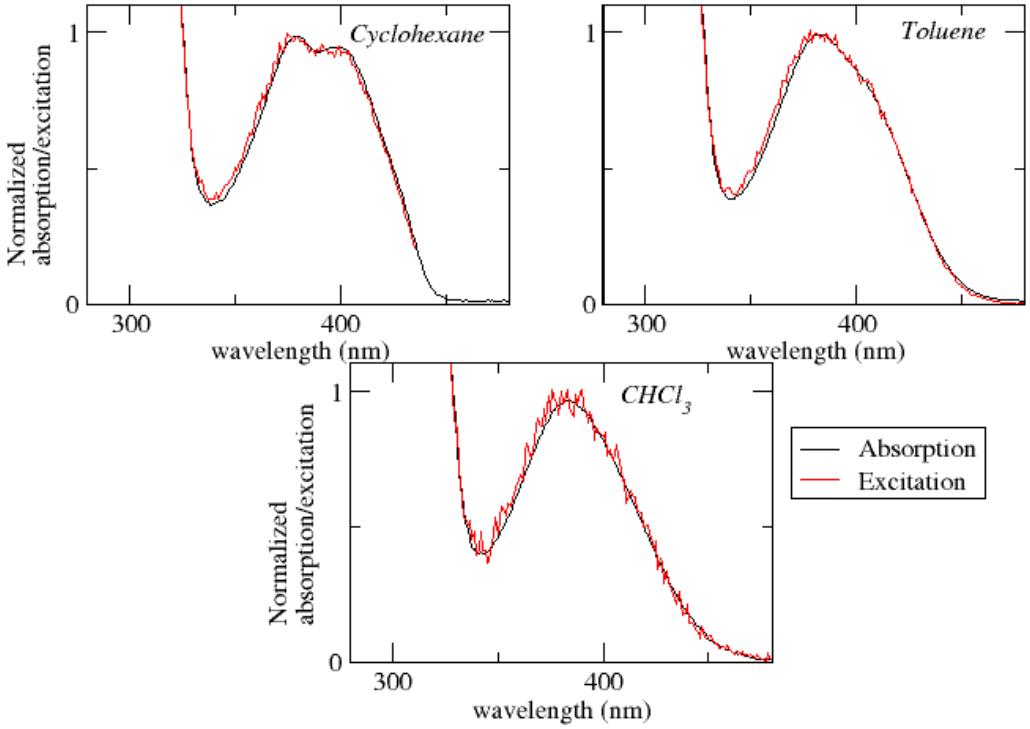

Figure 2.4: Absorption and fluorescence excitation spectra of **DMAC-TRZ** in different solvents.

magnitudes, as expected for TADF. Then, at ∼0.1 s the emission bandshape narrows appreciably. Dashed lines in the bottom right panel of Figure 2.2 show emission and excitation spectra obtained collecting photons reaching the detector 1 s after the excitation (gated measurements, collected with a gate delay of 1 s and a gate width of 7 s). These long-delayed emission spectra are again superimposed to steady-state emission, even if with narrower bandshape, suggesting either a delayed fluorescence (even if with an unusually long lifetime) or a phosphorescence occurring in the same spectral region as fluorescence. Irrespective of the nature of this long-lived emission, the relevant excitation spectrum peaks in the same spectral region as the steady state excitation spectrum of **DMAC-TRZ**, i.e. in a region where neither **DMAC** nor **TRZ** show any absorption feature, demonstrating a dominant CT nature for the long-lived emission.

To gain more information on the nature of the long-lived states, Figure 2.5 shows time resolved fluorescence anisotropy spectra collected up to 2 s. Anisotropy remains constant at $\sim$ 0.25 up to at least 10 ms, and then decreases. The constant and large value of the

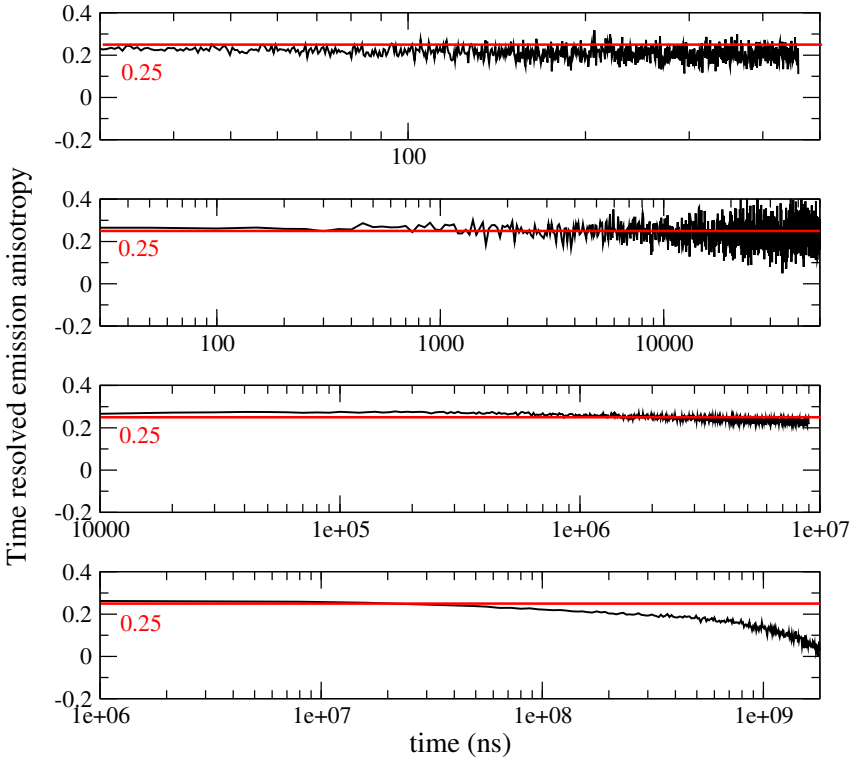

Figure 2.5: Time-resolved anisotropy of **DMAC-TRZ** collected in 2MeTHF at 77 K in different time ranges (excitation wavelegth 405 nm, emission wavelength 485 nm).

emission anisotropy over 6 orders of magnitude in time (from ns to ms), and the invariance of emission spectra in the same temporal windows (Figure 2.7) unambigously point to the observation of delayed fluorescence up to $\sim$ 10 ms. At longer times, the anisotropy decreases (Figure 2.5 bottom panel), and the shape of emission spectra (but not their position) changes (Figure 2.7, and Figure 2.2), offering a clear evidence of the involvement of a different emissive state, corresponding to a very long-lived triplet state. As discussed above, this triplet state has a CT nature, since the corresponding excitation spectrum (black dashed line in Figure 2.2) is distinctively red-shifted with respect to the absorption spectra of either **DMAC** or **TRZ** subunits. The marked decrease of the anisotropy for the phosphorescence signal can be understood in terms of a small mixing of the CT triplet state with an LE triplet. Transition dipole moments associated with (weak) CT transitions are orders of magnitude smaller than those relevant to LE states: even a weak LE contribution to the phosphorescent state would dominate the observed transition dipole moment, being therefore responsible for its rotation with respect to the CT direction.

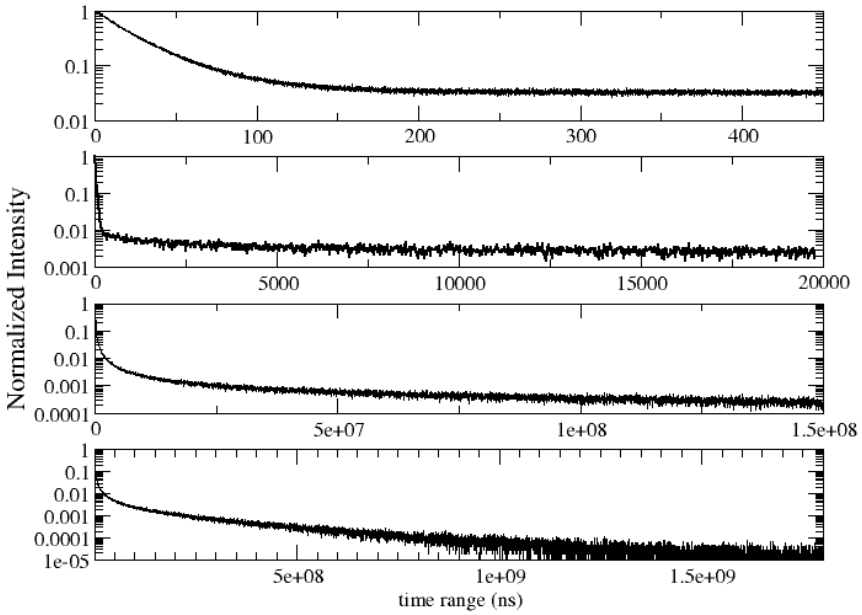

Figure 2.6: Fluorescence intensity (excitation: 405nm, emission 485nm) collected for **DMAC-TRZ** in 2MeTHF at 77K on different time ranges.

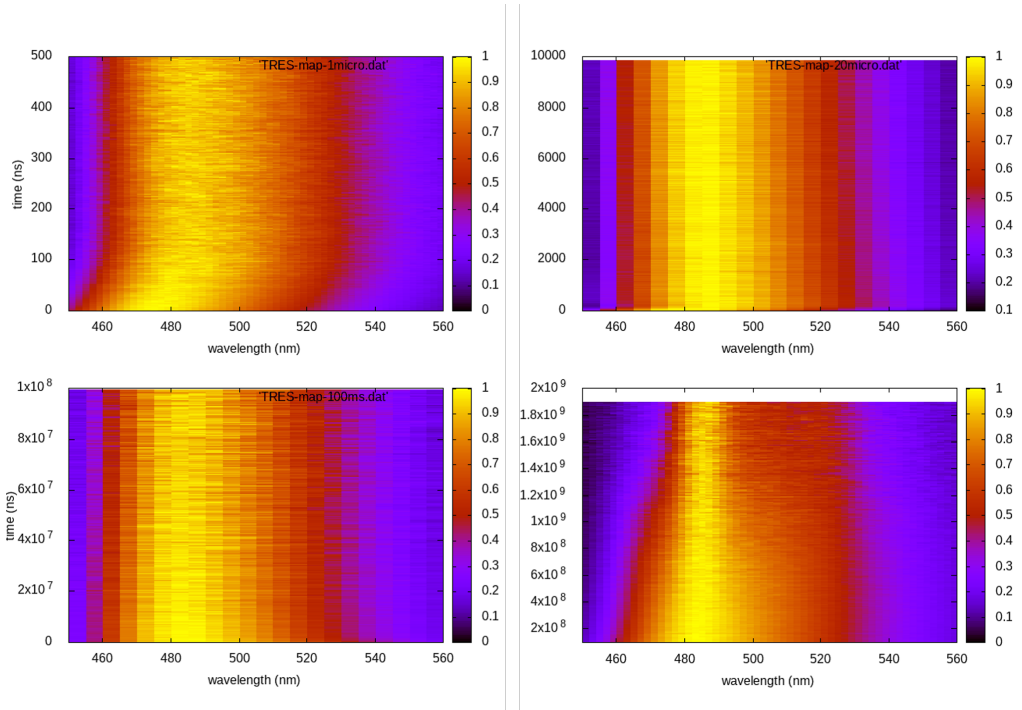

Figure 2.7: Time resolved emission spectra of **DMAC-TRZ** in 2-Me-THF at 77K in different time ranges.

2.3 Computational Analysis

The ground state geometry of **DMAC-TRZ** is optimized in DFT (M06-2X/6-31G(d)) in Gaussian 16 B.10.[56] Spin-orbit coupling (SOC) in **DMAC-TRZ** is calculated using M06-2X/6-31G(d). All calculations are performed under TD-DFT within Tamm-Dancoff approximation. The default Breit-Pauli Hamiltonian is adopted to calculate SOC between TD-DFT states in Orca 4.1 package.[136,137] Avogadro[138] was used as visualization tool.

The equilibrium dihedral angle, θ in Figure 2.9a, amounts to 90°, suggesting a negligible delocalization of electrons between the donor (**DMAC**) and acceptor (**TRZ**) units. To address excited states in such a large molecule, TD-DFT is the method of choice and, being interested in both singlet and triplet states, we adopt the Tamm-Dancoff approximation.[67]. The most delicate issue is the choice of the functional. Recent studies propose the use of range-separated exchange functionals to solve the problem for CT states, optimizing ω, the range-separation parameter, for each molecule of interest.[23–25]. Fairly reliable results for TADF-dyes are obtained in the optimal long-range corrected PBE (LC-ω^*PBE).[25]

Excitation energies of **DMAC-TRZ**, reported in Figure 2.9b for the lowest singlet and triplet states, are obtained for the optimized ω=0.195 value (Table 2.2) and are compared with results obtained with B3LYP,[71] CAM-B3LYP[73] and M06-2X functionals.[72] While all functionals find almost degenerate singlet and triplet states with a dominant CT character, the relative energies of CT and LE states change wildly, with B3LYP and PBE0 largely underestimating the energy of CT states and CAM-B3LYP overestimating it. M06-2X slightly overestimates all transition energies, but gives a very similar trend as LC-ω*PBE functional for the excitation energies of singlet and triplet states. Results in Figure 2.9b refer to the equilibrium geometry, $\theta = 90°$, but optimal ω is geometry dependent.[139]. So, we calculated the optimal ω for dihedral angles of 75°, 60°, 45° and compare with other functionals. Optimal ω values are listed in Table 2.2 and plots for transition energy calculated for different dihedral angles and functionals are shown in Figure 2.8. Similar results were obtained for selected values of the dihedral angle (Figure 2.8). On this basis, M06-2X is adopted as functional of choice.

Dihedral angle	ω
90°	0.195
75°	0.195
60°	0.190
45°	0.185

Table 2.2: Optimal ω values estimated for different geometries

Figure 2.9 summarizes main TD-DFT results. At the equilibrium geometry, the planes

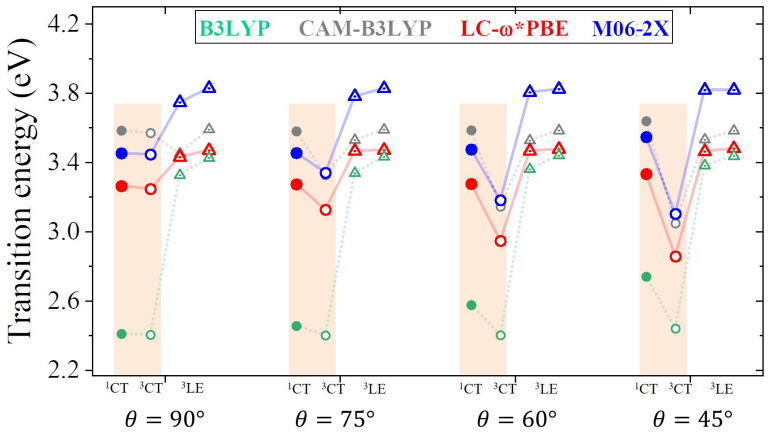

Figure 2.8: Excitation energies of the four lowest excited states calculated with different functionals and for different θ values.

of **DMAC** and **TRZ** moieties are mutually orthogonal ($\theta = 90°$) and the lowest lying singlet and triplet states (S_1 and T_1, respectively) are almost degenerate. The next excited state T_2, at 3.75 eV (not shown in the figure), is again a triplet. Based on relevant natural transition orbitals (Figure 2.9d) we describe the two lowest and almost degenerate singlet and triplet states as CT states (^{1}CT and ^{3}CT, respectively), while the next excited state is a triplet state localized on donor unit (^{3}LE$_D$). To further confirm the nature of the states, Figure 2.9e shows the evolution of the energies of the lowest states vs an electric field applied along the D-A axis. The energy of the ground (S_0) and of the T_2 state marginally depends on the applied field, suggesting that the two states have a very small permanent dipole moment, confirming the local nature of T_2. On the opposite, the large and almost linear dependence of the energy of S_1 and T_1 states on the applied field, points to a large and almost constant dipole moment for both states, confirming their CT nature.

The pure CT nature of the lowest singlet and triplet states accounts for a vanishing singlet-triplet gap, $\Delta E_{ST} = 0$, but, according to the El-Sayed rule,[20] it also implies a negligible spin-orbit coupling, hindering RISC and hence TADF. To better understand the physics of TADF in **DMAC-TRZ**, we therefore calculate the energies of the relevant states upon varying the dihedral angle, while keeping the geometry of the two fragments fixed. Results in Figure 2.9c are interesting in several respect. First of all, the potential associated to the ground state and to the first singlet state is fairly flat, suggesting considerable thermal configurational disorder. Moreover, a double-minimum structure is observed for the lowest triplet state: the equilibrium conformation for the relaxed triplet has a twist angle $\theta \sim 60°$ or $120°$. As discussed in the next section, this variation of conformation in the triplet state can

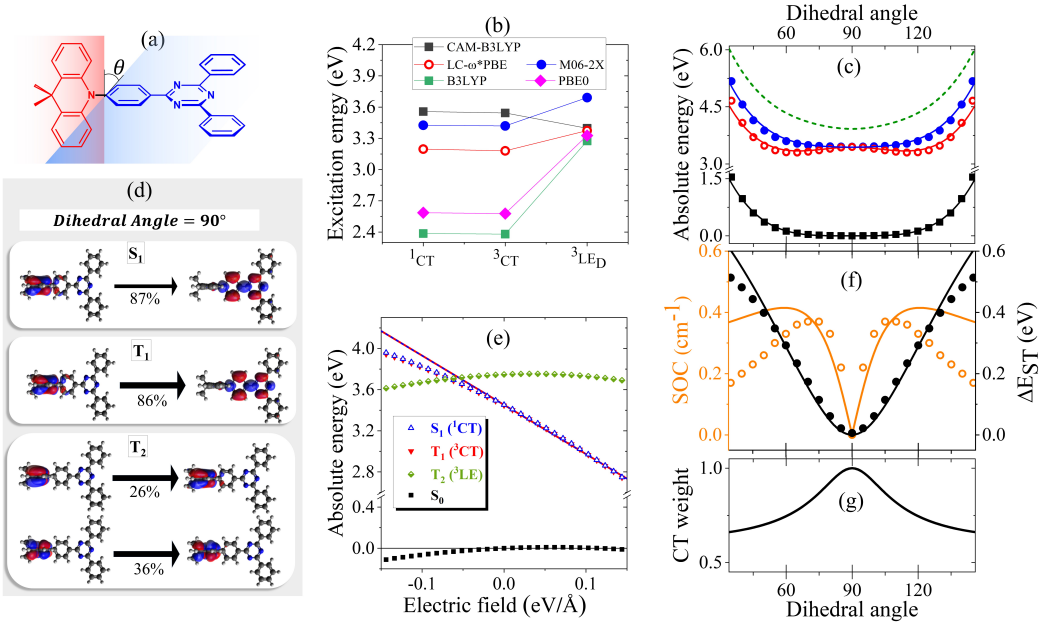

Figure 2.9: (a) a sketch of **DMAC-TRZ**, showing the dihedral angle, (b) Excitation energies for the three lowest excited states calculated at the equilibrium geometry with different functionals. (c) The energy of the ground (black), lowest excited singlet (blue) and triplet (red) states calculated as a function of θ in TD-DTF (symbols) and ESM (lines). The green dashed line shows the effective LE triplet introduced in the ESM. (d) Natural transition orbitals of the lowest singlet excited state and of the two- lowest triplet states. (e) Energies of the four lowest states vs the applied field (results for transition energies are shown in Figure 2.16) (f) The singlet-triplet gap (black) and the spin-orbit coupling (orange) between the lowest singlet and triplet states vs θ. Symbols and lines refer to TD-DFT and ESM results, respectively. (g) The weight of the CT state in the lowest triplet as estimated in ESM.

only be rationalized accounting for the coupling with some higher energy (local) excited triplet state. Figure 2.9f finally summarizes results of interest for TADF: the θ-dependence of the singlet-triplet gap and of the corresponding spin-orbit coupling. As expected, the singlet-triplet gap increases as the mutual orientation of the D and A planes deviates from orthogonality, at the same time the spin-orbit coupling first increases, to decrease again for $75° < \theta < 105°$.

The comparison with experiment requires a careful analysis of solvation effects, typically dealt with approximating the solvent as a continuum dielectric medium.[26] However, as discussed in Chapter 1, current implementations of continuum solvation models in quantum chemical packages do not properly account for the role of the solvent electronic polarizabil-

ity, leading to results that, as shown in Figure 2.10 for the available implementations of the polarizable continuum model in Gaussian 16,[56] wildly depend on the specific approximation scheme adopted, already in the comparatively simple case of a non-polar solvent. In the following Section we will therefore develop a minimal model for **DMAC-TRZ** that will allow us to discuss solvation and matrix effects in a simple and reliable approach.

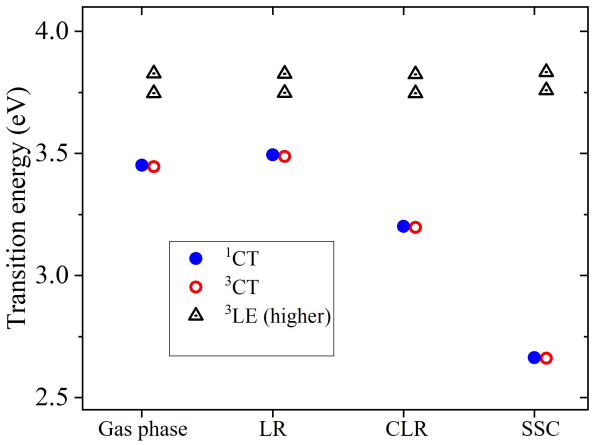

Figure 2.10: Excitation energies of the lowest singlet and three-lowest triplet states in gas phase and methylcyclohexane using different formalisms for solvent response: linear response (LR), corrected linear response (CLR) and state specific correction (SSC).[140–142]

2.4 Understanding TADF: Conformational Disorder and Matrix Effects

2.4.1 Setting up the Model

Having collected a large amount of experimental data and of computational results, we are now in the position to set up a model for **DMAC-TRZ**. In the spirit of essential state models (ESM)[133,134,143,144] we select the minimal set of electronic diabatic basis states to describe the ground and the low-energy excited states.

As for singlet states, the two-state model, proposed and extensively validated for D-A dyes,[133,134,145] also applies to **DMAC-TRZ**. The electronic basis states are selected as the neutral DA state, N, and the zwitterionic D^+A^- state, Z. The two states are separated by an energy difference $2z$ and are mixed by a matrix element $-\tau$, as sketched in Figure 2.17. As discussed above, the orthogonal configuration of the D and A planes, suggests a vanishing τ

at the equilibrium so that the ground state S_0 and the first excited state S_1 basically coincide with N and Z, respectively.

To account for the lowest triplet state, the basis must be extended to account for the zwitterionic triplet state T. The energy of the singlet and triplet zwitterionic basis states, Z and T, is the same, and, according to the El-Sayed rule, the spin-orbit coupling between the two states vanishes. A small but finite spin-orbit coupling V_{soc} instead mixes T with N.

2.4.1.1 θ Dependence of τ

We are interested to reproduce the θ dependence of the calculated energies of the excited singlet and triplet states in Figure 2.9c. To this aim, the spin orbit coupling V_{soc} can be treated as a minor perturation, so that, at the lowest order, only two electronic parameters enter the three state model: $2z$ whose marginal θ-dependence is neglected, and τ whose dependence on θ is definitely relevant. Information on the $\tau(\theta)$ dependence can be extracted mapping TD-DFT results on ESM. Specifically, in ESM the product between the transition frequency and the transition dipole moment is proportional to τ.[146]. Relevant TD-DFT results in Figure 2.11 are fully consistent with $\tau(\theta) = \tau_0|\cos(\theta)|$.

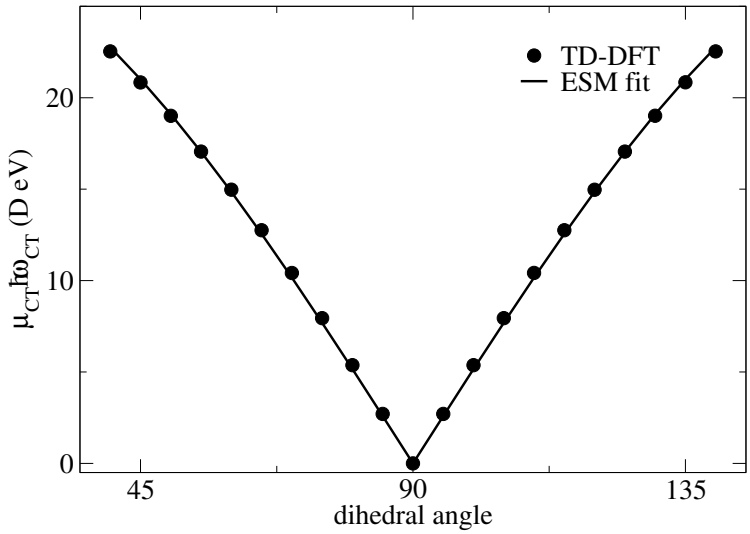

Figure 2.11: TD-DFT results for $\mu_{CT}\hbar\omega_{CT}$ (symbols) fitted with the function $A|\cos\theta|$ (line) with A as fitting parameter.

System properties in ESMs are dependent on the ionicity ρ that is defined by the model parameters as:

$$\rho = \frac{1}{2}\left(1 - \frac{z}{\sqrt{z^2+\tau^2}}\right) \tag{2.1}$$

In particular the transition dipole moment, μ_{CT} is given by:

$$\mu_{CT} = \mu_0 \sqrt{\rho(1-\rho)} \tag{2.2}$$

where μ_0 is the dipole moment associated to the zwitterionic state. The CT transition energy, $\hbar\omega_{CT}$

$$\hbar\omega_{CT} = \frac{\tau(\theta)}{\sqrt{\rho(1-\rho)}} \tag{2.3}$$

The product $\mu_{CT}\hbar\omega_{CT}$ has the same θ dependence as $\tau(\theta)$:

$$\mu_{CT}\hbar\omega_{CT} = \mu_0\tau(\theta) \tag{2.4}$$

The dependence of $\tau(\theta)$ is obtained fitting the values of $\mu_{CT}\hbar\omega_{CT}$ predicted using M06-2X/6-31G(d) calculations for different values of θ with the function $f(\theta) = A|\cos(\theta)|$ as in Figure 2.11.

2.4.1.2 Three-State vs Four-State Model for DMAC-TRZ

We must also introduce a restoring potential that we set equal for all states, in the hypothesis that state-specific features can be reproduced by the ESM, provided the relevant physics is properly accounted for. The restoring potential is set via an expansion to the fourth order around the equilibrium $V(\delta) = a_2\delta^2 + a_4\delta^4$, where $\delta = \theta - 90°$.

Initially, we employ a three state model and relevant 3×3 three-state Hamiltonian reads (basis: $|N\rangle$, $|Z\rangle$, $|T\rangle$):

$$\hat{H}_{3\times3} = \begin{pmatrix} 0 & -\tau_0|\sin\delta| & V_{soc} \\ -\tau_0|\sin\delta| & 2z & 0 \\ V_{soc} & 0 & 2z \end{pmatrix} + a_2\delta^2 + a_4\delta^4 \tag{2.5}$$

where all symbols are defined before.

Irrespective of model parameters, in the three-state model the triplet state only marginally mixes with the singlet state and therefore the relevant potential energy curve cannot develop the double minimum calculated in TD-DFT (Figure 2.12). A TD-DFT analysis of the nature of the lowest triplet state shows that it is a pure CT state at $\theta = 90°$, but it acquires some local nature when the system deviates from orthogonality. Unfortunately, several local triplet states enter into play and including all of them would lead to an impractical ESM, with too many parameters. On the other hand, we are not interested to model in detail higher excited triplets, rather we just want to capture the effect of their mixing with T_1.

We therefore set up a four-state model that, besides the three states, $|N\rangle$, $|Z\rangle$ and $|T\rangle$, described above, also includes an effective local triplet state $|L\rangle$ whose energy, $2k$ is a free fitting parameter. As for the mixing matrix element with T we assume the same angular

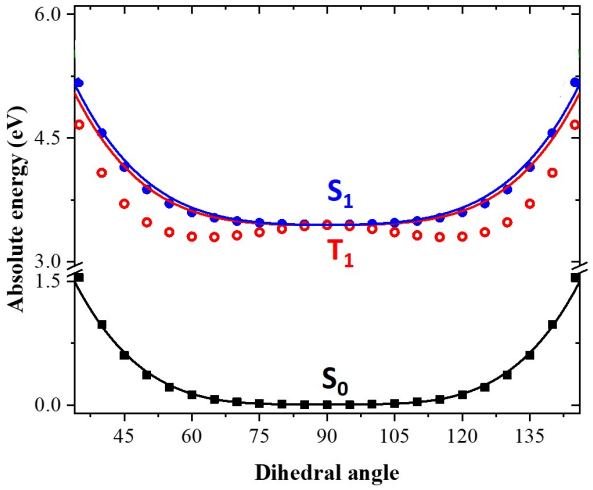

Figure 2.12: Energy of the ground and lowest excited singlet and triplet states calculated as a funcion of θ in TD-DFT (symbols) and three-state ESM (lines).

Table 2.3: ESM parameters extracted from the fit of the potential energy curves in Figure 2.9c

z (eV)	1.72
τ_0 (eV)	0.75
k (eV)	1.96
β_0 (eV)	0.85
a_2 (eV)	$6.00 \cdot 10^{-5}$
a_4 (eV)	$1.43 \cdot 10^{-7}$

dependence as for τ, setting $\beta(\theta) = \beta_0|\cos\theta|$. The relevant Hamiltonian, on the $|N\rangle$, $|Z\rangle$, $|T\rangle$ and $|L\rangle$ basis, reads:

$$\hat{H}_{4\times4} = \begin{pmatrix} 0 & -\tau_0|\sin\delta| & V_{soc} & 0 \\ -\tau_0|\sin\delta| & 2z & 0 & W_{soc} \\ V_{soc} & 0 & 2z & -\beta_0|\sin\delta| \\ 0 & W_{soc} & -\beta_0|\sin\delta| & 2k \end{pmatrix} + a_2\delta^2 + a_4\delta^4 \qquad (2.6)$$

The spin-orbit coupling elements, V_{soc} and W_{soc}, are very small and do not appreciably affect the calculated potential energy curves. To reproduce TD-DFT results model parameters are set to the values in Table 2.3. The agreement is very satisfactory (Figure 2.9c), suggesting that the proposed ESM properly captures the low-energy physics of the system. Quite interestingly, the lowest triplet state, the one relevant to TADF, has a pure CT character at 90°, but it acquires a partial local character at the equilibrium geometry (Figure 2.9g),

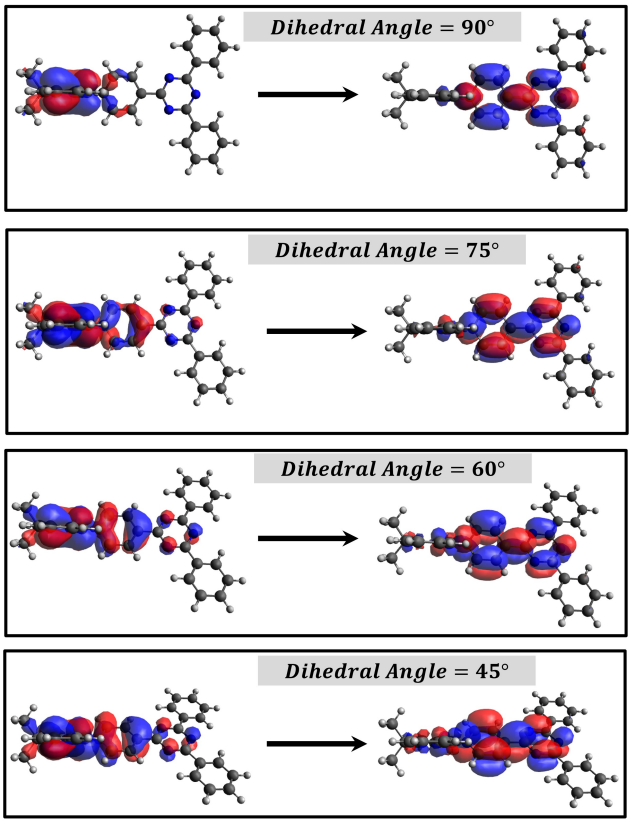

Figure 2.13: Natural transition orbitals calculated for T_1 state for different θ values.

as also confirmed by the analysis of the evolution with the dihedral angle of the natural transition orbitals calculated for T_1 state in Figure 2.13.

2.4.1.3 The Role of the Effective Local Triplet State

The choice of the effective local triplet (^{3}LE) state coupled to the CT triplet is somewhat arbitrary as it mimics the effects of several local triplet states. However, since we are interested in the properties of T_1, the lowest triplet, adopting different choices for the effective state has marginal effects on molecular and spectroscopic properties we are interested in. In Figure 2.14, we compare results obtained with models parameters in Table 2.4, with those obtained for different choices for the effective triplet state, and specifically we show results for a system where the state has a larger energy and a larger coupling strength and one where two coupled local triplet states are considered. The left panels in the Figure showing results for Model 1 coincide with data reported in the previous section (Figure 2.9). Middle panels refer to Model 2, where the energy and the coupling strength of the effective local triplet state are increased. Finally the rightmost column show results obtained for Model

3 that considers two coupled local triplets. Results are marginally affected by the choice: the θ-dependence of relevant electronic states and the SOC magnitude which are in fact governed by the nature of the lowest triplet state, and more precisely by the weight in this state of the CT triplets, while the precise properties of the effective triplet state(s) play a marginal role, as also demonstrated by calculated spectra in next section and Figure 2.15. We therefore reuse Model 1 for subsequent analysis.

	Model 1	Model 2	Model 3
z (eV)	1.72	1.72	1.72
τ_0 (eV)	0.75	0.75	0.75
k (eV)	1.96	2.20	1.96
β_0 (eV)	0.85	1.20	0.75
k' (eV)	-	-	2.20
β_0' (eV)	-	-	0.60
a_2 (eV)	$6.00{\cdot}10^{-5}$	$6.00{\cdot}10^{-5}$	$6.00{\cdot}10^{-5}$
a_4 (eV)	$1.43{\cdot}10^{-7}$	$1.43{\cdot}10^{-7}$	$1.43{\cdot}10^{-7}$
V_{soc} (cm^{-1})	3.10	3.10	3.10
W_{soc} (cm^{-1})	1.40	1.40	1.00
W'_{soc} (cm^{-1})	-	-	1.00

Table 2.4: Different parametrizations of the model prosposed. Model 1 is the same parametrization as in Table 2.3. Model 2 is a different parametrization, obtained for a different energy of $|L\rangle$. Model 3 accounts for an additional local state $|L'\rangle$ that is coupled through the following matrix elements: $\langle L'|\hat{H}|T\rangle = -\beta_0'|\sin(\delta)|$ and $\langle L'|\hat{H}|Z\rangle = W'_{soc}$.

Since at the equilibrium geometry the ground state S_0 and T_1 practically coincide with $|N\rangle$ and $|T\rangle$, respectively, we set $V_{soc} = 3.84 \cdot 10^{-4}$ eV equal to the TD-DFT value for the spin-orbit coupling between S_0 and T_1 states. Finally, the value of $W_{soc} = 1.74 \cdot 10^{-4}$ eV is adjusted in order to match the θ-dependence of the S_1-T_1 SOC (Figure 2.9f).

2.4.2 Validating the Model against Steady-State Spectra

Having built and parametrized against TD-DFT the electronic model for **DMAC-TRZ**, we now validate it against experimental spectra in Section 2.2. Towards this aim, the model must be extended to account for electron-vibration coupling and for solvation effects, as to address the observed vibronic structure and solvatochromism.

Typically, ESMs for D-A dyes describe electron-vibration coupling in terms of a single effective coordinate Q that accounts for the different geometry of the neutral and charge-separated diabatic states.[133,134,145]. For **DMAC-TRZ**, the frequency of the effective coor-

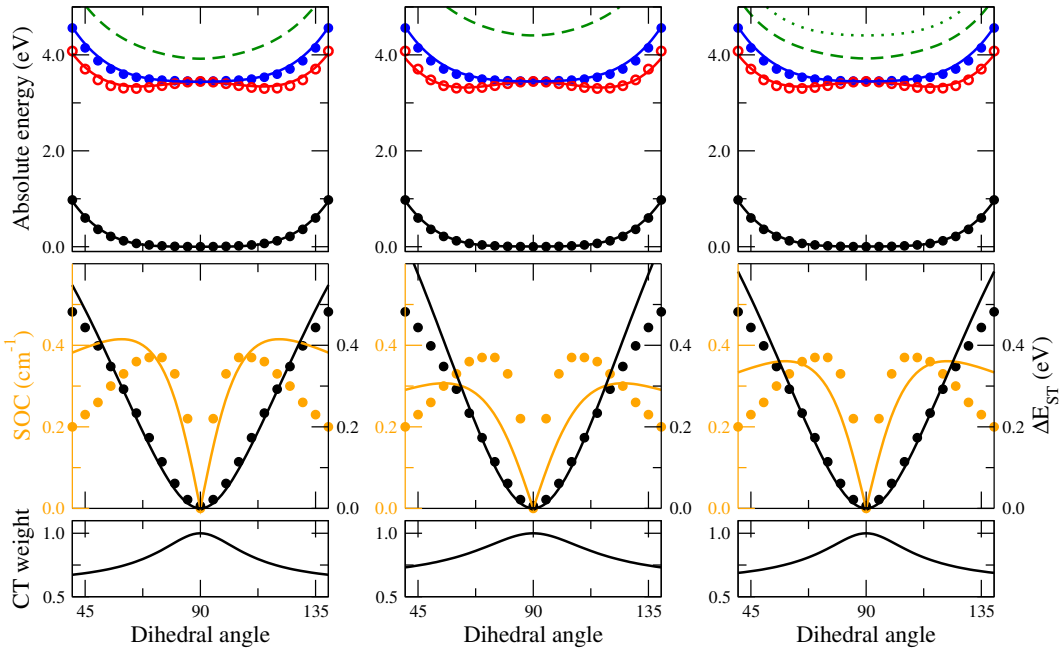

Figure 2.14: From top to bottom: PES, singlet-triplet energy gap and spin-orbit coupling and the weight of the CT triplet in T_1 state. Left: Model 1 parametrization (see Table 2.4); middle: model 2; right: model 3.

dinate is easily estimated as $\omega_v \sim 0.18$ eV from the partially resolved vibronic structure of optical spectra in non-polar solvents. The strength of the coupling is measured by the vibrational relaxation energy, ε_v, the energy gained by the charge separated (either Z or T) states upon relaxation. From DFT energies of the isolated D and D^+ and A and A^- species we extract $\varepsilon_v \sim 0.17$ eV.

Determination of ε_v: The vibrational relaxation energy, ε_v, is estimated through DFT energy calculations on the isolated donor (D) and acceptor (A) and the respective ionized species, D^+ and A^-:

$$\varepsilon_v = \left(E_{D^+}^{(D)} + E_{A^-}^{(A)}\right) - \left(E_{D^+}^{(D^+)} + E_{A^-}^{(A^-)}\right)$$

where $E_i^{(j)}$ is the energy of i in the equilibrium structure of j (See Table 2.5). Calculations involving the open-shell systems D^+ and A^- were done using unrestricted M06-2X/6-31G(d).

2.4.2.1 Modelling the Solvent Response

The simplest solvation model describes the solvent as a continuum elastic medium that responds to the presence of a solute molecule generating at the solute location an electric field, called the reaction field, proportional to the solute dipole moment. As extensively discussed

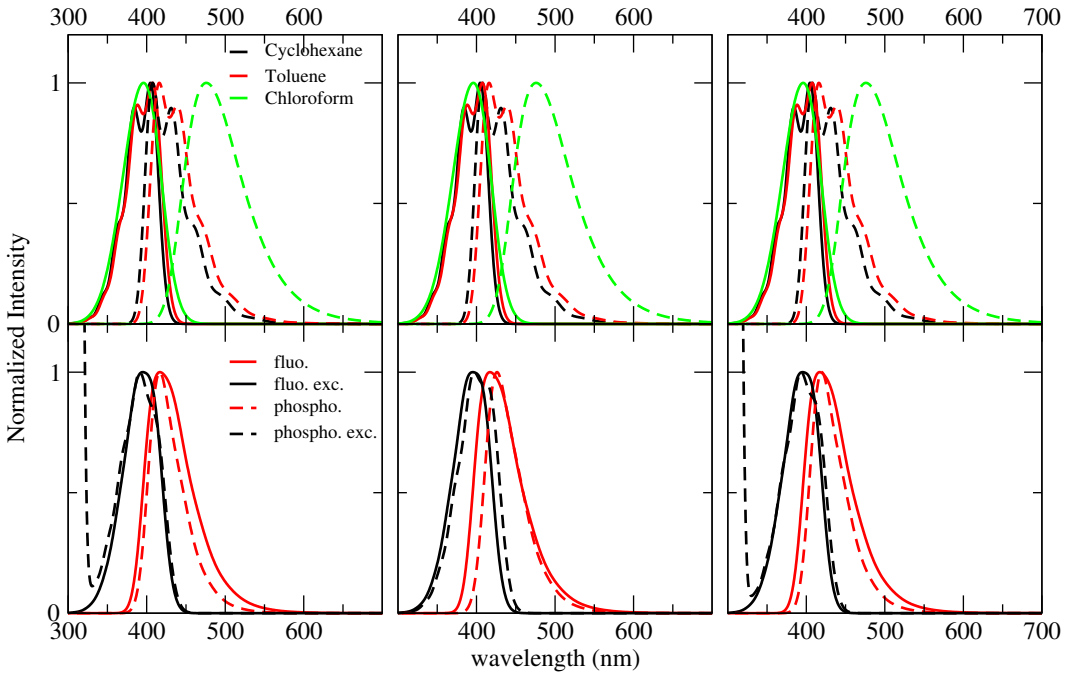

Figure 2.15: Top: Normalized absorption and fluorescence spectra (continuous and dashed lines, respectively) of **DMAC-TRZ** in different solvents. Bottom: emission and excitation spectra of **DMAC-TRZ** in glassy 2MeTHF. The columns show spectra calculated for model parameters listed in Table 2.4 (from left to right: model 1 to 3).

	SCF Energy (a.u.)
$E_{D^+}^{(D)}$	-634.873448021
$E_{D^+}^{(D^+)}$	-634.875775452
$E_{A^-}^{(A)}$	-973.174499157
$E_{A^-}^{(A^-)}$	-973.178453857

Table 2.5: SCF energies of D^+ and A^- used to estimate ε_v.

in Chapter 1, two components of the reaction field must be considered, a fast component associated to the electronic polarizability of the solvent and a slow component, of interest for polar solvents, associated with the orientational motion of the solvent molecules. The fast solvation component can be treated in the antiadiabatic approximation leading to a renormalization of the z parameter. In the hypothesis that the solute occupies a spherical cavity of radius a inside the solvent, the renormalized z reads:

$$z \to z - \frac{\mu_0^2}{16\pi\varepsilon_0 a^3}\frac{2\eta^2-1}{2\eta^2+1} \tag{2.7}$$

where ε_0 is the vacuum dielectric constant, η is the solvent refractive index at optical

frequencies, a is the cavity radius and μ_0 is the dipole moment associated with zwitterionic (Z and T) states. We set $a = 6.44$ Å as the suggested Onsager radius (0.5 Å larger than the radius corresponding to the computed molecular volume inside a contour of 0.001 electrons/Bohr^3 density).[56]

Estimation of μ_0: In order to estimate μ_0, we make resort to the dependence of the excited states with CT character (S_1 and T_1) on an applied external electric field, as shown in Figure 2.9e. More precisely, to get rid of the small F-dependence of the ground and local excited states, we estimate $\mu_0 \sim 22.71$ D from a linear fit of the S_1 and T_1 transition energies (Figure 2.16).

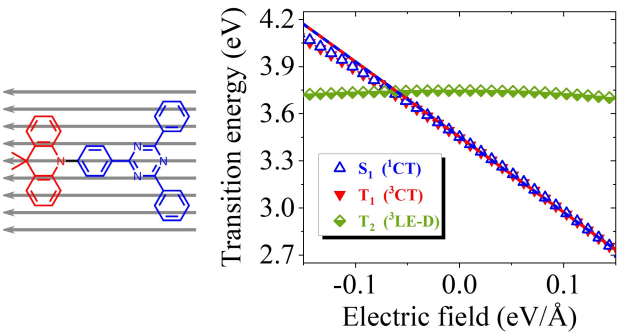

Figure 2.16: Left panel: a sketch of the molecule under an applied uniform electric field. Right panel: transition energies of the lowest singlet and triplet states as a function of an external electric field applied along the CT direction. Symbols refer to TD-DFT results, continuous lines show ESM energies for the CT states.

The slow component of the reaction field F_{or} enters the model as a slow coordinate and can be treated in the adiabatic approximation. The total Hamiltonian then reads

$$\hat{H}_{tot} = \hat{H} + \left[-\sqrt{\hbar\omega_v \varepsilon_v}\hat{Q}\left(|Z\rangle\langle Z| + |T\rangle\langle T|\right) + \frac{\hbar\omega_v}{4}\left(\hat{Q}^2 + \hat{P}^2\right)\right] + \\ + \left[-\mu_0 F_{or}\left(|Z\rangle\langle Z| + |T\rangle\langle T|\right) + \frac{1}{2r_{or}}F_{or}^2\right] \tag{2.8}$$

where $\hat{H}$ is the electronic Hamiltonian in Equation 2.6 with renormalized z as in Equation 2.7 to account for fast solvation. The first square bracket groups the vibrational terms, $\hat{P}$ being the momentum operator associated to the coordinate $\hat{Q}$. The second square bracket collects polar solvation terms, with r_{or} defined as

$$r_{or} = \frac{2}{4\pi\varepsilon_0 a^3}\left[\frac{\varepsilon_{st}-1}{2\varepsilon_{st}+1} - \frac{\eta^2-1}{2\eta^2+1}\right] \tag{2.9}$$

where ε_{st} is the static dielectric constant of the solvent. The values of η and ε_{st} of the solvents of interest are listed in Table 2.6. The above equation (Equation 2.9) is used to

estimate solvent relaxation energy which is defined as (energy unit):[44]

$$\varepsilon_{or} = \frac{1}{2} r_{or} \mu_0^2 \tag{2.10}$$

We solve the model Hamiltonian in Equation 2.8, writing the corresponding Hamiltonian matrix, for fixed F_{or} and δ values, on the basis obtained as the direct product of the 4-dimensional electronic basis states times the first M states of the harmonic oscillator associated to the vibrational coordinate $\hat{Q}$. M is large enough (typically in this work M=10) to ensure convergence. The Hamiltonian matrix is then diagonalized numerically to get vibronic eigenstates. Absorption and fluorescence spectra are computed assigning to each transition a Gaussian bandshape with a half-width at half-maximum of $\Gamma = 0.08$ eV. Spectra calculated for different F_{or} and δ values are then summed over accounting for their Boltzmann weight with reference to the energy of the ground state for absorption spectra, and of the lowest singlet and triplet states for fluorescence and phosphorescence spectra, respectively.[143]

Calculated absorption and fluorescence spectra in solvents of different polarity are shown in Figure 2.17a. The values of η and ε_{st} of the solvents of interest are listed in Table 2.6. The required dielectric parameters for the solvents are taken from the literature (except for 2MeTHF at 77K) and are listed in Table 2.6. Literature data for ε_{st} and ε_{opt} of glassy 2MeTHF at 77 K are not available. Since the refractive index of organic solvents increases linearly as the temperature decreases,[147], we set $\varepsilon_{opt}^{2\text{MeTHF}}(77K) = 2.016$. As for the static dielectric constant, the effective polarity of 2MeTHF increases as the temperature decreases and, for glassy 2MeTHF at 77K it is comparable to that of liquid EtOH or DMF,[148] so we set $\varepsilon_{st}^{2\text{MeTHF}}(77K) = 30.5$.

Solvent	ε_{opt}	ε_{st}
Cyclohexane	2.03	2.03
Toluene	2.24	2.38
Chloroform	2.09	4.81
2MeTHF	1.98	6.97

Table 2.6: Solvent dielectric properties at ambient conditions.

Absorption spectra agree well with experimental results in Figure 2.2 (see also Figure 2.18 for an easy comparison), showing negligible solvatochromism. Emission spectra qualitatively agree with experiment, reproducing the observed solvatochromism and the bandshape evolution with solvent polarity. The Stokes shift is overall underestimated with respect to experiment, possibly suggesting the presence of other sources of conformational disorder. We unerline that quantitative agreement (Figure 2.18) can be obtained if ε_{or} is

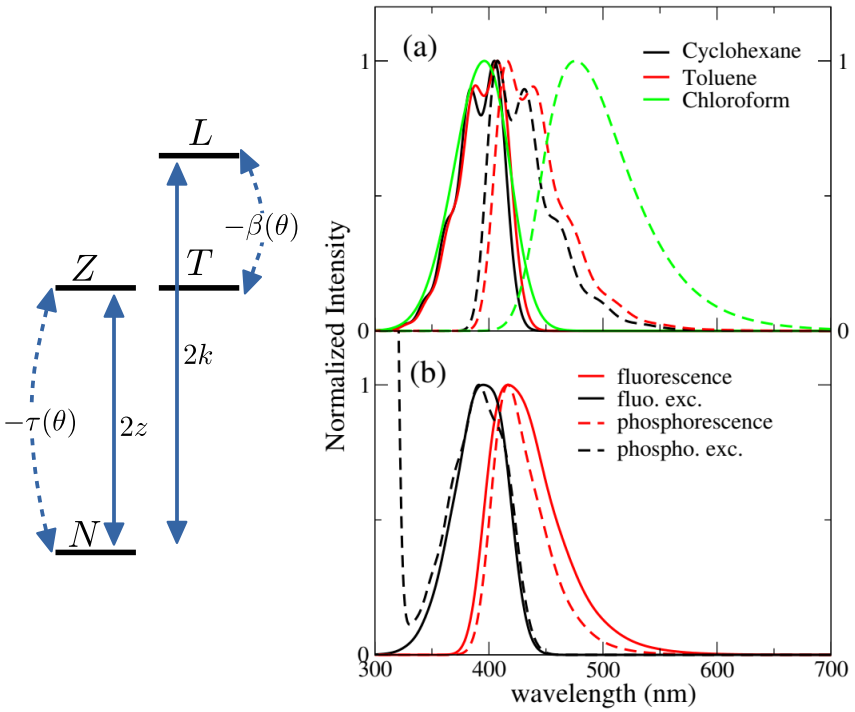

Figure 2.17: Left: schematic representation of the four electronic basis state entering the ESM model for **DMAC-TRZ**. Right panels: spectra calculated in the complete ESM also accounting for vibrational and conformational degrees of freedom and environmental effects. (a) absorption and fluorescence spectra (continuous and dashed lines, respectively) of **DMAC-TRZ** in solvents of different polarity at 298 K. (b) Calculated spectra in frozen 2MeTHF. Continuous lines: calculated fluorescence and fluorescence excitation spectra. Dashed lines: phosphorescence and phosphorescence excitation spectra. Excitation spectra are computed setting the excitation wavelength at 412 nm. The temperature was set to 77 K in the calculation of the Boltzmann distribution along the conformational coordinate, while it was set to 91 K (matching 2MeTHF glass transition temperature) for the Boltzmann distribution along the solvation coordinate.

treated as an adjustable parameter, accounting for all relaxation phenomena and relaxing the crude approximation of a spherical solvent cavity.

2.4.3 Matrix Effect

The model developed and validated for **DMAC-TRZ** in liquid solutions also applies to **DMAC-TRZ** in solid matrices, at least as long as the concentration is low enough to neglect intermolecular interactions. As a rule of thumb, concentrations $\sim$1% result, for typical matrix density $\sim$ 1 gr/cm^3, in an average distance between dyes of the order of few nm. Up

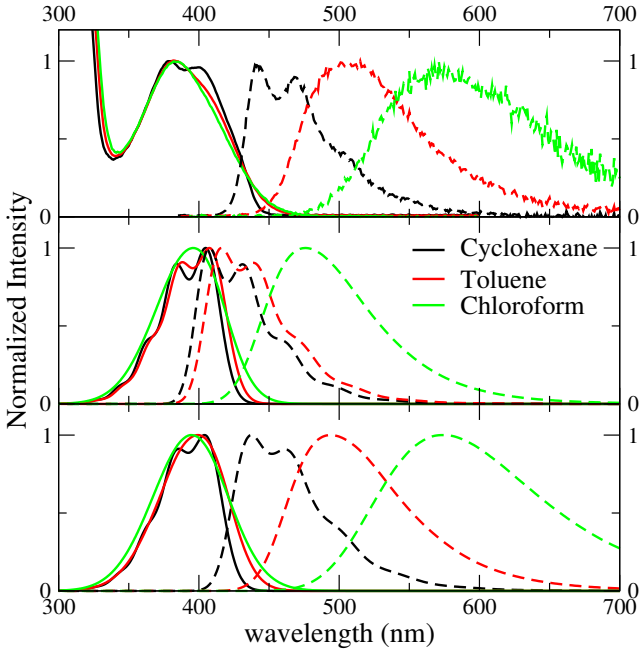

Figure 2.18: Normalized absorption and fluorescence spectra (continuous and dashed lines, respectively) of **DMAC-TRZ** in different solvents. Top panel: experimental data as in Figure 2.2. Middle panel: calculated spectra with ε_{or} estimated as described in Equation 2.10 (same data as in Figure 2.17a). Bottom panel: calculated spectra (298 K) adjusting ε_{or} as free fitting parameter: ε_{or} (Cyclohexane) = 0.10 eV; ε_{or} (Toluene) = 0.22 eV; ε_{or} (Cholorform) = 0.40 eV. The HWHM associated to each transition is $\Gamma = 0.03$ eV.

to these concentrations electrostatic intermolecular interactions can be safely neglected. In diluted solid matrices, the solvent molecules surrounding the solute do not readjust following the solute excitation, while the conformational flexibility of **DMAC-TRZ** is maintained. In this hypothesis, we calculate fluorescence and fluorescence excitation spectra of **DMAC-TRZ** in frozen 2MeTHF at 77 K as shown in Figure 2.17b. As discussed in the previous section for absorption and fluorescence in liquid solvents, also in this case the calculated Stokes shifts are somewhat underestimated, but a good agreement with experimental results in Figure 2.5 is obtained in terms of bandshape and band positions.

More delicate and interesting is the calculation of phosphorescence and phosphorescence excitation spectra. Phosphorescence is a forbidden process that occurs because spin-orbit coupling generates a very small mixing of singlet and triplet states. As a result, the triplet state *borrows* a tiny transition dipole moment from the singlet states. The lowest triplet state in **DMAC-TRZ** is described as the CT triplet plus a minor but non neglibible contribution from a local triplet state. Phosphorescence intensity then has a contribution from the (tiny) transition dipole moments associated with CT and LE triplets. Since the

transition dipole moments associated with CT states are orders of magnitude lower than the transition dipole moments associated with LE states, we assume that the contribution to phosphorescence from the LE state dominates over the contribution from the CT state. This hypothesis is also supported by the decrease of the emission anisotropy at very long delay times (Figure 2.5). Accordingly, phosphorescence and phosphorescence excitation spectra in Figure 2.17b are calculated only accounting for the LE contribution to the transition dipole moment (spectra calculated accounting only for the CT contribution in Figure 2.19 are in any case very similar). Calculated spectra in Figure 2.17b, referring to glassy 2MeTHF matrix at 77 K, compare very well with experimental results of Figure 2.2. Of course we only address phosphorescence bandshapes, the intensities of this process is very low and in any case it is not accessible experimentally.

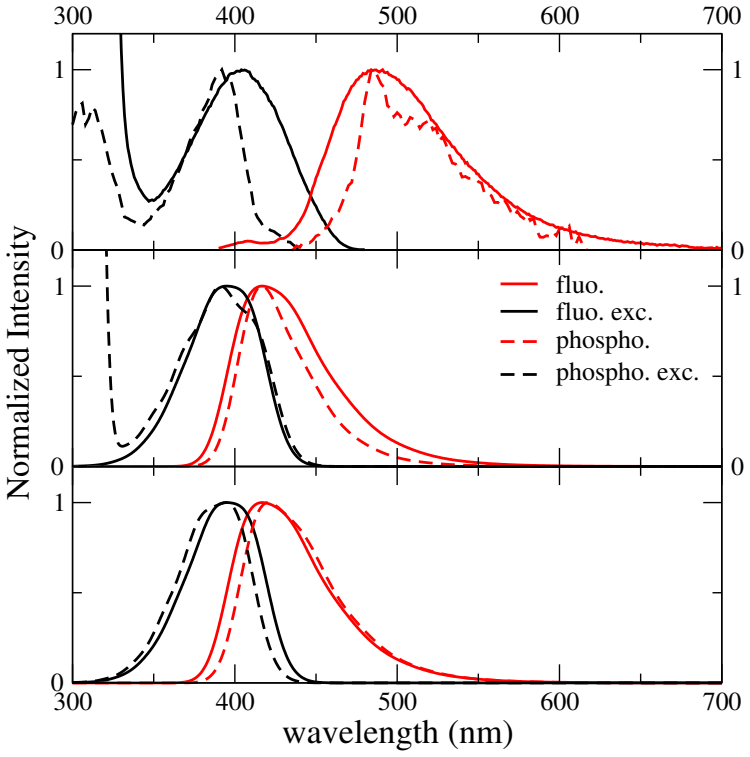

Figure 2.19: Emission and excitation spectra of **DMAC-TRZ** in frozen 2MeTHF. Top panel: experimental spectra as in Figure 2.2. Middle panel: calculated spectra as in Figure 2.17(b). Bottom panel: the same as in the middle panel, but with phosphorescence spectra calculated only accounting for the contribution from the CT state.

Low-T spectra are of special interest to collect reasonably intense phosphorescence spectra, The model of course applies to the calculation of finite temperature spectra as well. Indeed temperature enters in the definition of the Boltzmann distribution relevant to the ground state (for absorption and excitation spectra) or to the relevant excited state

for fluorescence and phosphorescence spectra. Increasing the temperature then leads to a broadining of the spectra, as shown in Figure 2.20 that shows room temperature spectra calculated for **DMAC-TRZ** dissolved in a matrix with the same dieletric properties adopted for glassy 2-MeTHF.

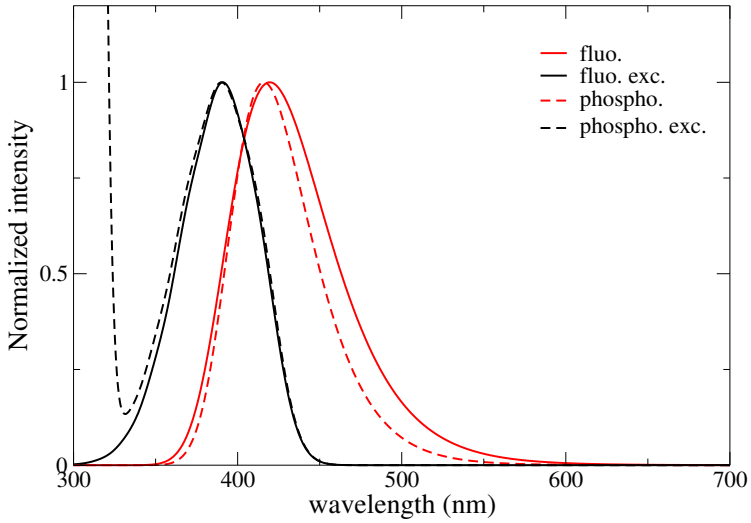

Figure 2.20: Calculated emission and excitation spectra of **DMAC-TRZ** in matrix with the same dielectric properties of 2-MeTHF at RT. Continuous lines: fluorescence and fluorescence excitation spectra. Dashed lines: phosphorescence and phosphorescence excitation spectra. Excitation spectra are computed setting the excitation wavelength as the wavelength of the maximum of the respective emission (fluroescence or phosphorescence) spectra.

The spectroscopic effects of polar solvation are well documented experimentally,[132] well understood in terms of simple solvation models[44,132,134,149] and are reliably addressed in current implementations of continuum solvation models in quantum chemical calculations.[26,31,32] The role of the electronic polarizability of the solvent (including rigid matrices) is more delicate. The marginal variability of the refractive index in common organic matrices makes an experimental analysis very difficult, while available implementations of continuum solvation models in quantum chemical approaches do not treat the corresponding solvation contribution properly.[35] However a sound understanding of the effects of the environmental polarizability on TADF-dyes is important in order to concurrently optimize the dye in its matrix, in the so called *smart matrix* approach. Specifically, the important information extracted from quantum chemical calculations for a dye in the gas phase cannot be transferred directly to a solvated dye, not even to a dye in a comparatively simple environment like a non-polar solvent. To illustrate this point we now disuss how the properties of **DMAC-TRZ** vary from gas-phase to a non-polar matrix with refractive index $\eta = 2$ (for

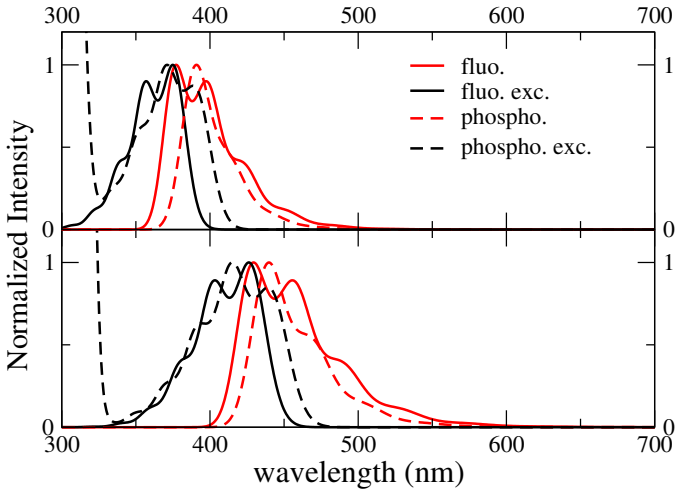

Figure 2.21: Calculated emission and excitation spectra of **DMAC-TRZ** in a $\eta = 1$ matrix (top) and in a $\eta = 2$ matrix (bottom) at 298 K. Continuous lines: fluorescence and fluorescence excitation spectra. Dashed lines: phosphorescence and phosphorescence excitation spectra. Excitation spectra are computed setting the excitation wavelength as the wavelength of the maximum of the respective emission (fluroescence or phosphorescence) spectra.

comparison the refractive index of common matrices is in the 1.5 - 1.7 range).

Specifically, Figure 2.22 shows the evolution with the dihedral angle, θ, of the energy of the first excited triplet and singlet and of the corresponding spin-orbit coupling. The first effect of the solvent polarizability is a considerable red-shift of CT states, that shows up with a marked red-shift of absorption and emission bands (see Figure 2.21). However, the most important effect of the environmental polarizability is expected on the properties that govern TADF. Indeed, since environmental effects are minor for LE states, the energy gap between CT and LE triplet increases, so that overall the spin-orbit coupling decreases, an effect that is clearly unfavorable for TADF applications. There is however another effect of the environmental polarizability: the potential energy curve associated to the lowest triplet is flatter in the matrix than in gas phase. Accordingly, a larger region is found where the singlet-triplet gap is thermally accessible (the shaded areas in the figure mark the inaccessible regions, those where the gap is larger than thermal energy at ambient conditions). Even more important, because of the shallower potential energy curve for the lowest triplet state, the distribution of θ equilibrated to the lowest triplet state is much broader in the matrix than in the gas phase. This is relevant, since TADF occurs from the equilibrated lowest

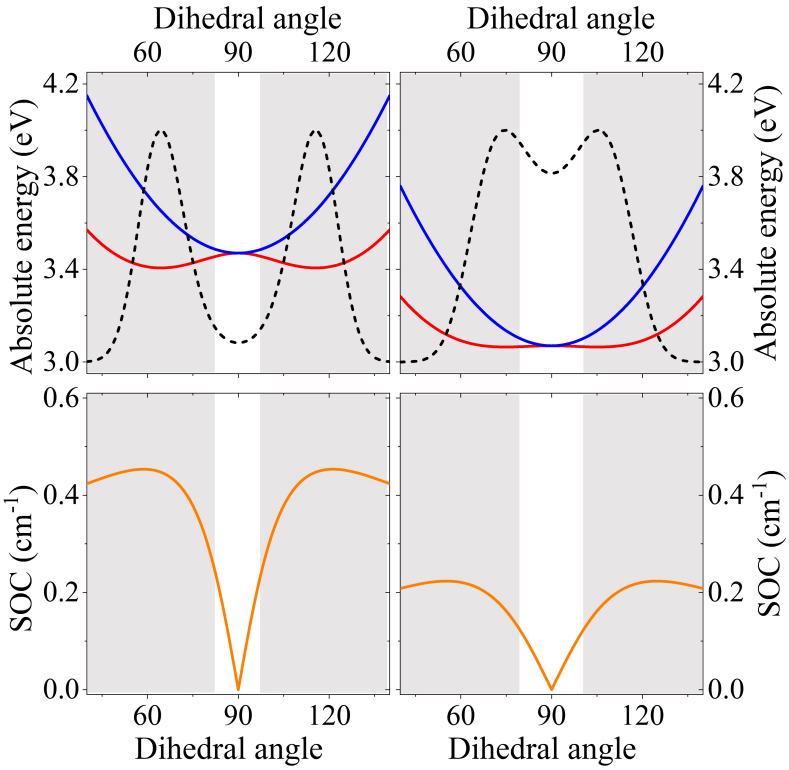

Figure 2.22: Comparison of ESM model results for **DMAC-TRZ** in the gas phase (left) and in a non-polar solvent with refractive index $\eta = 2$ (right). Top panels show the θ-dependence of the energies of the lowest excited singlet (blue) and triplet (red) states. The dotted line show the Boltzmann distribution calculated for the lowest triplet state. Bottom panels show the θ-dependence of the spin-orbit coupling between the lowest excited singlet and triplet states. The shaded areas mark the regions where the singlet triplet gap is larger than thermal energy at ambient conditions.

triplet state and in the gas-phase the population of conformations with thermally accessible RISC is marginal, while it becomes sizable in the matrix. This of course considerably favors TADF, possibly outweighting the decrease of the spin-orbit coupling among states responsible for RISC.

2.5 Conclusions

This chapter presents both experimental and theoretical analysis of **DMAC-TRZ**, a prototypical dye for TADF applications. Experimental results unambigously demonstrate that a state with predominant CT nature is responsible for fluorescence and delayed fluorescence.

Phosphorescence occurs in the same spectral region as fluorescence, from a triplet state with dominant CT character. Extensive gas-phase TD-DFT calculations, run in the presence of an applied electric field and for different conformations, confirm the experimental analysis and are exploited to build a reliable essential-state model for **DMAC-TRZ**. The model accounts for few electronic states, as needed to describe the low-energy properties of the dye, for the coupling to a molecular vibration, responsible for the vibronic structure of the absorption and fluorescence bands, and for the conformational degrees of freedom associated with the torsional angle that modulates spin-orbit coupling. Environmental effects are properly addressed to simulate spectral properties in liquid solution and solid matrices, accounting for the different role of polar solvation and of the electronic polarizability of the environment. The resulting picture, extensively validated against experiment, offers a sturdy and flexible toy model to investigate TADF.

The approach proposed here for a specific dye is general and can be applied to set up reliable few-state models for other dyes, including multipolar dyes, with multiple D and A groups. The enormous variability of the properties of these dyes, depending on the number and strength of the D and A groups, on bridging units and geometry,[12] calls for the definition of practical models to define reliable structure-properties relationships for the large and technologically relevant family of TADF dyes. The power of few-state models is in the possibility to account for a large number of interactions that range from vibrational coupling, to be treated in a truly non-adiabatic approach, conformational motion, treated adiabatically, and the interaction with the local environment, accounting for both the polarizability and the polarity of the environment. The model also sets the basis to build an open-quantum model[150,151] for TADF dyes able to address ISC and RISC processes, together with other competitive relaxation process without introducing additional approximations. The evolution of the population of excited states can be followed over several orders of magnitude in time, to trace the subtle competition between fluorescence, phosphorescence, non-radiative relaxation, ISC, RISC that govern the delicate TADF phenomenon shedding clear light on and their interdependence with vibrational and conformational motion and on environmental effects.

Chapter 3

Large Dihedral Angle Relaxation of DMAC-py-TRZ

3.1 Introduction

Commonly employed D and A fragments are 9,9-dimethyl-9,10-dihydroacridine (**DMAC**) and 2,4,6-triphenyl-1,3,5-triazine (**TRZ**), and the simplest combination of the two is found in DMAC-TRZ from Tsai *et. al.*[131] **DMAC-TRZ** shows excellent properties, with photoluminescence yield $\Phi_{PL} \sim 90\%$ in mCPCN films, and OLED with external quantum efficiency $EQE \sim 26.5\%$ at 500 nm. In devices based on pure DMAC-TRZ matrices, EQE up to 20.0% were measured. The very low quenching at high concentration can be attributed to the conformation of the material, the dihedral angle between the DMAC and TRZ fragment is almost 90°, making for a very non-planar molecule, effectively suppressing $\pi - \pi$ aggregation. In Chapter 2, we present a detailed theoretical and experimental characterization and different affecting parameters that govern TADF properties.

Modification of **DMAC-TRZ** with adamantane has been published by Li et. al. and Wada et. al. with the emitters **a-DMAC-TRZ**[152] and MA-TA[153] respectively. Even if the two reports functionalize the donor and the acceptor with the adamantane, the effect is that of reducing the conjugation of the material, leading to a bluer emission. The substitution of the two methyl groups with the adamantane in a-**DMAC-TRZ** also makes for a more rigid and bulky structure, suppressing excited state geometry deformation, leading to higher performances. The photoluminescent and electroluminescent performances remain similar to **DMAC-TRZ** ones, with Φ_{PL} of 86% and an EQEmax of 28.9%, the main difference is the blue-shift in the emission color, at 488 nm. The insertion of the adamantane unit on the triazine made for a larger improvement in the Φ_{PL}, bringing it almost to unity, at 99%, while the device, solution-processed in this case, presented a lower EQEmax at 22.1%, with also a blue-shifted λ_{EL} of 475 nm. Also from Wada et. al. came the material **DMAC-bPmT**.[154]

While the adamantane modification was aimed to tune the emission color, in this work they presented a design concept to enhance the k_{RISC} and thus the efficiency of **DMAC-TRZ** by using two pyrimidine instead of phenyls on the triazine. **DMAC-bPmT** presents a k_{RISC} of $8.8 \times 10^5 s^{-1}$, three times faster than **DMAC-TRZ**, at $2.9 \times 10^5 s^{-1}$, even though the addition of the pyrimidine led to a lower Φ_{PL} of 70% (vs 90% for **DMAC-TRZ**).[154]

Dual-conformation TADF emitters have also been documented by Shi *et. al.* with the emitters **TP2P-PXZ** and **TP5P-PXZ**.[155] The presence of quasi-equatorial (QE) and quasi-axial (QA) conformation for **TP2P-PXZ** led to a unique self-doped system, where the QA conformation effectively acts as the host material. This led to a highly efficient OLED for **TP2P-PXZ**, with EQEmax od 25.4% at λ_{EL} of 548 nm. **TP5P-PXZ** also presented decent device efficiency, at 14.6% of EQEmax at a slightly red-shifted λ_{EL} of 560 nm. Both materials also present extremely low-efficiency roll-off, with EQE1000 values of 16.5% and 8.0% for **TP2P-PXZ** and **TP5P-PXZ** respectively, with TP2P-PXZ representing the current state-of-the-art performance for non-doped devices.[155]

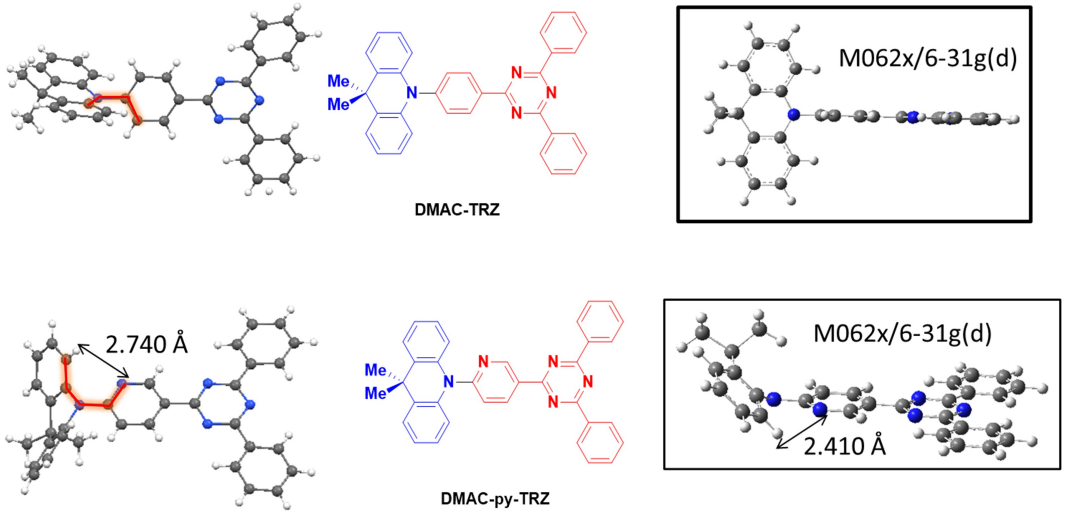

Figure 3.1: Crystal structure and molecular structure of **DMAC-TRZ** and **DMAC-py-TRZ**, respectively. The relevant

The role of steric hindrance was investigated by Chen *et. al.* in the two phenoxazine based-emitters **PXZ-PPO** and **PXZ-BOO**.[156] The large steric hindrance between nearby hydrogens, in PXZ-BOO, results in a twisted structure. **PXZ-BOO** shows TADF, leading to efficient devices (EQE 19.4% at 528 nm). In **PXZ-PPO** the steric hindrance is relieved and nearby H and N atoms allow for different structures. The dye shows indeed two different conformations, a quasi-planar structure with a twisted structure. The planar conformation shows a deep-blue emission but no TADF, while the twisted structure shows a green delayed emission. The planar conformation is dominant in the crystalline state, however, in solution

TADF is observed from the twisted conformation, despite its low population. The **PXZ-PPO** device has a slightly worst performance than **PXZ-BOO**, with EQEmax = 14.1% at the same $\lambda_{EL} = 528nm$.[156]

Dual-conformation TADF emitters have also been documented by Shi *et. al.* with the emitters **TP2P-PXZ** and **TP5P-PXZ**.[155] Phenoxazine and a central pyridine bridge were chosen to promote the formation of intra-molecular hydrogen bond in **TP2P-PXZ**, while **TP5P-PXZ** is presented as the control compound, with a conventional twisted conformation. The presence of quasi-equatorial (QE) and quasi-axial (QA) conformers of **TP2P-PXZ** led to a unique self-doped system, where the QA conformation effectively acts as the host material. This led to a highly efficient OLED for **TP2P-PXZ**, with EQEmax = 25.4% at λ_{EL}=548nm. **TP5P-PXZ** also shows decent device efficiency, at 14.6% = EQEmax at λ_{EL} = 560 nm. Both materials have extremely low efficiency roll-off, with EQE1000 values of 16.5% and 8.0% for **TP2P-PXZ** and **TP5P-PXZ** respectively, with **TP2P-PXZ** representing the current state-of-the-art performance for non-doped devices.[155]

In this chapter, we present a new TADF emitter **DMAC-py-TRZ**, which comes from a modification of the previously known, and discussed previously, emitter **DMAC-TRZ**. Besides presenting a good solution and solid-state photophysical properties, the interest in this material was sparked by the unusual crystal structure that was found. Instead of presenting the usual $\sim 90^\circ$ dihedral angle, the x-ray showed a very small twist of $\sim 19.73^\circ$ and a v-shaped bent molecule, with an angle of around $\sim 19.73^\circ$. The interesting molecular geometry led us to carry out an in-depth computational study of the dihedral angle relaxation and excited-state properties, together with a complete optoelectronic and photophysical characterization. For the sake of clarity, we will refer to the one that presents the $\sim 90^\circ$ dihedral angle as the orthogonal conformer, and to v-bent molecules, with a dihedral angle of $\sim 19.73^\circ$ as the bent conformer. Experimental data are collected by experimentalists in the host lab and with close collaboration with Prof Eli Zysman-Colman's lab, University of St Andrews, Scotland under TADF*life* network. Here I present experimental data to have a better understanding of the process. I then performed a critical analysis of TD-DFT analysis and combined them.

3.2 Computational Analysis

The ground state geometry of **DMAC-TRZ** and **DMAC-py-TRZ** was optimized in Gaussian 16 B.10,[56] followed by excited state TD-DFT calculation (Tamm-Dancoff approximation)[67,74] using M062X functional[72] and the 6-31g(d) basis set. In the following, we will dub "orthogonal" for the structure with a dihedral angle similar to 90° and "bent" for the structure with a small dihedral angle and V-shaped geometry.

In Chapter 2, I discussed an extensive computational analysis of **DMAC-TRZ**, set the basis for a few-state model that allowed us to discuss how the molecular geometry in the ground and excited states affects the energy gap, spin-orbit coupling, transition dipole moments, etc. More recently the same model was exploited to calculate ISC and RISC rates, also accounting for environmental effects.[157] In line with the crystal structure DFT calculation predicts an orthogonal geometry for the ground state. The optimized S_1 (^1CT) and T_2 (^3LE) states retain an orthogonal geometry, while the optimized T_1 state undergoes a large deformation ending up with a dihedral $\sim 30°$. At this small angle ΔE_{ST} increases, but, at the same time, SOC increases, allowing for efficient ISC/RISC. A rigid scan of the dihedral angle (Figure 3.2) is also informative. Specifically, starting with the optimized ground state geometry, we calculated the ground and excited state energy, upon gradual rotation of the D and A units without allowing for any additional molecular relaxation. The resulting S_0, S_1, T_2 and T_3 potential energy surface (PES) show a flat minimum for the orthogonal geometry, while T_1 gives a double minimum around $(90 \pm 30)°$ angle due to its mixing with higher excited triplet states.

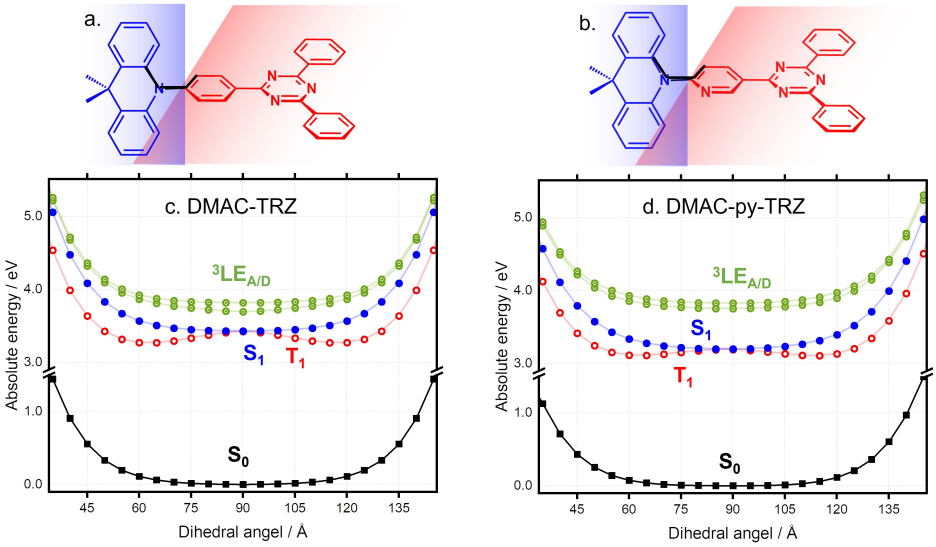

Figure 3.2: Sketch of (a) **DMAC-TRZ** and (b) **DMAC-py-TRZ** showing four adjacent atoms to define the dihedral angle of the dihedral rigid scan of interest. Energies of ground (black), lowest energy singlet (blue), lowest energy triplet (red) and two higher energy triplet (green) states.

For a direct comparison with DMAC-TRZ, we started our analysis by optimizing DMAC-py-TRZ in an orthogonal structure. A rigid dihedral angle scan analysis of the twisted DMAC-py-TRZ gives qualitatively similar PES as for DMAC-TRZ, with a single minimum for S_0, S_1 (^1CT), T_2 and T_3 (^3LE) at 90° and a double minimum for T_1 (^3CT)

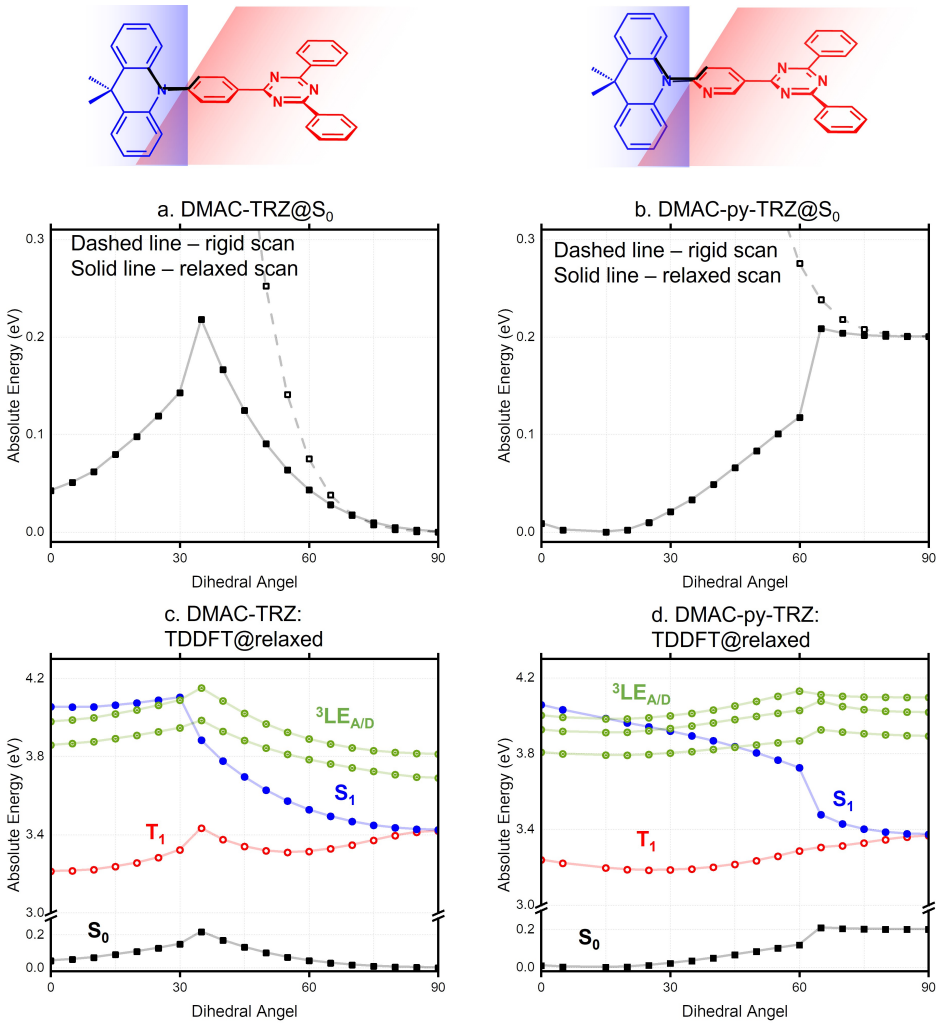

Figure 3.3: (Upper Panel) Sketch of **DMAC-TRZ** and **DMAC-py-TRZ** showing four adjacent atoms fixed during relaxed dihedral angle scan. (Middle Panel) Relaxed dihedral angle scan of (a) **DMAC-TRZ** and (b) **DMAC-py-TRZ** for S_0. (Lower Panel) Excited state energies of (c) **DMAC-TRZ** and (d) **DMAC-py-TRZ** relaxed energy suraface.

around $(90 \pm 30)^\circ$ angle (NTOs are shown in Figure 3.7). The nitrogen on the pyridine bridge increases the withdrawing strength of the A group with a decreased HOMO-LUMO gap in DMAC-py-TRZ ($E_{HOMO-LUMO} = 4.78eV$) orthogonal structure) vs DMAC-TRZ ($E_{HOMO-LUMO} = 4.99eV$). Accordingly, S_1 and T_1 excitations occur at lower energy in DMAC-py-TRZ than in DMAC-TRZ (Figure 3.4). The rigid scan results show a very steep increase in the energy of the molecule when decreasing the dihedral angle, suggesting a strong sterical hindrance. Therefore we undertook for both DMAC-TRZ and DMAC-py-TRZ a relaxed scan analysis for the dihedral angle. To carry out the relaxed energy scan we

took the previous rigid scan geometries and marked four adjacent atoms to define the dihedral angle of interest (Figure 3.2a and 3.2b). This angle is then frozen, while the molecule is otherwise allowed to relax towards the ground state equilibrium structure (Figure 3.3a and 3.3b).

The relaxed scan shows for both dyes two minima, corresponding to the orthogonal and bent structures. However in DMAC-TRZ, the orthogonal structure is lower in energy and the energy barrier from the orthogonal to the bent conformation amounts to 0.22 eV, making interconversion unlikely. In DMAC-TRZ the orthogonal geometry is therefore mostly populated at room temperature, fully in line with crystallographic data. In DMAC-py-TRZ, the bent conformation (dihedral angle $\sim 10°$) has lower energy than the orthogonal structure. Again, the energy barrier between the two conformations ($\sim 0.20eV$) is too large to allow for interconversion between the bent and orthogonal structures. In line with crystallographic results, the bent geometry is the stable ground state geometry for DMAC-py-TRZ.

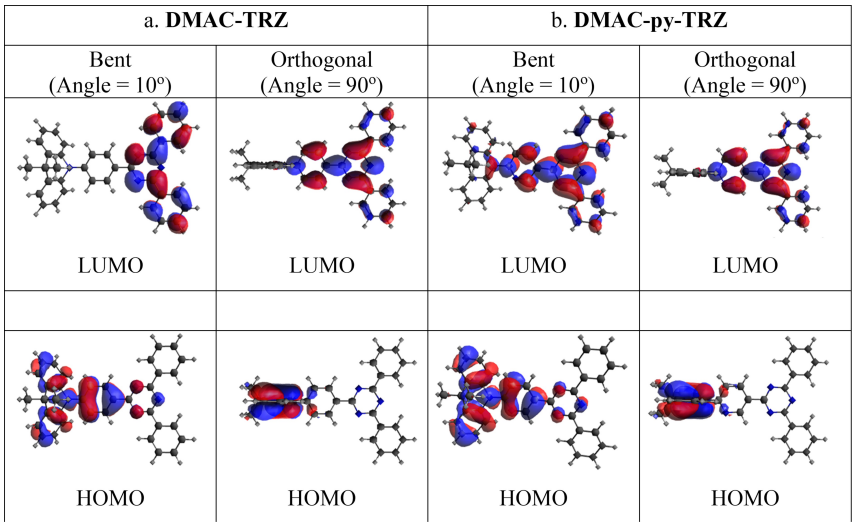

Figure 3.4: Molecular orbitals (HOMO and LUMO) of (a) DMAC-TRZ and (b) DMAC-py-TRZ for both bent and orthogonal geometries.

Very interesting results are obtained for the excited state energies at the geometries relevant to the rigid/relaxed scans of the dihedral angle(Figure 3.3c and 3.3d). In DMAC-TRZ both the rigid and the relaxed scan calculation lead to the same results: S_1 state is stable in the orthogonal structure, while T_1 state is stabilized in a twisted structure (dihedral angle $\sim 30°$). Full optimisation of S_1 and T_1 confirms this result. The scenario is much more interesting for DMAC-py-TRZ. The relaxed scan suggests the bent structure as for the stable ground state geometry. In these conditions, the vertical excitation energy to S_1 amounts to 4.1 eV and the singlet-triplet gap $\sim 0.78eV$ is by far too large for TADF. However, it is clear that the bent geometry is not the equilibrium geometry for S_1 (blue line in Fig. 3.3d):

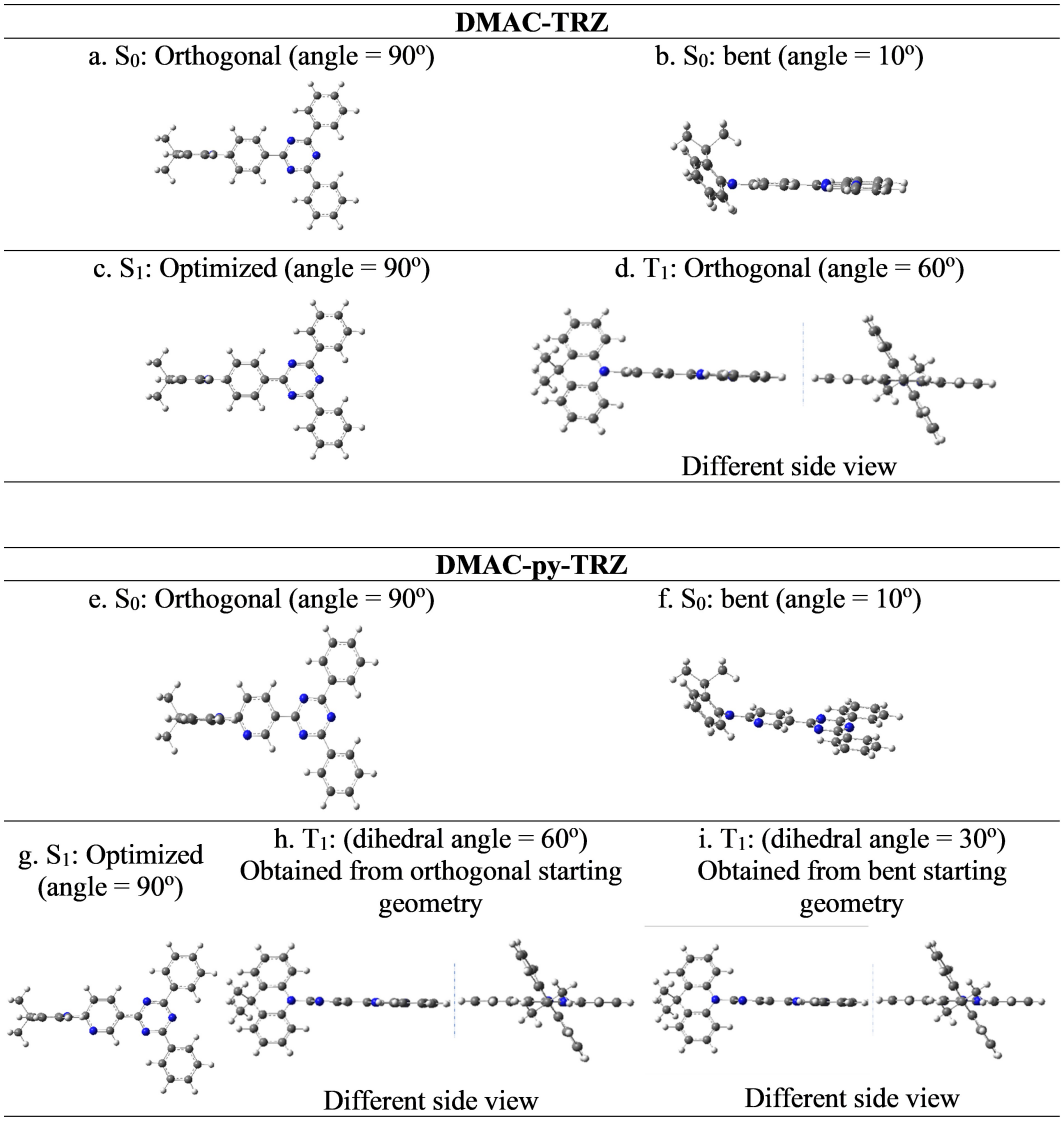

Figure 3.5: Optimized geometries (bent and orthogonal) of the ground state (S_0), first singlet excited state (S_1), first triplet-excited state (T_1) for both DMAC-TRZ and DMAC-py-TRZ. All geometries are obtained at the M06-2X/6-31g(d) level of theory.

indeed we do predict a huge structural deformation of the excited molecule from the bent to the orthogonal structure. In other terms, we do expect that fluorescence will occur from the orthogonal structure at a much lower energy ($\sim 3.17eV$) than calculated for the bent structure. Quite interestingly, in this orthogonal geometry, the singlet-triplet gap closes ($\sim 8.2meV$), making TADF possible.

T_1 state is predicted for DMAC-py-TRZ in a twisted geometry in either the rigid (Figure

3.2d, red line) and relaxed scans (Figure 3.3d, red line). The full optimization of the excited state geometry however yields conflicting results. For S_1 the situation is clear: taking either the bent or the orthogonal geometry as starting points for the excited state optimization, S_1 (Figure 3.5) always reaches the orthogonal conformation, supporting the results from the relaxed scan analysis. For T_1, instead, two different geometries are reached (Figure 3.5, middle ($\Delta E_{ST} = 0.93eV$) and right panel ($\Delta E_{ST} = 0.41eV$)) with comparable energies , so that it is not possible to reach a firm conclusion about the equilibrium geometry for T_1. NTOs calculated at the optimized S_1 geometry, and at the two possible geometries for T_1 are shown in Figure 5.

3.3 Experimental Details

3.3.1 Cyclic Voltammetry

Cyclic Voltammetry (CV) and Differential Pulse Voltammetry (DPV) of DMAC-py-TRZ, and of DMAC-TRZ as a comparison, were measured in degassed DCM with $tetra-n-butylammoniumhexafluorophosphate$ as the electrolyte and Fc/Fc^{+} as the internal reference, data are reported versus a Saturated Calomel Electrode (SCE) (Figure 3.6a). Both materials present reversible reduction and oxidation waves, with nearly identical profiles, which is expected, as the D and A moieties are basically the same in the two compounds. The effect of the pyridyl bridge can be observed in the higher oxidation potential of the pyridine material, with 0.97 V (for DMAC-TRZ) vs 1.11 V for DMAC-py-TRZ. The same behavior is observed for the reduction potential, also shifted up-fields, with values of -1.72 V and -1.64 V for DMAC-TRZ and DMAC-py-TRZ respectively. The calculated HOMO and LUMO values are -5.31 eV/ -2.62 eV and -5.45 eV/ -2.70 eV for DMAC-TRZ and DMAC-py-TRZ, respectively. The electron-withdrawing nature of the nitrogen lowers the electron density on the donor, leading to a weaker donor and a lower HOMO in DMAC-py-TRZ. The electron-withdrawing character also lowers the electron density on the acceptor, resulting in a lower LUMO level, meaning a stronger acceptor.

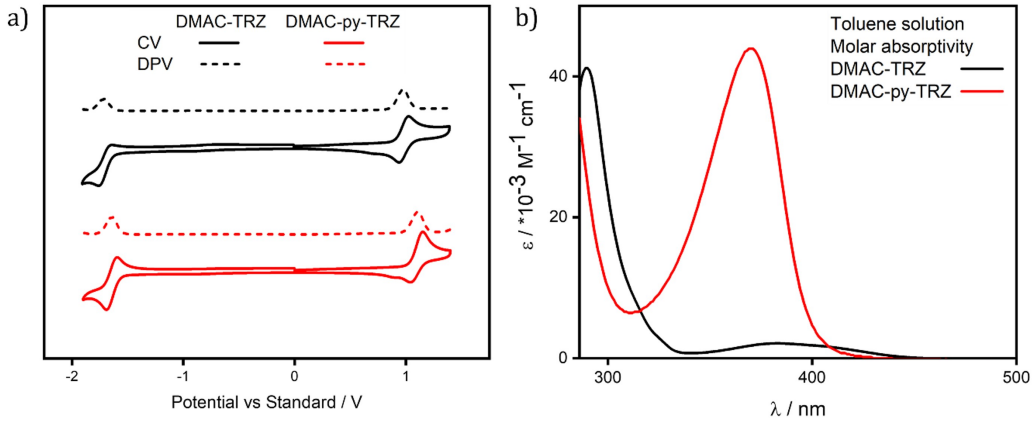

Figure 3.6: (a) Cyclic voltammetry (CV) and differential pulse voltammetry (DPV) of **DMAC-TRZ** (black) and **DMAC-py-TRZ** (red) in DCM (scan rate = 100 mV/s). (b) UV-vis absorption spectrum of **DMAC-TRZ** (black) and **DMAC-py-TRZ** (red) in 10^{-5} M toluene solution.

3.3.2 Optical Spectra

3.3.2.1 Absorption Oscillator Strength

As for UV-vis absorption, we focus on the lowest band, whose maximum is located at 382 nm and 370 nm in toluene in DMAC-TRZ and DMAC-py-TRZ, respectively. The slight blue shift of the absorption band in DMAC-py-TRZ is ascribed to the more efficient HOMO-LUMO mixing in the bent structure if compared with the marginal mixing in the orthogonal structure of DMAC-TRZ. Since the bent geometry has higher mixing between

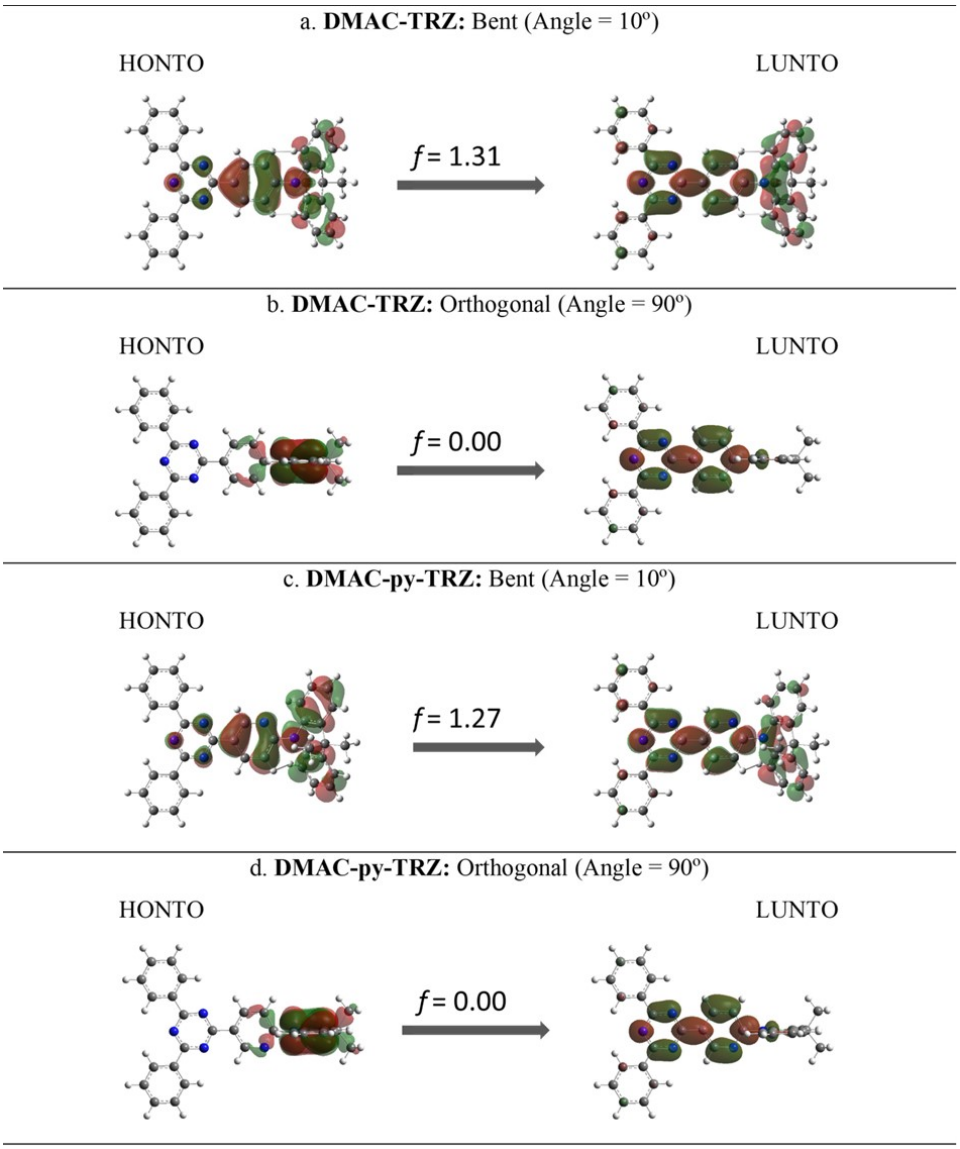

Figure 3.7: Natural transition orbitals of DMAC-TRZ for both (a) bent (b) orthogonal geometries and DMAC-py-TRZ for both (c) bent (d) orthogonal geometries shown.

HOMO-LUMO, energy gaps between the ground state and excited state increase. This causes the blue shift in absorption spectra for DMAC-py-TRZ. The different structure and hence mixing of orbitals in the two systems is however most dramatically demonstrated by the massively different intensity of the transition in the two systems. As shown in Figure 3.6b, the extinction coefficient of DMAC-py-TRZ is 20 times larger than for DMAC-TRZ, in line with the hypothesis of a much stronger conjugation in DMAC-py-TRZ than in DMAC-TRZ.

3.3.2.2 Effect of Solvent Polarity

The effect of solvent polarities on the absorption and emission spectra of the material is investigated for both **DMAC-TRZ** and **DMAC-py-TRZ**. Figure 3.8 shows room temperature absorption and emission spectra of **DMAC-py-TRZ** solutions in solvents of increasing polarity (cyclohexane, toluene, chloroform and DMSO). Relevant spectroscopic quantities are collected in Table 3.1. In-room temperature (Figure 3.8a and 3.8b), absorption is not solvatochromic, suggesting a small permanent dipole moment of the molecule in the ground state. Emission spectra instead show a large solvatochromism, suggesting that the emissive state has a large permanent dipole moment for both molecules.[134,158,159] In case of **DMAC-py-TRZ**, absorption is more blue-shifted, suggesting a higher S_1 states than **DMAC-TRZ**'s S_1 state. Recollecting the excited energy of **DMAC-py-TRZ**, an orthogonal geometry should give red-shifted and bent geometry should give blue-shifted absorption energy. This clearly suggests the existence of bent geometry of **DMAC-py-TRZ** in the ground state. The most interesting result is the very large Stokes shift (0.72 eV) observed in the non-polar cyclohexane solvent. This can only be explained in terms of a large rearrangement of the molecular geometry following photoexcitation.

To collect more information about the emissive state for **DMAC-py-TRZ**, we collected the spectra in the viscous polyTHF solvent at room temperature. Spectra are shown in Figure Figure 3.10. Even if a very weak emission is observed from the solvent, a double emission from the solute is detected. The emission at 410 nm is similar to the one observed in the glassy matrix at 77K; the second emission at 600 nm is similar to the emissions observed in DMSO at room temperature. We tentatively ascribe the observation of the two bands to the simultaneous presence of the unrelaxed emissive species (as in the glassy matrix) as well as of relaxed species (as in the liquid solvent). Excitation spectra in Figure 3.10 were collected detecting emitted light at 410 nm and 600 nm. The emission at 600 nm can be safely ascribed to **DMAC-py-TRZ**, the corresponding excitation peaks at 370, in correspondence with the absorption band. The emission at 410 nm has two components, as clearly seen from the excitation spectrum that shows a peak at 370, related to the **DAMC-py-TRZ** absorption and a peak at 340 that is due to the spurious emission from the solvent

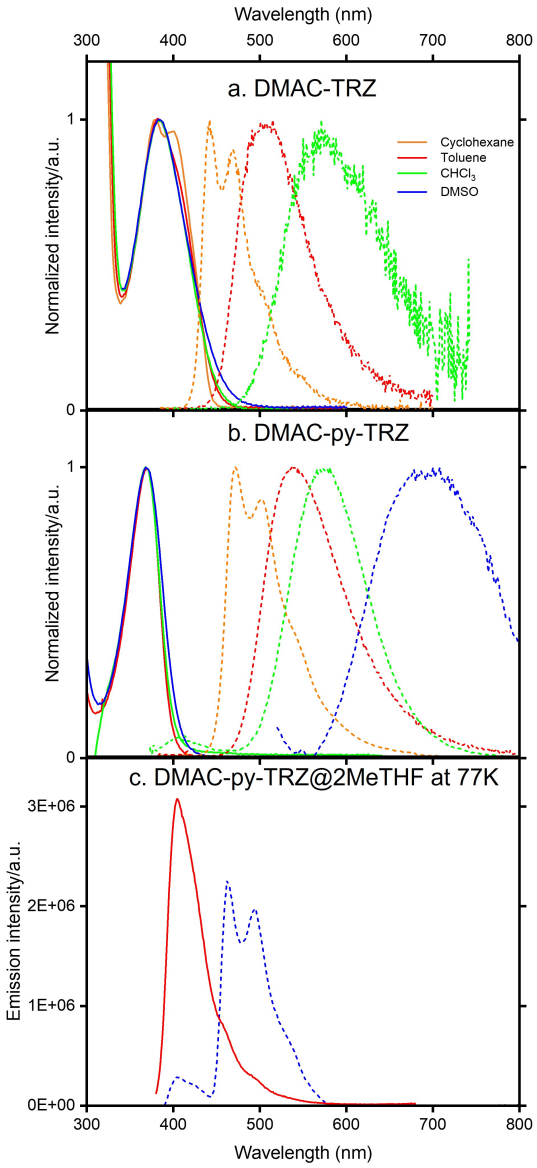

Figure 3.8: Steady state absorption and emission spectra of (a) **DMAC-TRZ** at room temperature; (b) **DMAC-py-TRZ** @ RT Lower panel; (c) emission spectra of **DMAC-py-TRZ** in 2MeTHF at 77K. The blue dotted line show spectra obtained in the same sample, with a gated measurement, collecting light emitted in the time interval 1-7 s following excitation.

(as confirmed by the spectra collected in the pure solvent). Fluorescence anisotropy spectra in Figure 3.10 show a very large value for the anisotropy of 0.38.

In Figure 3.8c, we show spectra collected in a glassy 2MeTHF matrix at 77K. The maximum of the steady state spectrum at 404 nm is largely blue-shifted with respect to the spectra collected in liquid 2MeTHF showing a maximum at 596 nm (Table 3.1) but also

SOLVENT	λ_{abs}	λ_{em} (nm)	$\tau(ns)$	$\Delta\nu(cm^{-1})$	f	$\varepsilon(M^{-1}cm^{-1})$
cyclohexane	370	472	τ_1= 13.11 (97,14%) τ_2= 91.46 (2.86%)	5840	0,21	
toluene	370	550	τ_1= 14.07 (81.79%) τ_2= 77.98 (18.11%)	8845	0,19	34100
chloroform	370	573	τ_1= 10.04 (69,34%) τ_2= 108.90 (30.66%)	9575	0,012	35100
DMSO	368	675	*	12212	*	
2MeTHF (298K)	370	596	τ_1= 8.80 (77.67%) τ_2= 62.90 (22.33%)	10192	0.055	
2MeTHF (77K)	370	404	τ_1= 1.95 (88.94%) τ_2= 2.93 (11.06%)	2275		

Table 3.1: Spectroscopic data: absorption wavelength λ_{abs}, emission wavelength λ_{em}, lifetime τ, Stokes shift $\Delta\nu$, and fluorescence quantum yield (Φ) (reference: fluorescein water 0.1 M NaOH). *the weak emissivity of **DMAC-py-TRZ** in DMSO hinders the estimate of the fluorescence lifetime and quantum yield.

with respect to cyclohexane (472 nm). This suggests that the large variation of the molecular geometry that in cyclohexane is responsible for the large Stokes (abs maximum at 370 nm, emission max 472 nm) is hindered (or partially so) in the frozen matrix, where the Stokes shifts reduce to 0.28 eV (abs max at 370 nm emission 405 nm). The gated signal (blue dotted line in Figure 3.8c collecting the light emitted with a delay of 1s after excitation) is ascribed to phosphorescence, suggesting a large singlet-triplet gap. Figure 3.9 shows emission (λ_{exc}=370 nm) and excitation (λ_{em}= 405 nm) fluorescence anisotropy spectra for DMAC-pyTRZ in 2MeTHF at 77K. Excitation anisotropy is roughly constant 0.25 in the region of the absorption band, suggesting that a single state is responsible for absorption. The emission fluorescence anisotropy decreases at longer wavelengths, possibly due to a contribution from phosphorescence. The ΔE_{ST} of the **DMAC-py-TRZ** was first measured in a frozen (77K) 2Me-THF, 10^{-5}M solution (Figure 3.9). The material presented a triplet energy level of 2.77 eV and a single energy level of 3.21 eV, leading to a high ΔE_{ST} of 0.44 eV. **DMAC-TRZ** presents a slightly smaller energy gap, at 0.33 eV, with T_1 and S_1 energies of 2.57 eV and 2.88 eV.

The emission of **DMAC-TRZ** and **DMAC-py-TRZ** falls at λ_{PL} of 499 nm and 539 nm

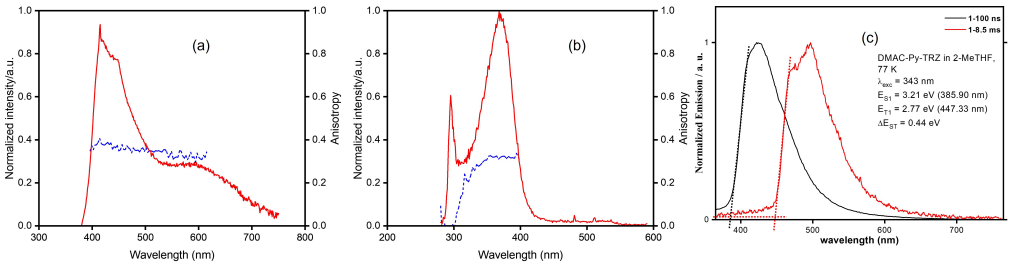

Figure 3.9: (a) Emission (λ_{exc}=370 nm) and (b) excitation (λ_{emis}= 405nm) fluorescence anisotropy spectra of **DMAC-py-TRZ** in 2MeTHF at 77K. (c) Prompt fluorescence and phosphorescence spectra at 77 K in 10^{-5} M 2MeTHF solution (λ_{exc} = 343 nm, prompt and delayed fluorescence spectra were obtained in the $1-100$ ns and $1-8.5$ ms time range, respectively.

respectively. The Φ_{PL} of the two materials was obtained via the relative method, **DMAC-TRZ** an efficiency of 67.3% under N_2, which decreases to 21.8% when exposed to air. As previously reported, the material presents both prompt and delayed fluorescence, with respective lifetimes of 20.8 ns and 5.2μs. **DMAC-py-TRZ** presents slightly lower PLQY, at 58.3% under N_2, which went down to 16.9% when exposed to air. Prompt and delayed fluorescence was also observed, the prompt component presents a longer decay lifetime of 44.0 ns, while the delayed shows a much faster one, at only 1.5μs. Looking at the theoretical ΔE_{ST} values, the presence of a delayed component for **DMAC-py-TRZ** would only be possible from the twisted conformer, since the bent material should present any TADF behavior due to the too large gap between singlet and triplet.

By looking at the behavior of the material in the solution, we can see that is in line with what was predicted by the DFT calculations. For measurement that involves the ground state of the molecule (UV-vis, excitation spectra), the material behaves as expected from the planar conformation, showing a large overlap between HOMO and LUMO, leading to very high ε. As soon as the excited state of the molecule is involved (emission spectra and lifetime measurements), the behavior mirrors what was predicted for the twisted conformer, showing clear evidence of a TADF charge transfer state. These latter results closely resemble the one obtained for **DMAC-TRZ**, which presents a very similar conformation to the twisted conformer of **DMAC-py-TRZ**.

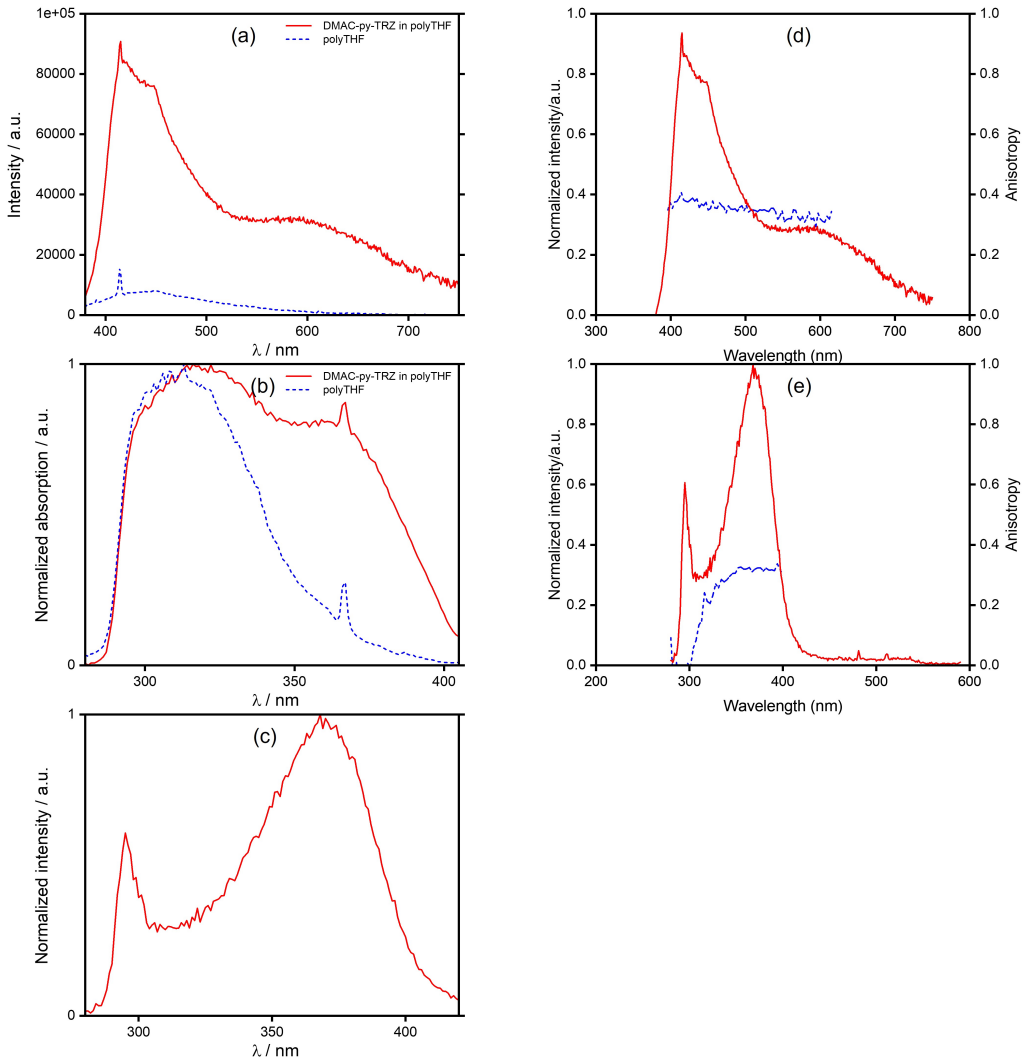

Figure 3.10: a) Emission spectrum (red line) of **DMAC-py-TRZ** dissolved in polyTHF (λ_{exc}=370nm). The blue dotted line is the emission of the pure solvent. b) red line: excitation spectrum collected revealing at 410 nm. The blue dashed line is the excitation spectrum of the solvent, collected revealing the emission at 401 nm. c) excitation spectrum of **DMAC-py-TRZ** in polyTHF collected revealing at 600nm. (d) emission (left, λ_{exc}=370 nm) and (e) excitation (right, λ_{emiss}=600 nm) fluorescence anisotropy spectra.

3.3.3 DMAC-py-TRZ in Solid Matrixes

DMAC-py-TRZ was then doped in amorphous films. In the weakly polar PMMA matrix (Figure 3.11), at a doping concentration of 10 wt%, emission is observed at λ_{PL}= 516 nm with Φ_{PL} 63.8% under N_2 atmosphere, which decreased to 58.0% after exposure to air. Prompt fluorescence is observed with lifetime τ_p 26.0 ns, while delayed fluorescence is better described by two exponentials with τ_1=1.0 μs (32.6%), τ_2=7.4 μs (67.4%). When switching to the more polar host material mCP (Figure 3.11), in 10wt% doped films, we observed a blue shift of the emission color at λ_{PL} of 496 nm, with similar Φ_{PL} as in PMMA films, 57.4% in N_2 atmosphere, 53.5% in air. Prompt and delayed fluorescence were again observed with τ_p 24.9 ns and a bi-exponential fit for the delayed fluorescence with τ_1=1.4 μs (46.8%), τ_2=7.7 μs (53.2%), again in line with PMMA results. The TADF nature of the material was confirmed by measuring the temperature dependence properties of the two samples (Figures 3.11). A clear increase in the emission intensity is observed with increasing temperatures. The ΔE_{ST} in both environments was measured, yielding very similar results with values of 0.02 eV and 0.05 eV for 10 wt% drop-casted PMMA and mCP film respectively (Figure 3.11.

The emission spectra measured in 10% doped films are largely red-shifted, possibly suggesting emission from a relaxed dye in orthogonal conformation. However, at these large concentrations energy-transfer phenomena may occur so that, in a system with the conformational disorder, the emission is only seen from the dyes emitting in the red part of the spectrum. We, therefore, studied films with lower dye concentrations (Figure 8). At a doping concentration of 1 wt%, the blue-shifted emission band appears again and coexists with the red-shifted emission. The blue-shifted emission does not present any delayed component and it is safely ascribed to the bent conformer. The progressive disappearance of the blue-band due to the bent conformer upon increasing the dye concentration then suggests that at 10% concentration the homo transfer is fast enough to completely remove the signal of the bent confirm, quickly transferring all population to the orthogonal conformer. In the neat **DMAC-py-TRZ** film most of the emission is seen at 513 nm, attributed to the orthogonal structure, but a minor peak at 415 nm is also observed that can be attributed to the bent conformation. Lifetimes measured at 500 nm show a prompt fluorescence component (τ_p 56.7 ns) and a bi-exponential delayed component (τ_1=1.0 µs (35.7%), τ_2=4.6 µs (56.1%)). At 425 nm, only prompt fluorescence is observed, confirming the nature of the two emissions. Efficient energy transfer is expected also in neat films, shifting most of the intensity to the red portion of the emission spectrum, however, in this case, a residual emission from the bent structure is seen whose intensity increases at 77 K (Fig.3.12).

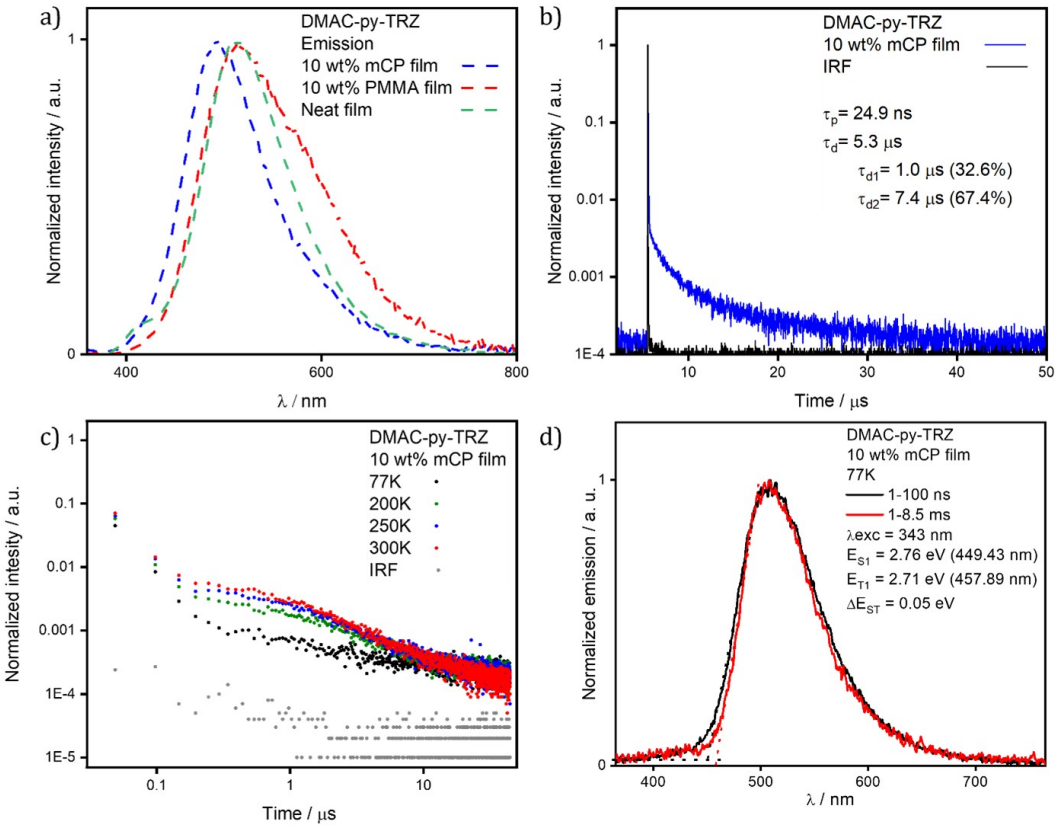

Figure 3.11: (a) Emission spectra of **DMAC-py-TRZ** in spin-coated 10 wt% mCP film, spin-coated 10wt% PMMA film, and drop-casted neat film ($\lambda_{exc} = 340nm$). (b) Time-resolved fluorescence decay in spin-coated 10 wt% mCP film of **DMAC-py-TRZ** ($\lambda_{exc} = 378nm$). (c) Delayed fluorescence decay data measured at different temperatures in spin-coated 10 wt% mCP film of **DMAC-py-TRZ** ($\lambda_{exc} = 378nm$). (d) Prompt fluorescence and phosphorescence spectra at 77 K in drop-casted 10 wt% mCP film ($\lambda_{exc} = 343nm$), prompt and delayed fluorescence spectra were obtained in the 1–100 ns and 1–8.5 ms time range, respectively

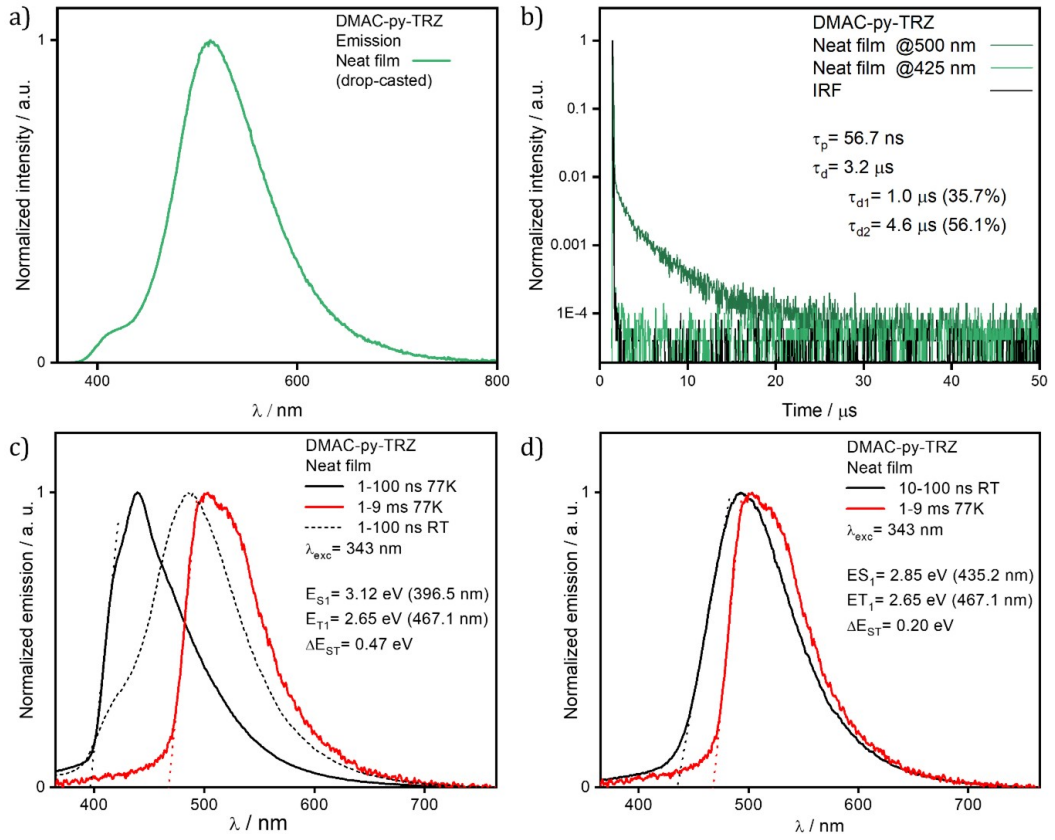

Figure 3.12: a) emission spectra of **DMAC-py-TRZ** in drop casted neat film (λ_{exc}=340 nm); b) time-resolved fluorescence decay in spin-coated 10 wt% mCP film of **DMAC-py-TRZ** collected at λ_{emi}=500 nm and λ_{emi}=425 nm (λ_{exc}=378 nm); Prompt fluorescence and phosphorescence spectra at room temperature and at 77 K in drop-casted neat film (λ_{exc}=343 nm, prompt and delayed fluorescence spectra were obtained in the 1–100 ns and 1–9 ms time range, respectively), and calculation of the ΔE_{ST} from the phosphorescence spectra at 77K and the fluorescence spectra at c) 77K (corresponding to the ΔE_{ST} of the bent conformer), and d) room temperature (corresponding to the ΔE_{ST} of the twisted conformer)

Material	Environment	λ_{PL} $(nm)^a$	Φ_{PL} N_2 $(air)(\%)^b$	τ_p (ns); $\tau_d(\mu s)^e$	S_1 $(eV)^f$	T_1 $(eV)^g$	$\Delta E_{ST}(eV)^i$
DMAC-TRZ	Toluene (10^{-5} M)	499	$67(22)^c$	20.8; 5.2	2.88	2.57	0.31
	mCP 10 wt %	-	-	-	2.83	2.81	0.02
	PMMA 10 wt%	-	-	-	2.85	2.74	0.11
	neat	-	-	-			
DMAC-py-TRZ	Toluene (10^{-5} M)	539	$58(17)^c$	44.0; 1.5	3.21	2.77	0.44
	mCP 10 wt%	496	$57(54)^d$	24.9; 5.3	2.76	2.71	0.05
	PMMA 10 wt%	516	$64(58)^d$	26.0; 4.7	2.76	2.74	0.02
	neat	425^j	$55(54)^d$	-; -	3.12	2.65	0.47
		500^k		56.7; 3.2	2.85^h	2.65	0.2

Table 3.2: ^{a} measured at room temperature; $^b\lambda_{exc}$ = 340 nm; ^{c} obtained via the optically dilute method22 (see SI), quinine sulfate (0.5 M) in H_2SO_4 (aq) was used as the reference, Φ_{PL}: 54.6%, λ_{exc} = 360 nm;23 ^{d} obtained via integrating sphere; $^e\tau_p$ (prompt lifetime) and τ_d (delayed lifetime) were obtained from the transient PL decay of degassed solution/doped film, λ_{exc} = 378 nm; $^f S_1$ was obtained from the onset of the prompt emission measured at 77K;$^g T_1$ was obtained from the onset of the phosphorescence spectrum measured at 77K; $^h S_1$ was obtained from the onset of the fluorescence spectrum measured at room temperature; $^i\Delta E_{ST} = S_1 - T_1$; ^{j} assigned to the bent conformer of **DMAC-py-TRZ**; ^{k} assigned to the twisted conformer of **DMAC-py-TRZ**

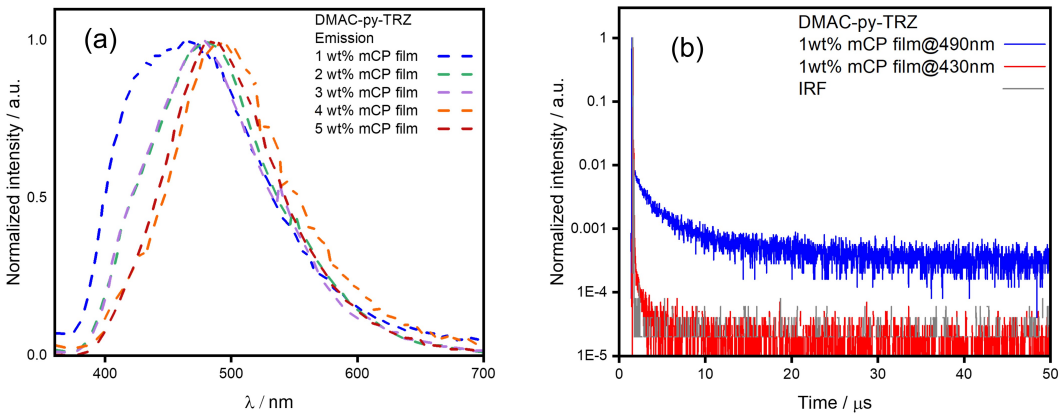

Figure 3.13: (a) screen of low-concentration spin-coated films emission spectra of **DMAC-py-TRZ** in spin-coated 1wt% mCP film (λ_{exc}= 340 nm); (b) time-resolved fluorescence decay in spin-coated 1wt% mCP film of **DMAC-py-TRZ** collected at λ_{emi} = 490 nm and λ_{emi} = 430 nm (λ_{exc} = 378 nm)

3.4 Conclusions

This chapter presents a new TADF dye, **DMAC-py-TRZ**, together with an extensive computational analysis and experimental characterization. The experimental data are collected from the host lab and collaboration lab. The chemical structure of **DMAC-py-TRZ** only marginally differs from that of the parent **DMAC-TRZ** compound, with a CH group substituted by a N atom. However, this minor substitution has an enormous impact on the structure and hence on the photophysics of the dye. Specifically, **DMAC-TRZ** has the same orthogonal geometry in both the ground state and in the first excited singlet, **DMAC-py-TRZ** assumes a bent geometry in the ground state, as best demonstrated by the large oscillator strength measured in solution for this dye. However, upon excitation in the S_1 state, the system undergoes a large geometrical rearrangement that brings it to an orthogonal geometry. This large relaxation is confirmed by the very large Stokes shift measured in non-polar solvents. In frozen (glassy) solvents and low temperatures, the relaxation is hindered and a blue-shifted emission is seen from the unrelaxed bent state. In PMMA and mCP films a distribution of structures is seen, so that, at low concentrations emission is observed both from bent and orthogonal structures. However, upon increasing concentration efficient energy transfer is observed from the bent to the orthogonal structures, so that the spectrum at high concentration is dominated by the red-shifted emission. While TADF is not possible nor observed in the bent structure, due to a too large singlet-triplet energy gap, the efficiency of **DMAC-py-TRZ** devices is similar as for **DMAC-TRZ**: indeed the efficient energy transfer of excitons created on bent (and TADF silent) structures towards molecules in the orthogonal (and TADF-active) structure allows to retrieve all singlet photogenerated states for TADF activity. Most probably, efficient triplet to triplet energy transfer is also required to explain the good efficiency of **DMAC-py-TRZ** OLED, but this will be the subject of a subsequent study.

Conclusions and Perspectives

TADF is a rare phenomenon occurring in systems where a triplet state sits very close in energy to the lowest excited singlet. It requires a delicate balance of several sometimes competing interactions, as to ensure a tiny energy gap between the lowest excited singlet and triplet states, a large spin-orbit coupling between the same states, with the singlet showing reasonable emissive properties. Governing this delicate balance requires the control of the relative energies and mixing of charge-transfer and local excited states, that in turn are affected by vibrational and conformational motions as well as by the interaction with the surrounding. To make the picture even more intricate, the matrix properties, including dielectric properties, mobility, viscosity *etc.*, may affect in different ways states of different nature, with dramatic effects on the relative energies of excited states. Mastering TADF then requires reliable models able to accurately account for the different interactions while maintaining the global picture in control.

This thesis provides a guide and fundamental understanding toward this direction. Having charge-transfer as well local-excited states for TADF dyes, one of the most delicate issues is the choice of the functional to treat all the states properly. This issue is addressed in Chapter 1 and Chapter 2 as well as also got published in Ref. 70 and 160. The dielectric properties of the local environment also largely affect the behavior of TADF dyes. Typically used continuum models lead to wildly different results because of the adiabatic approximation used for solvent electronic degrees of freedom. The development of the antiadiabatic approach is demonstrated to treat the relaxation of the fast (electronic) solvent degree of freedom and this implementation is extensively addressed in Chapter 1. Ref. 35 and 160 contain this discussion further. Chapter 2 represents a detailed discussion of extensive experimental and TD-DFT results for a typical TADF dye, **DMAC-TRZ**. The essential-state model, without adjustable parameters, satisfactorily reproduces the absorption and fluorescence spectra (in terms of band positions and bandshapes) and their evolution with the solvent polarity, as well as absorption, fluorescence and phosphorescence spectra in a solid matrix. The model offers safe guidance on environmental effects on the photophysics of the TADF dye. This is a very important step toward the so-called smart-matrix approach, where the dye and the matrix are optimized together for the best device performance. These results

are published in Ref. 70 and 161. In Chapter 3, a new novel emitter **DMAC-py-TRZ** is discussed in-depth to understand dihedral angle relaxation and excited-state properties. The computational results shed light on an anomalously large Stokes shift observed experimentally, in terms of a large molecular relaxation upon photoexcitation. This work is carried out in close collaboration with Prof. Eli Zysman-Colman, University of St Andrews, Scotland. Based on this understanding, we have developed an approach to simulate TADF dynamics (including the time evolution of spectral properties) in condensed phases.

In conclusion, this thesis provides an original and fundamental approach to reliable models of the TADF process, accounting for the delicate role of environmental effects as well as geometrical effects. A large body of literature is now available that quite unambiguously points to important and highly non-trivial phenomena due to disorder in TADF systems, however, TADF remains a delicate phenomenon that requires precise control of a tiny singlet-triplet gap and of an even tinier and somewhat elusive spin-orbit coupling in systems where molecular vibrations, conformational modes and the interaction with the environment heavily affect the properties of the dye. All the computational approaches developed and discussed in this thesis provide the scientific and technological community with a useful tool as needed to guide the design and synthesis of concurrently optimized TADF dyes. The comprehensive and detailed model presented here is validated against the experiment and should set a solid basis for a reliable simulation of TADF-OLED, which is a prerequisite for the design of efficient devices.

Bibliography

[1] M. Fernández, E. Casanova, and I. Alonso, "Review of display technologies focusing on power consumption," *Sustainability*, vol. 7, pp. 10854–10875, aug 2015.

[2] *Organic Light-Emitting Devices*. Springer US, 2013.

[3] T. M. Brown, R. H. Friend, I. S. Millard, D. J. Lacey, J. H. Burroughes, and F. Cacialli, "LiF/al cathodes and the effect of LiF thickness on the device characteristics and built-in potential of polymer light-emitting diodes," *Applied Physics Letters*, vol. 77, pp. 3096–3098, nov 2000.

[4] Y. Liu, C. Li, Z. Ren, S. Yan, and M. R. Bryce, "All-organic thermally activated delayed fluorescence materials for organic light-emitting diodes," *Nature Reviews Materials*, vol. 3, apr 2018.

[5] Z. Yang, Z. Mao, Z. Xie, Y. Zhang, S. Liu, J. Zhao, J. Xu, Z. Chi, and M. P. Aldred, "Recent advances in organic thermally activated delayed fluorescence materials," *Chemical Society Reviews*, vol. 46, no. 3, pp. 915–1016, 2017.

[6] D. Hu, L. Yao, B. Yang, and Y. Ma, "Reverse intersystem crossing from upper triplet levels to excited singlet: a 'hot excition' path for organic light-emitting diodes," *Philosophical Transactions of the Royal Society A: Mathematical, Physical and Engineering Sciences*, vol. 373, p. 20140318, jun 2015.

[7] Y. Tao, K. Yuan, T. Chen, P. Xu, H. Li, R. Chen, C. Zheng, L. Zhang, and W. Huang, "Thermally activated delayed fluorescence materials towards the breakthrough of organoelectronics," *Advanced Materials*, vol. 26, pp. 7931–7958, sep 2014.

[8] M. Y. Wong and E. Zysman-Colman, "Purely organic thermally activated delayed fluorescence materials for organic light-emitting diodes," *Advanced Materials*, vol. 29, p. 1605444, mar 2017.

[9] C. Adachi, "Third-generation organic electroluminescence materials," *Japanese Journal of Applied Physics*, vol. 53, p. 060101, may 2014.

[10] C. Adachi, M. A. Baldo, M. E. Thompson, and S. R. Forrest, "Nearly 100% internal phosphorescence efficiency in an organic light-emitting device," *Journal of Applied Physics*, vol. 90, pp. 5048–5051, nov 2001.

[11] M. Y. Wong and E. Zysman-Colman, "Purely organic thermally activated delayed fluorescence materials for organic light-emitting diodes," *Advanced Materials*, vol. 29, no. 22, p. 1605444, 2017.

[12] F.-M. Xie, J.-X. Zhou, Y.-Q. Li, and J.-X. Tang, "Effects of the relative position and number of donors and acceptors on the properties of TADF materials," *Journal of Materials Chemistry C*, vol. 8, no. 28, pp. 9476–9494, 2020.

[13] D. Barman, R. Gogoi, K. Narang, and P. K. Iyer, "Recent developments on multifunctional metal-free mechanochromic luminescence and thermally activated delayed fluorescence organic materials," *Frontiers in Chemistry*, vol. 8, p. 483, jun 2020.

[14] C. A. Parker and C. G. Hatchard, "Triplet-singlet emission in fluid solutions. phosphorescence of eosin," *Trans. Faraday Soc.*, vol. 57, pp. 1894–1904, 1961.

[15] A. Endo, K. Sato, K. Yoshimura, T. Kai, A. Kawada, H. Miyazaki, and C. Adachi, "Efficient up-conversion of triplet excitons into a singlet state and its application for organic light emitting diodes," *Applied Physics Letters*, vol. 98, no. 8, p. 083302, 2011.

[16] H. Uoyama, K. Goushi, K. Shizu, H. Nomura, and C. Adachi, "Highly efficient organic light-emitting diodes from delayed fluorescence," *Nature*, vol. 492, pp. 234–238, 2012.

[17] J. Lee, K. Shizu, H. Tanaka, H. Nomura, T. Yasuda, and C. Adachi, "Oxadiazole- and triazole-based highly-efficient thermally activated delayed fluorescence emitters for organic light-emitting diodes," *Journal of Materials Chemistry C*, vol. 1, no. 30, p. 4599, 2013.

[18] F. B. Dias, K. N. Bourdakos, V. Jankus, K. C. Moss, K. T. Kamtekar, V. Bhalla, J. Santos, M. R. Bryce, and A. P. Monkman, "Triplet harvesting with 100% efficiency by way of thermally activated delayed fluorescence in charge transfer OLED emitters," *Advanced Materials*, vol. 25, pp. 3707–3714, may 2013.

[19] Z. Yang, Z. Mao, Z. Xie, Y. Zhang, S. Liu, J. Zhao, J. Xu, Z. Chi, and M. P. Aldred, "Recent advances in organic thermally activated delayed fluorescence materials," *Chemical Society Reviews*, vol. 46, no. 3, pp. 915–1016, 2017.

[20] M. A. El-Sayed, "Spin—orbit coupling and the radiationless processes in nitrogen heterocyclics," *The Journal of Chemical Physics*, vol. 38, pp. 2834–2838, jun 1963.

[21] Mulliken, R. S., "Molecular Compounds and their Spectra. II," *J. Am. Chem. Soc.*, vol. 74, no. 3, pp. 811–824, 1952.

[22] T. Jiang, Y. Liu, Z. Ren, and S. Yan, "The design, synthesis and performance of thermally activated delayed fluorescence macromolecules," *Polymer Chemistry*, vol. 11, no. 9, pp. 1555–1571, 2020.

[23] T. Stein, L. Kronik, and R. Baer, "Reliable prediction of charge transfer excitations in molecular complexes using time-dependent density functional theory," *Journal of the American Chemical Society*, vol. 131, pp. 2818–2820, mar 2009.

[24] H. Sun and J. Autschbach, "Influence of the delocalization error and applicability of optimal functional tuning in density functional calculations of nonlinear optical properties of organic donor-acceptor chromophores," *ChemPhysChem*, vol. 14, pp. 2450–2461, jun 2013.

[25] H. Sun, C. Zhong, and J.-L. Brédas, "Reliable prediction with tuned range-separated functionals of the singlet-triplet gap in organic emitters for thermally activated delayed fluorescence," *Journal of Chemical Theory and Computation*, vol. 11, no. 8, pp. 3851–3858, 2015. PMID: 26574466.

[26] J. Tomasi, B. Mennucci, and R. Cammi, "Quantum mechanical continuum solvation models," *Chem. Rev.*, vol. 105, pp. 2999–3094, 2005.

[27] R. Loudon, *The Quantum Theory of Light*. Oxford, UK: Oxford University Press, 1 ed., 1973.

[28] R. Cammi, S. Corni, B. Mennucci, and J. Tomasi, "Electronic excitation energies of molecules in solution: State specific and linear response methods for nonequilibrium continuum solvation models," *J. Chem. Phys.*, vol. 122, p. 104513, 2005.

[29] S. Corni, R. Cammi, B. Mennucci, and J. Tomasi, "Electronic excitation energies of molecules in solution within continuum solvation models: Investigating the discrepancy between state-specific and linear-response methods," *J. Chem. Phys.*, vol. 123, p. 134512, 2005.

[30] R. Improta, V. Barone, G. Scalmani, and M. J. Frisch, "A state-specific polarizable continuum model time dependent density functional theory method for excited state calculations in solution," *J. Chem. Phys.*, vol. 125, p. 054103, 2006.

[31] A. V. Marenich, C. J. Cramer, D. G. Truhlar, C. A. Guido, B. Mennucci, G. Scalmani, and M. J. Frisch, "Practical computation of electronic excitation in solution: vertical excitation model," *Chem. Sci.*, vol. 2, pp. 2143–2161, 2011.

[32] B. Lunkenheimer and Köhn, "Solvent effects on electronically excited states using the conductor- like screening model and the second-order correlated method adc(2)," *J. Chem. Theory Comput.*, vol. 9, pp. 977–994, 2013.

[33] J. A. Bjorgaard, V. Kuzmenko, K. A. Velizhanin, and S. Tretiak, "Solvent effects in time-dependent selfconsistent field methods. i. optical response calculations," *J. Chem. Phys.*, vol. 142, p. 044103, 2015.

[34] C. A. Guido and S. Caprasecca, "On the description of the environment polarization response to electronic transitions," *Int. J. Quantum Chem.*, vol. 119, p. e25711, 2019.

[35] D. K. A. Phan Huu, R. Dhali, C. Pieroni, F. Di Maiolo, C. Sissa, F. Terenziani, and A. Painelli, "Antiadiabatic view of fast environmental effects on optical spectra," *Phys. Rev. Lett.*, vol. 124, p. 107401, Mar 2020.

[36] A. V. Marenich, C. J. Cramer, and D. G. Truhlar, "Electronic absorption spectra and solvatochromic shifts by the vertical excitation model: Solvated clusters and molecular dynamics sampling," *The Journal of Physical Chemistry B*, vol. 119, pp. 958–967, sep 2014.

[37] T. Vreven and K. Morokuma, "Chapter 3 hybrid methods: Oniom(qm:mm) and qm/mm," vol. 2 of *Annual Reports in Computational Chemistry*, pp. 35–51, Elsevier, 2006.

[38] Y. Olivier, B. Yurash, L. Muccioli, G. D'Avino, O. Mikhnenko, J. C. Sancho-García, C. Adachi, T.-Q. Nguyen, and D. Beljonne, "Nature of the singlet and triplet excitations mediating thermally activated delayed fluorescence," *Physical Review Materials*, vol. 1, dec 2017.

[39] J. Li, G. D'Avino, I. Duchemin, D. Beljonne, and X. Blase, "Accurate description of charged excitations in molecular solids from embedded many-body perturbation theory," *Phys. Rev. B*, vol. 97, p. 035108, 2018.

[40] J. M. Milanese, M. R. Provorse, E. Alameda, and C. M. Isborn, "Convergence of computed aqueous absorption spectra with explicit quantum mechanical solvent," *Journal of Chemical Theory and Computation*, vol. 13, pp. 2159–2171, apr 2017.

[41] M. Stanke, "Adiabatic, born-oppenheimer, and non-adiabatic approaches," in *Handbook of Computational Chemistry*, pp. 1–51, Springer Netherlands, 2015.

[42] E. G. McRae, "Theory of solvent effects on molecular electronic spectra. frequency shifts," *J. Phys. Chem.*, vol. 61, pp. 1128–1129, 1957.

[43] S. Di Bella, T. J. Marks, and M. A. Ratner, "Environmental effects on nonlinear optical chromophore performance. calculation of molecular quadratic hyperpolarizabilities in solvating media," *J. Am. Chem. Soc.*, vol. 116, pp. 4440–4445, 1994.

[44] A. Painelli, "Amplification of nlo responses: vibronic and solvent effects in push-pull polyenes," *Chem. Phys.*, vol. 245, pp. 185–197, 1999.

[45] "See supplemental material at [url will be inserted by publisher] for technical details and additional results."

[46] H. J. Kim and J. T. Hynes, "Equilibrium and nonequilibrium solvation and solute electronic structure. iii. quantum theory," *The Journal of Chemical Physics*, vol. 96, pp. 5088–5110, 1992.

[47] M. V. Basilevsky, G. E. Chudinov, and M. D. Newton, "The multi-configurational adiabatic electron transfer theory and its invariance under transformations of charge density basis functions," *Chemical Physics*, vol. 179, pp. 263–278, 1994.

[48] W. Liptay, "Electrochromism and solvatochromism," *Angewandte Chemie International Edition in English*, vol. 8, no. 3, pp. 177–188, 1969.

[49] A. Painelli and F. Terenziani, "A non-perturbative approach to solvatochromic shifts of push-pull chromophores," *Chem. Phys. Lett.*, vol. 312, pp. 211–220, 1999.

[50] J. Gilmore and R. H. McKenzie, "Spin boson models for quantum decoherence of electronic excitations of biomolecules and quantum dots in a solvent," *Journal of Physics: Condensed Matter*, vol. 17, pp. 1735–1746, 2005.

[51] F. Terenziani, A. Painelli, C. Katan, M. Charlot, and M. Blanchard-Desce, "Charge instability in quadrupolar chromophores: Symmetry breaking and solvatochromism," *Journal of the American Chemical Society*, vol. 128, no. 49, pp. 15742–15755, 2006. PMID: 17147384.

[52] A. Amadei, M. D'Alessandro, M. D'Abramo, and M. Aschi, "Theoretical characterization of electronic states in interacting chemical systems," *J. Chem. Phys.*, vol. 130, no. 8, p. 084109, 2009.

[53] S. Sanyal, C. Sissa, F. Terenziani, S. K. Pati, and A. Painelli, "Superlinear amplification of the first hyperpolarizability of linear aggregates of dans molecules," *Phys.Chem.Chem.Phys*, vol. 19, pp. 24979–24984, 2017.

[54] C. Reichardt, "Solvatochromic dyes as solvent polarity indicators," *Chem. Rev.*, vol. 94, no. 8, pp. 2319–2358, 1994.

[55] M. K. Etherington, F. Franchello, J. Gibson, Y. Northey, J. Santos, J. S. Ward, H. F. Higginbotham, P. Data, A. Kurowska, P. L. Dos Santos, D. R. Graves, A. S. Batsanov, F. B. Dias, M. R. Bryce, T. J. Penfold, and A. P. Monkman, "Regio- and conformational isomerization critical to design of efficient thermally-activated delayed fluorescence emitters.," *J. Amer. Chem. Soc.*, vol. 128, p. 14987, 2006.

[56] M. J. Frisch, G. W. Trucks, H. B. Schlegel, G. E. Scuseria, M. A. Robb, J. R. Cheeseman, G. Scalmani, V. Barone, G. A. Petersson, H. Nakatsuji, X. Li, M. Caricato, A. V. Marenich, J. Bloino, B. G. Janesko, R. Gomperts, B. Mennucci, H. P. Hratchian, J. V. Ortiz, A. F. Izmaylov, J. L. Sonnenberg, D. Williams-Young, F. Ding, F. Lipparini, F. Egidi, J. Goings, B. Peng, A. Petrone, T. Henderson, D. Ranasinghe, V. G. Zakrzewski, J. Gao, N. Rega, G. Zheng, W. Liang, M. Hada, M. Ehara, K. Toyota, R. Fukuda, J. Hasegawa, M. Ishida, T. Nakajima, Y. Honda, O. Kitao, H. Nakai, T. Vreven, K. Throssell, J. A. Montgomery, Jr., J. E. Peralta, F. Ogliaro, M. J. Bearpark, J. J. Heyd, E. N. Brothers, K. N. Kudin, V. N. Staroverov, T. A. Keith, R. Kobayashi, J. Normand, K. Raghavachari, A. P. Rendell, J. C. Burant, S. S. Iyengar, J. Tomasi, M. Cossi, J. M. Millam, M. Klene, C. Adamo, R. Cammi, J. W. Ochterski, R. L. Martin, K. Morokuma, O. Farkas, J. B. Foresman, and D. J. Fox, "Gaussian 16 Revision B.01."

[57] L. Tian and C. Feiwu, "Multiwfn: A multifunctional wavefunction analyzer," *J. Comput. Chem.*, vol. 33, pp. 580–592, 2012.

[58] C. A. Guido and S. Caprasecca, "On the description of the environment polarization response to electronic transitions," *International Journal of Quantum Chemistry*, vol. 119, no. 1, p. e25711, 2019.

[59] R. Cammi, S. Corni, B. Mennucci, and J. Tomasi, "Electronic excitation energies of molecules in solution: State specific and linear response methods for nonequilibrium continuum solvation models," *The Journal of Chemical Physics*, vol. 122, no. 10, p. 104513, 2005.

[60] R. Improta, V. Barone, G. Scalmani, and M. J. Frisch, "A state-specific polarizable continuum model time dependent density functional theory method for excited state calculations in solution," *The Journal of Chemical Physics*, vol. 125, no. 5, p. 054103, 2006.

[61] M. Caricato, B. Mennucci, J. Tomasi, F. Ingrosso, R. Cammi, S. Corni, and G. Scalmani, "Formation and relaxation of excited states in solution: A new time dependent polarizable continuum model based on time dependent density functional theory," *The Journal of Chemical Physics*, vol. 124, no. 12, p. 124520, 2006.

[62] C. Guido and S. Caprasecca, "How to perform corrected linear response calculations in g09," 03 2016.

[63] J. Foresman and A. Frisch, *Exploring Chemistry With Electronic Structure Methods, 3rd edition*. 01 2015.

[64] Lakowicz, J. R., *Principles of Fluorescence Spectroscopy*. Springer US, 1999.

[65] I. Duchemin, D. Jacquemin, and X. Blase, "Combining the gw formalism with the polarizable continuum model: A state-specific non-equilibrium approach," *J. Chem. Phys.*, vol. 144, no. 16, p. 164106, 2016.

[66] I. Duchemin, C. A. Guido, D. Jacquemin, and X. Blase, "The bethe-salpeter formalism with polarisable continuum embedding: reconciling linear-response and state-specific features," *Chem. Sci.*, vol. 9, pp. 4430–4443, 2018.

[67] S. Hirata and M. Head-Gordon, "Time-dependent density functional theory within the tamm–dancoff approximation," *Chem. Phys. Lett.*, vol. 314, pp. 291–299, 1999.

[68] T. Stein, L. Kronik, and R. Baer, "Reliable prediction of charge transfer excitations in molecular complexes using time-dependent density functional theory," *Journal of the American Chemical Society*, vol. 131, pp. 2818–2820, mar 2009.

[69] L. Kronik, T. Stein, S. Refaely-Abramson, and R. Baer, "Excitation gaps of finite-sized systems from optimally tuned range-separated hybrid functionals," *J. Chem. Theory Comput.*, vol. 8, pp. 1515–1531, 2012.

[70] R. Dhali, D. K. A. P. Huu, F. Bertocchi, C. Sissa, F. Terenziani, and A. Painelli, "Understanding tadf: a joint experimental and theoretical study of dmac-trz," *Phys. Chem. Chem. Phys.*, 2021.

[71] A. D. Becke, "Density-functional thermochemistry. iii. the role of exact exchange," *The Journal of Chemical Physics*, vol. 98, no. 7, pp. 5648–5652, 1993.

[72] Y. Zhao and D. G. Truhlar, "The m06 suite of density functionals for main group thermochemistry, thermochemical kinetics, noncovalent interactions, excited states,

and transition elements: two new functionals and systematic testing of four m06-class functionals and 12 other functionals," *Theor. Chem. Acc.*, vol. 120, pp. 215–241, 2008.

[73] T. Yanai, D. P. Tew, and N. C. Handy, "A new hybrid exchange–correlation functional using the coulomb-attenuating method (cam-b3lyp)," *Chem. Phys. Lett.*, vol. 393, pp. 51–57, 2004.

[74] S. Hirata and M. Head-Gordon, "Time-dependent density functional theory within the tamm–dancoff approximation," *Chem. Phys. Lett.*, vol. 314, pp. 291–299, 1999.

[75] M. K. Etherington, J. Gibson, H. F. Higginbotham, T. J. Penfold, and A. P. Monkman, "Revealing the spin–vibronic coupling mechanism of thermally activated delayed fluorescence," *Nat. Commun.*, vol. 7, 2016.

[76] M. K. Etherington, F. Franchello, J. Gibson, T. Northey, J. Santos, J. S. Ward, H. F. Higginbotham, P. Data, A. Kurowska, P. L. D. Santos, D. R. Graves, A. S. Batsanov, F. B. Dias, M. R. Bryce, T. J. Penfold, and A. P. Monkman, "Regio- and conformational isomerization critical to design of efficient thermally-activated delayed fluorescence emitters," *Nat. Commun.*, vol. 8, 2017.

[77] T. J. Penfold, E. Gindensperger, C. Daniel, and C. M. Marian, "Spin-vibronic mechanism for intersystem crossing," *Chem. Rev.*, vol. 118, pp. 6975–7025, 2018.

[78] T. Lu and F. Chen, "Multiwfn: A multifunctional wavefunction analyzer," *J. Comput. Chem.*, vol. 33, pp. 580–592, 2012.

[79] Z. Tu, G. Han, T. Hu, R. Duan, and Y. Yi, "Nature of the lowest singlet and triplet excited states of organic thermally activated delayed fluorescence emitters: A self-consistent quantum mechanics/embedded charge study," *Chem. Mater.*, vol. 31, pp. 6665–6671, 2019.

[80] Y. Gao, Y. Geng, Y. Wu, M. Zhang, and Z.-M. Su, "Investigation on the effect of connected bridge on thermally activated delayed fluorescence property for dcbpy emitter," *Dyes and Pigments*, vol. 145, pp. 277–284, 2017.

[81] P. K. Samanta, D. Kim, V. Coropceanu, and J.-L. Brédas, "Up-conversion intersystem crossing rates in organic emitters for thermally activated delayed fluorescence: Impact of the nature of singlet vs triplet excited states," *J. Am. Chem. Soc.*, vol. 139, pp. 4042–4051, 2017.

[82] T.-T. Huang and E. Y. Li, "Enhanced spin-orbit coupling driven by state mixing in organic molecules for oled applications," *Organic Electronics*, vol. 39, pp. 311–317, 2016.

[83] T. Northey, J. Stacey, and T. J. Penfold, "The role of solid state solvation on the charge transfer state of a thermally activated delayed fluorescence emitter," *J. Mater. Chem. C*, vol. 5, pp. 11001–11009, 2017.

[84] L. Lv, K. Yuan, Y. Zhu, G. Zuo, and Y. Wang, "Investigation of conversion and decay processes in thermally activated delayed fluorescence copper(i) molecular crystal: Theoretical estimations from an ONIOM approach combined with the tuned range-separated density functional theory," *The Journal of Physical Chemistry A*, vol. 123, pp. 2080–2090, feb 2019.

[85] T. Hu, G. Han, Z. Tu, R. Duan, and Y. Yi, "Origin of high efficiencies for thermally activated delayed fluorescence organic light-emitting diodes: Atomistic insight into molecular orientation and torsional disorder," *J. Phys. Chem. C*, vol. 122, pp. 27191–27197, nov 2018.

[86] H. Sun, X. Yin, Z.-P. Liu, S.-L. Wei, J.-Z. Fan, L.-L. Lin, and Y.-P. Sun, "Theoretical insights on the luminescent mechanism of an efficient aggregation-induced nondoped delayed fluorescence emitter using QM / MM method," *Int. J. Quantum Chem*, sep 2020.

[87] J. Fan, Y. Zhang, Y. Ma, Y. Song, L. Lin, Y. Xu, and C.-K. Wang, "The role of intermolecular interactions in regulating the thermally activated delayed fluorescence and charge transfer properties: a theoretical perspective," *J. Mater. Chem. C*, vol. 8, no. 25, pp. 8601–8612, 2020.

[88] K. Zhang, L. Cai, J. Fan, Y. Zhang, L. Lin, and C.-K. Wang, "Effect of intermolecular interaction on excited-state properties of thermally activated delayed fluorescence molecules in solid phase: A QM/MM study," *Spectrochim. Acta A*, vol. 209, pp. 248–255, feb 2019.

[89] Y.-J. Gao, W.-K. Chen, Z.-R. Wang, W.-H. Fang, and G. Cui, "QM and ONIOM studies on thermally activated delayed fluorescence of copper(i) complexes in gas phase, solution, and crystal," *Phys. Chem. Chem. Phys.*, vol. 20, no. 38, pp. 24955–24967, 2018.

[90] Q. Wang, Y.-J. Gao, T.-T. Zhang, J. Han, and G. Cui, "QM/MM studies on luminescence mechanism of dinuclear copper iodide complexes with thermally activated delayed fluorescence," *RSC Adv.*, vol. 9, no. 36, pp. 20786–20795, 2019.

[91] C. Tu and W. Liang, "Nb-type electronic asymmetric compounds as potential blue-color tadf emitters: Steric hindrance, substitution effect, and electronic characteristics," *ACS Omega*, vol. 2, pp. 3098–3109, 2017.

[92] G. Valchanov, A. Ivanova, A. Tadjer, D. Chercka, and M. Baumgarten, "Understanding the fluorescence of tadf light-emitting dyes," *J. Phys. Chem. A*, vol. 120, pp. 6944–6955, 2016.

[93] G. Grybauskaite-Kaminskiene, K. Ivaniuk, G. Bagdziunas, P. Turyk, P. Stakhira, G. Baryshnikov, D. Volyniuk, V. Cherpak, B. Minaev, Z. Hotra, H. Ågren, and J. V. Grazulevicius, "Contribution of tadf and exciplex emission for efficient "warm-white" oleds," *J. Mater. Chem. C.*, vol. 6, pp. 1543–1550, 2018.

[94] T. Cardeynaels, S. Paredis, A. Danos, D. Vanderzande, A. P. Monkman, B. Champagne, and W. Maes, "Benzo[1,2-b:4,5-b']dithiophene as a weak donor component for push-pull materials displaying thermally activated delayed fluorescence or room temperature phosphorescence," *Dyes and Pigments*, p. 109022, 2020.

[95] C. Wang, C. Deng, D. Wang, and Q. Zhang, "Prediction of intramolecular charge-transfer excitation for thermally activated delayed fluorescence molecules from a descriptor-tuned density functional," *J. Phys. Chem. C*, vol. 122, pp. 7816–7823, 2018.

[96] L. Wang, T. Li, P. Feng, and Y. Song, "Theoretical tuning of the singlet–triplet energy gap to achieve efficient long-wavelength thermally activated delayed fluorescence emitters: the impact of substituents," *Phys. Chem. Chem. Phys.*, vol. 19, pp. 21639–21647, 2017.

[97] C. He, Z. Li, Y. Lei, W. Zou, and B. Suo, "Unraveling the emission mechanism of radical-based organic light-emitting diodes," *J. Phys. Chem. Lett.*, vol. 10, pp. 574–580, 2019.

[98] H. Sun, Z. Hu, C. Zhong, X. Chen, Z. Sun, and J.-L. Brédas, "Impact of dielectric constant on the singlet–triplet gap in thermally activated delayed fluorescence materials," *J. Phys. Chem. Lett.*, vol. 8, pp. 2393–2398, 2017.

[99] M. Moral, J. Tolosa, J. Canales-Vázquez, J. C. Sancho-García, A. Garzón-Ruiz, and J. C. García-Martínez, "Combined theoretical and experimental study on intramolecular charge transfer processes in star-shaped conjugated molecules," *J. Phys. Chem. C*, vol. 123, pp. 11179–11188, 2019.

[100] I. Lyskov, M. Etinski, C. M. Marian, and S. P. Russo, "Exciton energy transfer in organic light emitting diodes with thermally activated delayed fluorescence dopants," *Journal of Materials Chemistry C*, vol. 6, no. 25, pp. 6860–6868, 2018.

[101] T. J. Penfold, F. B. Dias, and A. P. Monkman, "The theory of thermally activated delayed fluorescence for organic light emitting diodes," *Chem. Commun.*, vol. 54, pp. 3926–3935, 2018.

[102] R. Ishimatsu, S. Matsunami, K. Shizu, C. Adachi, K. Nakano, and T. Imato, "Solvent effect on thermally activated delayed fluorescence by 1,2,3,5-tetrakis(carbazol-9-yl)-4,6-dicyanobenzene," *J. Phys. Chem. A*, vol. 117, pp. 5607–5612, 2013.

[103] M. Hong, M. K. Ravva, P. Winget, and J.-L. Brédas, "Effect of substituents on the electronic structure and degradation process in carbazole derivatives for blue oled host materials," *Chem. Mater.*, vol. 28, pp. 5791–5798, 2016.

[104] D. K. A. P. Huu, C. Sissa, F. Terenziani, and A. Painelli, "Optical spectra of organic dyes in condensed phases: the role of the medium polarizability," *Physical Chemistry Chemical Physics*, vol. 22, no. 44, pp. 25483–25491, 2020.

[105] P. de Silva, "Inverted singlet–triplet gaps and their relevance to thermally activated delayed fluorescence," *The Journal of Physical Chemistry Letters*, vol. 10, pp. 5674–5679, sep 2019.

[106] J. Ehrmaier, E. J. Rabe, S. R. Pristash, K. L. Corp, C. W. Schlenker, A. L. Sobolewski, and W. Domcke, "Singlet–triplet inversion in heptazine and in polymeric carbon nitrides," *The Journal of Physical Chemistry A*, vol. 123, pp. 8099–8108, aug 2019.

[107] R. Pollice, P. Friederich, C. Lavigne, G. dos Passos Gomes, and A. Aspuru-Guzik, "Organic molecules with inverted gaps between first excited singlet and triplet states and appreciable fluorescence rates," *Matter*, vol. 4, no. 5, pp. 1654–1682, 2021.

[108] J. Sanz-Rodrigo, G. Ricci, Y. Olivier, and J. C. Sancho-García, "Negative singlet–triplet excitation energy gap in triangle-shaped molecular emitters for efficient triplet harvesting," *The Journal of Physical Chemistry A*, vol. 125, pp. 513–522, jan 2021.

[109] G. Ricci, E. San-Fabián, Y. Olivier, and J. C. Sancho-García, "Singlet-triplet excited-state inversion in heptazine and related molecules: Assessment of TD-DFT and ab initio methods," *ChemPhysChem*, feb 2021.

[110] H. Hayashi, N. Watanabe, Y. Udagawa, and C.-C. Kao, "The complete optical spectrum of liquid water measured by inelastic x-ray scattering," *Proceedings of the National Academy of Sciences*, vol. 97, pp. 6264–6266, may 2000.

[111] D. Feinberg, S. Ciuchi, and F. De Pasquale, "Squeezing phenomena in interacting electron-phonon systems," *Int. J. Modern Phys. B*, vol. 4, pp. 1317–1367, 1990.

[112] C. A. Guido, M. Rosa, R. Cammi, and S. Corni, "An open quantum system theory for polarizable continuum models," *The Journal of Chemical Physics*, vol. 152, p. 174114, may 2020.

[113] H. Sun, C. Zhong, and J.-L. Brédas, "Reliable prediction with tuned range-separated functionals of the singlet-triplet gap in organic emitters for thermally activated delayed fluorescence," *Journal of Chemical Theory and Computation*, vol. 11, no. 8, pp. 3851–3858, 2015. PMID: 26574466.

[114] K. A. Nguyen, P. N. Day, and R. Pachter, "The performance and relationship among range-separated schemes for density functional theory," *The Journal of Chemical Physics*, vol. 135, no. 7, p. 074109, 2011.

[115] O. A. Vydrov and G. E. Scuseria, "Assessment of a long-range corrected hybrid functional," *The Journal of Chemical Physics*, vol. 125, no. 23, p. 234109, 2006.

[116] A. E. Raeber and B. M. Wong, "The importance of short- and long-range exchange on various excited state properties of dna monomers, stacked complexes, and watson-crick pairs," *Journal of Chemical Theory and Computation*, vol. 11, no. 5, pp. 2199–2209, 2015. PMID: 26574420.

[117] L. Kronik, T. Stein, S. Refaely-Abramson, and R. Baer, "Excitation gaps of finite-sized systems from optimally tuned range-separated hybrid functionals," *Journal of Chemical Theory and Computation*, vol. 8, no. 5, pp. 1515–1531, 2012. PMID: 26593646.

[118] C. S. Oh, D. de Sa Pereira, S. H. Han, H.-J. Park, H. F. Higginbotham, A. P. Monkman, and J. Y. Lee, "Dihedral angle control of blue thermally activated delayed fluorescent emitters through donor substitution position for efficient reverse intersystem crossing," *ACS Applied Materials & Interfaces*, vol. 10, pp. 35420–35429, sep 2018.

[119] F. B. Dias, J. Santos, D. R. Graves, P. Data, R. S. Nobuyasu, M. A. Fox, A. S. Batsanov, T. Palmeira, M. N. Berberan-Santos, M. R. Bryce, and A. P. Monkman, "The role of local triplet excited states and d-a relative orientation in thermally activated

delayed fluorescence: Photophysics and devices," *Advanced Science*, vol. 3, no. 12, p. 1600080, 2016.

[120] X.-K. Chen, D. Kim, and J.-L. Brédas, "Thermally activated delayed fluorescence (TADF) path toward efficient electroluminescence in purely organic materials: Molecular level insight," *Accounts of Chemical Research*, vol. 51, pp. 2215–2224, aug 2018.

[121] X.-K. Chen, S.-F. Zhang, J.-X. Fan, and A.-M. Ren, "Nature of highly efficient thermally activated delayed fluorescence in organic light-emitting diode emitters: Nonadiabatic effect between excited states," *The Journal of Physical Chemistry C*, vol. 119, pp. 9728–9733, apr 2015.

[122] J. Gibson, A. P. Monkman, and T. J. Penfold, "The importance of vibronic coupling for efficient reverse intersystem crossing in thermally activated delayed fluorescence molecules," *ChemPhysChem*, vol. 17, no. 19, pp. 2956–2961, 2016.

[123] I. Lyskov and C. M. Marian, "Climbing up the ladder: Intermediate triplet states promote the reverse intersystem crossing in the efficient TADF emitter ACRSA," *The Journal of Physical Chemistry C*, vol. 121, pp. 21145–21153, sep 2017.

[124] T. J. Penfold, E. Gindensperger, C. Daniel, and C. M. Marian, "Spin-vibronic mechanism for intersystem crossing," *Chemical Reviews*, vol. 118, pp. 6975–7025, mar 2018.

[125] G. Méhes, K. Goushi, W. J. Potscavage, and C. Adachi, "Influence of host matrix on thermally-activated delayed fluorescence: Effects on emission lifetime, photoluminescence quantum yield, and device performance," *Organic Electronics*, vol. 15, pp. 2027–2037, sep 2014.

[126] P. L. dos Santos, J. S. Ward, M. R. Bryce, and A. P. Monkman, "Using guest–host interactions to optimize the efficiency of TADF OLEDs," *The Journal of Physical Chemistry Letters*, vol. 7, pp. 3341–3346, aug 2016.

[127] T. Northey, J. Stacey, and T. J. Penfold, "The role of solid state solvation on the charge transfer state of a thermally activated delayed fluorescence emitter," *Journal of Materials Chemistry C*, vol. 5, no. 42, pp. 11001–11009, 2017.

[128] Y. Olivier, J.-C. Sancho-Garcia, L. Muccioli, G. D'Avino, and D. Beljonne, "Computational design of thermally activated delayed fluorescence materials: The challenges ahead," *The Journal of Physical Chemistry Letters*, vol. 9, no. 20, pp. 6149–6163, 2018.

[129] J.-M. Mewes, "Modeling TADF in organic emitters requires a careful consideration of the environment and going beyond the franck–condon approximation," *Physical Chemistry Chemical Physics*, vol. 20, no. 18, pp. 12454–12469, 2018.

[130] R. Skaisgiris, T. Serevičius, K. Kazlauskas, Y. Geng, C. Adachi, and S. Juršėnas, "Origin of dual emission in σ-bridged donor–acceptor TADF compounds," *Journal of Materials Chemistry C*, vol. 7, no. 40, pp. 12601–12609, 2019.

[131] W.-L. Tsai, M.-H. Huang, W.-K. Lee, Y.-J. Hsu, K.-C. Pan, Y.-H. Huang, H.-C. Ting, M. Sarma, Y.-Y. Ho, H.-C. Hu, C.-C. Chen, M.-T. Lee, K.-T. Wong, and C.-C. Wu, "A versatile thermally activated delayed fluorescence emitter for both highly efficient doped and non-doped organic light emitting devices," *Chem. Commun.*, vol. 51, pp. 13662–13665, 2015.

[132] C. Reichardt, "Solvatochromic dyes as solvent polarity indicators," *Chemical Reviews*, vol. 94, no. 8, pp. 2319–2358, 1994.

[133] Painelli, A. and Terenziani, F., "Optical Spectra of Push-Pull Chromophores in Solution: A Simple Model," *The Journal of Physical Chemistry A*, vol. 104, no. 47, pp. 11041–11048, 2000.

[134] B. Boldrini, E. Cavalli, A. Painelli, and F. Terenziani, "Polar dyes in solution: A joint experimental and theoretical study of absorption and emission band shapes," *J. Phys. Chem. A*, vol. 106, pp. 6286–6294, 2002.

[135] Terenziani, F. and Painelli, A., "Two-dimensional electronic-vibrational spectra: modeling correlated electronic and nuclear motion," *Phys. Chem. Chem. Phys.*, vol. 17, pp. 13074–13081, 2015.

[136] F. Neese, "The orca program system," *WIREs Computational Molecular Science*, vol. 2, no. 1, pp. 73–78, 2012.

[137] F. Neese, "Efficient and accurate approximations to the molecular spin-orbit coupling operator and their use in molecular g-tensor calculations," *The Journal of Chemical Physics*, vol. 122, no. 3, p. 034107, 2005.

[138] M. D. Hanwell, D. E. Curtis, D. C. Lonie, T. Vandermeersch, E. Zurek, and G. R. Hutchison, "Avogadro: an advanced semantic chemical editor, visualization, and analysis platform," *Journal of Cheminformatics*, vol. 4, p. 17, Aug 2012.

[139] J. Eng, B. A. Laidlaw, and T. J. Penfold, "On the geometry dependence of tuned-range separated hybrid functionals," *Journal of Computational Chemistry*, vol. 40, no. 25, pp. 2191–2199, 2019.

[140] R. Cammi and B. Mennucci, "Linear response theory for the polarizable continuum model," *The Journal of Chemical Physics*, vol. 110, no. 20, pp. 9877–9886, 1999.

[141] M. Caricato, B. Mennucci, J. Tomasi, F. Ingrosso, R. Cammi, S. Corni, and G. Scalmani, "Formation and relaxation of excited states in solution: A new time dependent polarizable continuum model based on time dependent density functional theory," *The Journal of Chemical Physics*, vol. 124, no. 12, p. 124520, 2006.

[142] R. Improta, V. Barone, G. Scalmani, and M. J. Frisch, "A state-specific polarizable continuum model time dependent density functional theory method for excited state calculations in solution," *The Journal of Chemical Physics*, vol. 125, no. 5, p. 054103, 2006.

[143] C. Sissa, V. Calabrese, M. Cavazzini, L. Grisanti, F. Terenziani, S. Quici, and A. Painelli, "Tuning the nature of the fluorescent state: A substituted polycondensed dye as a case study," *Chemistry - A European Journal*, vol. 19, pp. 924–935, nov 2012.

[144] L. Grisanti, C. Sissa, F. Terenziani, A. Painelli, D. Roberto, F. Tessore, R. Ugo, S. Quici, I. Fortunati, E. Garbin, C. Ferrante, and R. Bozio, "Enhancing the efficiency of two-photon absorption by metal coordination," *Physical Chemistry Chemical Physics*, vol. 11, no. 41, p. 9450, 2009.

[145] S. Sanyal, C. Sissa, F. Terenziani, S. K. Pati, and A. Painelli, "Superlinear amplification of the first hyperpolarizability of linear aggregates of dans molecules," *Phys. Chem. Chem. Phys.*, vol. 19, pp. 24979–24984, 2017.

[146] Painelli, A., "Vibronic contribution to static NLO properties: exact results for the DA dimer," *Chemical Physics Letters*, vol. 285, no. 5, pp. 352 – 358, 1998.

[147] Á. Piñeiro, P. Brocos, A. Amigo, M. Pintos, and R. Bravo, "Refractive indexes of binary mixtures of tetrahydrofuran with 1-alkanols at 25°c and temperature dependence of n and ρ for the pure liquids," *Journal of Solution Chemistry*, vol. 31, pp. 369–380, May 2002.

[148] G. U. Bublitz and S. G. Boxer, "Effective polarity of frozen solvent glasses in the vicinity of dipolar solutes," *Journal of the American Chemical Society*, vol. 120, no. 16, pp. 3988–3992, 1998.

[149] S. Di Bella, T. J. Marks, and M. A. Ratner, "Environmental effects on nonlinear optical chromophore performance. calculation of molecular quadratic hyperpolariz-

abilities in solvating media," *Journal of the American Chemical Society*, vol. 116, pp. 4440–4445, may 1994.

[150] Di Maiolo, F. and Painelli, A., "Intermolecular Energy Transfer in Real Time," *J. Chem. Theory Comput.*, vol. 14, no. 10, pp. 5339–5349, 2018.

[151] F. Di Maiolo and A. Painelli, "Dynamical disorder and resonance energy transfer: a novel quantum-classical approach," *Physical Chemistry Chemical Physics*, vol. 22, no. 3, pp. 1061–1068, 2020.

[152] W. Li, X. Cai, B. Li, L. Gan, Y. He, K. Liu, D. Chen, Y.-C. Wu, and S.-J. Su, "Adamantane-substituted acridine donor for blue dual fluorescence and efficient organic light-emitting diodes," *Angewandte Chemie*, dec 2018.

[153] Y. Wada, S. Kubo, and H. Kaji, "Adamantyl substitution strategy for realizing solution-processable thermally stable deep-blue thermally activated delayed fluorescence materials," *Advanced Materials*, vol. 30, p. 1705641, jan 2018.

[154] Y. Wada, H. Nakagawa, and H. Kaji, "Acceleration of reverse intersystem crossing using different types of charge transfer states," *Chemistry – An Asian Journal*, vol. 16, pp. 1073–1076, mar 2021.

[155] Y.-Z. Shi, K. Wang, S.-L. Zhang, X.-C. Fan, Y. Tsuchiya, Y.-T. Lee, G.-L. Dai, J.-X. Chen, C.-J. Zheng, S.-Y. Xiong, X.-M. Ou, J. Yu, J.-S. Jie, C.-S. Lee, C. Adachi, and X.-H. Zhang, "Characterizing the conformational distribution in an amorphous film of an organic emitter and its application in a "self-doping" organic light-emitting diode," *Angewandte Chemie*, vol. 133, pp. 26082–26087, nov 2021.

[156] J.-X. Chen, Y.-F. Xiao, K. Wang, X.-C. Fan, C. Cao, W.-C. Chen, X. Zhang, Y.-Z. Shi, J. Yu, F.-X. Geng, X.-H. Zhang, and C.-S. Lee, "Origin of thermally activated delayed fluorescence in a donor–acceptor type emitter with an optimized nearly planar geometry," *Journal of Materials Chemistry C*, vol. 8, no. 38, pp. 13263–13269, 2020.

[157] D. K. A. Phan Huu, S. Saseendran, and A. Painelli, "Effective models for TADF: the role of the medium polarizability," *Journal of Materials Chemistry C*, 2022.

[158] Terenziani, F. and Painelli, A. and Girlando, A. and Metzger, R. M., "From Solution to Langmuir-Blodgett Films: Spectroscopic Study of a Zwitterionic Dye," *The Journal of Physical Chemistry B*, vol. 108, no. 30, pp. 10743–10750, 2004.

[159] A. Painelli, "Amplification of nlo responses: vibronic and solvent effects in push–pull polyenes," *Chemical Physics*, vol. 245, no. 1, pp. 185 – 197, 1999.

[160] R. Dhali, D. K. A. Phan Huu, F. Terenziani, C. Sissa, and A. Painelli, "Thermally activated delayed fluorescence: A critical assessment of environmental effects on the singlet–triplet energy gap," *The Journal of Chemical Physics*, vol. 154, p. 134112, apr 2021.

[161] D. K. A. Phan Huu, S. Saseendran, R. Dhali, L. G. Franca, K. Stavrou, A. Monkman, and A. Painelli, "Thermally activated delayed fluorescence: Polarity, rigidity, and disorder in condensed phases," *Journal of the American Chemical Society*, vol. 144, no. 33, pp. 15211–15222, 2022. PMID: 35944182.

List of Publications

- D. K. Andrea Phan Huu, **Rama Dhali**, Carlotta Pieroni, Francesco Di Maiolo, Cristina Sissa, Francesca Terenziani, and Anna Painelli

  "Antiadiabatic View of Fast Environmental Effects on Optical Spectra", *Phys. Rev. Lett.* **124**, 107401 (2020).

- **Rama Dhali**, D. K. Andrea Phan Huu, Francesco Bertocchi, Cristina Sissa, Francesca Terenziani, and Anna Painelli

  "Understanding TADF: a joint experimental and theoretical study of DMAC-TRZ", *Phys. Chem. Chem. Phys.* **23**, 378-387 (2021).

- **Rama Dhali**, D. K. Andrea Phan Huu, Francesca Terenziani, Cristina Sissa, and Anna Painelli

  "Thermally activated delayed fluorescence: A critical assessment of environmental effects on the singlet–triplet energy gap", *J. Chem. Phys.* **154**, 134112 (2021).

- Ettore Crovini, **Rama Dhali**, Dianming Sun, Tomas Matulaitis, Timothy Cromberfield, David B. Cordes, Alexandra M. Z. Slawin, Cristina Sissa, Francesco Azzolin, Francesco Di Maiolo, Anna Painelli, and Eli Zysman-Colman

  "Large Dihedral Angle Relaxation of DMAC-py-TRZ:A joint Experimental and Computational Study of TADF Dye"

  (*Manuscript under preparation*)

Manuscript not part of this thesis:

- D. K. Andrea Phan Huu, Sangeeth Saseendran, **Rama Dhali**, Larissa Gomes Franca, Kleitos Stavrou, Andrew Monkman, and Anna Painelli

  "Thermally Activated Delayed Fluorescence: Polarity, Rigidity, and Disorder in Condensed Phases", *J. Am. Chem. Soc.* **144**, 15211–15222 (2022).

Acknowledgements

I wish to express my deep gratitude to my supervisor Prof. Anna Painelli for her presence, guidance and constant support during these years. I wish to thanks also Prof. Alberto Girlando, Prof. Francesca Terenziani, Dr. Cristina Sissa Dr. Matteo Masino, Dr. Andrea Lapini, Dr. Francesco Di Maiolo for the essential support.

I am thankful to all people of the research team for their help and for the interesting and useful discussions: Sangeeth Saseendran, Dr. Guillem Vargas Nadal, Dr. Brunella Bardi, Dr. Mattia Anzola, Dang Khoa Andrea Phan Huu, Elena Ferrari, Francesco Bertocchi, Francesco Azzolin, Andrea Delledonne, Davide Giavazzi, Ilaria Ferraboschi, Carlotta Pieroni, Dr Swathi K, Lorenzo Savi, Samuel Longo and Giacomo Cotelli. They all have contributed to make this journey a very important formative and scientific experience.

I am thankful to all team members of TADF*life* project, specially: Rishabh Saxena, Dr. Eimantas Duda, Dr. Francesco Rodella, Ettore Crovini, Bilal Naqvi, Nguyen Binh Minh, Prakhar Sahay, Andrei Stankevich, Kleitos Stavrou, Larissa Gomes Franca, Volodymyr Sendiuk, Daniel Hudson, Christoph Hauenstein and Stefano Sem.

I also wish to thank all people I have collaborated with:

• Prof. Eli Zysman-Colman and his team in the University of St. Andrews, Scotland for my two months secondment.

• Prof. Dr. Beat Ruhstaller and Dr. Sandra Jenatsch and their team in Fluxim, Zurich for the remote secondments.

I thank Dr. R. S. Swathi (IISER Thiruvananthapuram) and Dr. Yoann Olivier (University of Namur) for reviewing the thesis critically and carefully. It certainly helped to improve the quality of the thesis.

I thank my family and friends for all their support.

This project received funding from the European Union Horizon 2020 research and innovation program under Grant Agreement No. 812872 (TADF*life*), and benefited from the equipment and support of the COMP-HUB Initiative, funded by the "Departments of Excellence" program of the Italian Ministry for Education, University and Research (MIUR, 2018–2022). I acknowledge the support from the HPC (High-Performance Computing) facility of the University of Parma, Italy.